Doctoral Thesis

Design of High Energy Density Anode Materials for Next-generation Energy Storage Systems

Dongki Hong

Department of Energy Engineering
(Battery Science and Technology)

Graduate School of UNIST

2019

Design of High Energy Density Anode Materials for Next-generation Energy Storage Systems

Dongki Hong

Department of Energy Engineering
(Battery Science and Technology)

Graduate School of UNIST

Design of High Energy Density Anode Materials for Next-generation Energy Storage Systems

A thesis/dissertation
submitted to the Graduate School of UNIST
in partial fulfillment of the
requirements for the degree of
Doctor of Philosophy

Dongki Hong

05/29/2019
Approved by

Nam-Soon Choi

Advisor
Nam-Soon Choi

Design of High Energy Density Anode Materials for Next-generation Energy Storage Systems

Dongki Hong

This certifies that the thesis/dissertation of Dongki Hong is approved.

05/29/2019

signature

Advisor: Nam-Soon Choi

signature

Prof. Soojin Park

signature

Prof. Seok Ju Kang

signature

Prof. Hyun-Wook Lee

signature

Dr. Minchul Jang

Abstract

As environmental regulation on conventional fossil fuel energy would be tightened, interest in renewable energy and energy storage devices have been gradually increased. Especially, the electric vehicle (EV) field which mainly includes a great portion of the battery market, would be estimated to grow more than 100 times bigger than the current size in 20 years. However, the insufficient energy density of the current lithium ion battery (LIB) system hinders the popularization of the EVs. Therefore, the demands for high energy density energy storage systems have been increased sharply owing to the development of long-range EVs. The potential solutions for the enhancing energy density are the introduction of silicon (Si), germanium (Ge) anode based LIB and lithium metal battery (LMB) systems. The main difference between LIB and LMB is the number of host material. LIB consist of two host materials of anode/cathode, electrolyte, and separator. In LIB, lithium (Li) is stored as an ion state, thus it shows good electrolyte compatibility, stable battery performance, but relatively low energy density. On the other hands, LMB has one host material. Instead of anode host materials, metallic Li is occupied. We can expect higher gravimetric and volumetric energy density in LMB owing to the extra elimination of host material in the anode side. However, deposited Li metal is thermodynamically unstable and causes Li dendrite growth, resulting in low Coulombic efficiency and safety issue.

Herein, we introduce diverse strategies of Si/Ge based anodes (LIB) and gel polymer electrolyte (GPE)/electrolyte additives (LMB) for high energy density battery systems. In Si/Ge LIB, we focus on solving the original nature of large volume expansion (>300%) and low conductivity by the combination of volume expansion compensation and conductive layer. On the other hands, various attempts for Li dendrite suppression, for example, uniform Li deposition or mechanical strength are carried out in the LMB system.

In chapter II, we design a 3D porous structure with aluminum (Al) core and aluminum oxide (Al_2O_3) layer through selective etching and wet oxidation process. The volume expansion during electrochemical lithiation is compensated owing to the porous structure. Al core inside supports the overall particle structure and outer Al_2O_3 thin layer enhances ionic conductivity and structural robustness, resulting in stable long-term electrochemical performance.

In chapter III, a nitrogen-doped Ge/C composite secondary particle is reported via gelation and carbothermal reduction process using natural carbon source and germanium oxide nanoparticles. This secondary particle strategy is effective for preventing volume expansion in both particle level and electrode level owing to the existence of enough free volume inside. In addition, nitrogen dopant successfully increases the electric conductivity, leading to higher Coulombic efficiency during cycling.

In chapter IV, we report a functionalized carbon nanodot (CD) additive for LMB which is well dispersible in commercial carbonate electrolyte. In addition, CDs include surface negative charges and various functional groups, which are easily controllable through modulating the amount and types of precursors. The synergistic interplay between high negative surface charges and the configuration of nitrogen in CD plays a critical role in strong Li-ion affinity, as determined by various characterization and computational analysis. Therefore, CD draws Li ions through the strong binding energy under electric field and moves together. This CD-based shuttling not only provides the nucleation sites for Li-ions, but also induces uniform transportation of Li ions to the current collector, resulting in homogeneous Li plating.

In chapter V, we report a mechanically strengthened GPE for LMB. The GPE includes vinyl functionalized silica nanoparticles which forms direct bonds between vinyl end group and polymer chains with the thermally induced in-situ crosslinking process. The inorganic particle included GPE exhibits enough strength which suppresses the growth of Li dendrite mechanically. As a result, we secure the improved electrochemical property, prevention of electrolyte depletion, and minimized degradation layer of Li metal.

Contents

List of figures

plots of ANHC/Ge for initial three cycles. (c) Long-term cycle life of ANHC/Ge electrode at different C-rates. (d) Rate capabilities of ANHC/Ge at various C-rates. (e-f) Electrochemical impedance spectroscopy (EIS) plots for AHC (black), ANHC-10 (red), and ANHC/Ge (blue) after 1th and 100th cycles.

Figure 3-4. Electrode swelling results: cross-sectional SEM images of ANHC/Ge electrodes (a) at pristine state, after (b) 1st cycle, (c) 100th cycle, and (d) 500th cycle. (e) Equivalent plots for electrode swelling results (left ordinate) and corresponding volumetric capacities (right ordinate). Electrochemical results of high mass ANHC/Ge electrode: (f) first galvanostatic discharge/charge curves and (g) cycling stability for 100 cycles at a rate of C/5 along with previous electrode of moderate loading level.

Figure 3-5. Post characterization of ANHC/Ge electrode. (a) Schematic illustration showing structural changes of ANHC/Ge. (b) TEM image, (c, d) STEM-HAADF images, and (e) TEM-EDX mapping results for ANHC/Ge after 100 cycles at 1C rate. The inset is the corresponding SAED pattern showing amorphous nature of Ge particles after cycles. (f, g) Size distribution curves for ANHC/Ge particle and Ge particle before/after 100 cycles at 1C rate.

Figure 3-6. Full cell performance of ANHC/Ge anodes. (a) Cross-sectional SEM images of both anode and cathode before/after 300 cycles. (b) Long-term cycle life of full cell at 1C rate (Inset: red LED bulb lit up by as-assembled full cell).

Figure 4-1. Schematic and SEM images of the Li deposition behavior on the current collector. a) Original nature of Li dendrite growth with-out using the carbon dot additives and b–c) corresponding SEM images of the top view (b, inset: high magnification image) and cross-sectional view (c). d) Carbon dot-assisted homogeneous Li plating and e–f) corresponding SEM images of the top view (e, inset: high magnification image) and cross-sectional view f). Scale bars are 20 μm (Inset: 500 nm) (b, c, e, and f).

Figure 4-2. Chemical properties of the carbon dot additives. a) Structural illustration of the N-CD and U-CD. b–c) Chemical compositions of the N-CD and U-CD determined by high-resolution XPS spectra of C 1s (b) and N 1s (c), respectively. d) Model structures for the binding energy calculation of a Li ion and functional groups such as pyridinic-N, pyrrolic-N, and COOH. e–f) Binding energy of the Li ions as a function of the single functional group (e) and dual functional groups (f).

Figure 4-3. Behavior of the Li plating and stripping. A series of TEM images and HAADF-STEM images of a, e, i) plating without U-CD; b, f, j) stripping without U-CD; c, g, k) plating with the U-CD; and d, h, l) stripping with the U-CD. Scale bars are 100 nm (a–d), 10 nm (e–h), and 1 μm (i–l).

Figure 4-4. Overpotential minimization through U-CD additives. a) Initial galvanostatic voltage profiles of the Li/Cu half-cell at 0.1C-rate with areal capacity of 1 mA h cm^{-2}. b) Cycle retention

properties of the Li/Li symmetric-cell at 1C-rate with areal capacity of 1 mA h cm^{-2}. c) Cycle retention properties and d) plots of the voltage differences of the Li/Li symmetric-cell at 5C-rate with areal capacity of 0.5 mA h cm^{-2} and electrolyte concentration control. The electrolyte concentration is 0.5 mg mL^{-1} (a, b).

Figure 4-5. Stable electrochemical performances originating from the carbon dot-assisted plating. A series of SEM images of the Li metal a, c) without the CD; b, d) with the U-CD after 500 cycles. e) First-cycle voltage profile of the Li/LCO full-cell at 0.1C-rate with areal capacity of 1 mA h cm^{-2}. f) Cycle retention properties of the 20 μm Li/LCO extreme full-cell test at 1C-rate with areal capacity of 1 mA h cm^{-2}. Scale bars are 200 μm (a–d). The electrolyte concentration is 0.5 mg mL^{-1}.

Figure 5-1. Schematic illustration of a synthetic approach for the high mechanical strength of polymer-inorganic filler matrix based gel polymer electrolyte.

Figure 5-2. Physical and chemical properties of vinyl functionalized silica nanoparticle (VSNP) and various gel polymer electrolyte (GPE). (a) an SEM image of VSNP. FT-IR spectra of (b) bare silica and VSNP. (c) various GPEs before and after gelation. (d) Strain-stress curve of GPEs. (e) Young's Modulus and rupture point of GPEs. (f) ionic conductivity of liquid electrolyte (LE) and various GPEs.

Figure 5-3. The profiles of voltage versus time for lithium stripping/plating experiments of symmetric lithium cells. Voltage profiles for LE and various GPEs with the cycling conditions of (a) an areal capacity of 1mAh cm^{-2} with a current density of 1mA cm^{-2}. (b) an areal capacity of 0.4mAh cm^{-2} with a current density of 2mA cm^{-2}.

Figure 5-4. Morphology of lithium growth on Cu current collector after cycles 100 times at 0.5C-rate with different electrolyte. Components of each electrolyte are (a) liquid electrolyte (b) ETG (c) ETG-SNP (d) ETG-VSNP.

Nomenclature

ALD	atomic layer deposition
BET	**Brunauer-Emmett-Teller analysis**
C_2H_2	acetylene gas
CE	Coulombic efficiency
CMC	sodium carboxymethyl cellulose
CVD	chemical vapor deposition
DEC	diethyl carbonate
DFT	density function theory
DI water	deionized water
DMF	N,N-dimethylformamide
EC	ethylene carbonate
EDX(S)	energy-dispersive X-ray spectroscopy
EIS	electrochemical impedance spectroscopy
EVs	electric vehicles
FEC	fluoroethylene carbonate
FFT	fast Fourier transform
FT-IR	Fourier transform infrared
GPE	gel polymer electrolyte
HAADF	high angle annular dark field
HCl	hydrochloric acid
ICE	initial Coulombic efficiency
LCO	$LiCoO_2$
LE	liquid electrolyte
LIB	Lithium ion battery
LiPF6	lithium hexafluorophosphate
NG	natural graphite
LMB	Lithium metal battery
LMO	$LiMn_2O_4$
NMP	N-methyl-2-pyrrolidone
PAA	poly(acrylic acid)
PC	polycarbonate
PVdF	poly(vinylidene fluoride)
SAED	selected area electron diffraction
SBR	styrene-butadiene rubber

SEI	solid-electrolyte-interface
SEM	scanning electron microscopy
STEM	scanning/transmission electron microscope
TEM	transmission electron microscopy
TGA	thermogravimetric analysis
XPS	X-ray photoelectron spectroscopy
XRD	X-ray diffraction

1. Introduction

1.1 Demands for high energy density

A new class energy storage devices and technologies are coming into the spotlight in the contemporary society, as the energy issues related to a rapid increase of energy consumption from tremendous population growth has become a public concern. Since Alessandro Volta suggested electrochemical cell, various battery systems such as zinc-bromine, nickel-cadmium, lead-acid, lithium-ion, sodium-sulfur, etc. have been commercialized[1]. Among diverse systems, LIBs become a mainstream of energy storage in daily life which enables operation of mobile devices, electric transportations, and energy storage systems[2-5].

The global electric vehicle (EV) market which is one of the largest battery consumer is predicted to grow more than 10 times bigger than the current market size in 10 years[6]. However, current EVs exhibit insufficient mileage originated from the low energy density of battery compared to the fossil fuel-based automobile[7]. This is because the current commercialized LIB system which mostly consists of graphite anode with lithium oxide cathode represent a relatively low energy density of 85 to 130 Wh kg^{-1} and 220 to 300 Wh L^{-1} [8]. Therefore, the demands for the development of high-performance battery in terms of energy density, power density, durability, and efficiency have been increased sharply owing to the EV driving range extension[9].

To design the ideal battery for EVs, a fundamental understanding of the present situation is necessary. As the environmental regulation has been tightened, many automobile companies have great efforts in expanding the EVs line up and replacing the internal combustion engine gradually. To substitute the engine into the motor, securing sufficient mileage is important. The conventional gasoline/diesel based vehicles represent more than 600 km of distance range per tank. In the case of EVs, it needs to 150 kWh of the battery pack to reach the same travel distance which means around 1 ton of conventional LIB has to stored in a cabin room. This battery pack weight must be reduced to maintain the driving performance of EVs and a simple solution is getting higher energy density.

The great potentials of the battery market predispose many researchers and companies to develop the next-generation battery systems for EVs which are targeted in the direction of having a high energy density[10-15]. In particular, group IV elements (Si, Ge) based high energy density LIB and Li metal battery (LMB) are receiving the spotlight owing to their own advantages and

applicability as a next-generation battery. The Si, Ge based LIB and LMB are expected to show more than 300 Wh kg^{-1} of energy density which is 2~3 times more than graphite based LIB. These next-generation battery systems deliver more than 600 km of mileage and would increase the EVs market share.

The main difference between LIB and LMB is the number of Li-ion host materials. For example, LIB has two Li-ion host materials of anode and cathode. LIB stores the Li as an ion state with three different chemical reactions of intercalation, alloy, and conversion[16]. Thus, LIB is less vulnerable to side reaction and delivers good chemical compatibility and stable electrochemical performance. On the other hands, LMB has only one host material. Instead of anode host, metallic Li is occupied. The extra elimination of anode host in LMB compare to LIB, higher gravimetric and volumetric capacity is exhibited. However, Li dendrite growth which is the critical issue of LMB causes low Coulombic efficiency attributed to continuous SEI crack and formation, leading to poor cycle performance and battery safety issue. Therefore, radical study and design are necessary for practical usage of high energy density LIB and LMB.

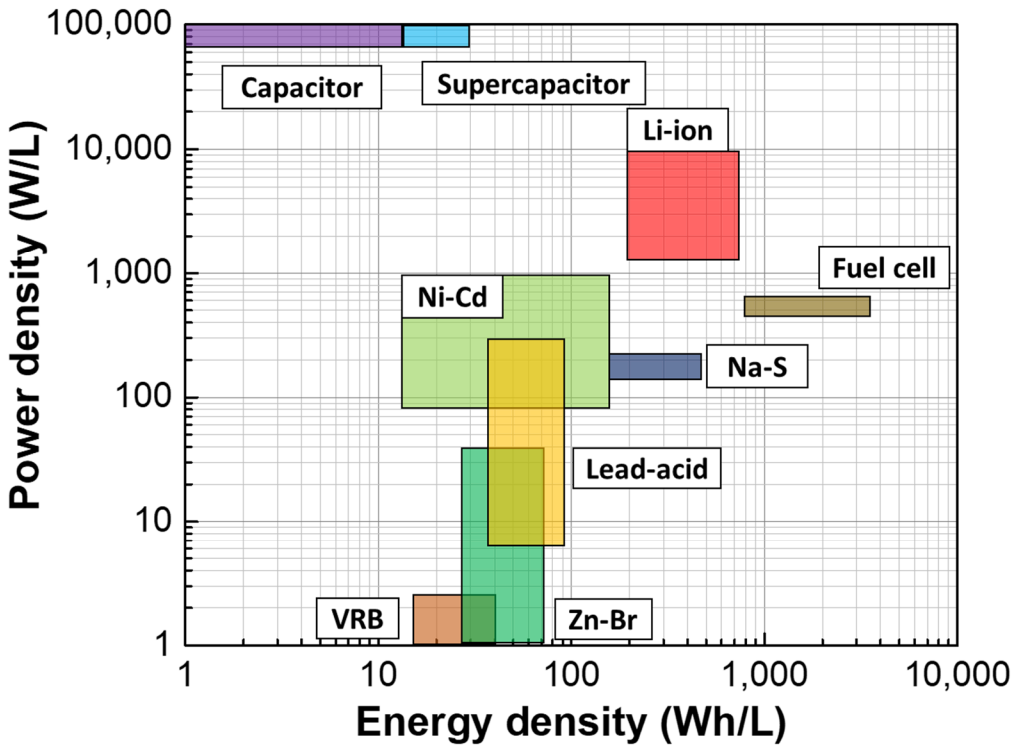

Figure 1-1. Ragone plot for various energy storage systems[1].

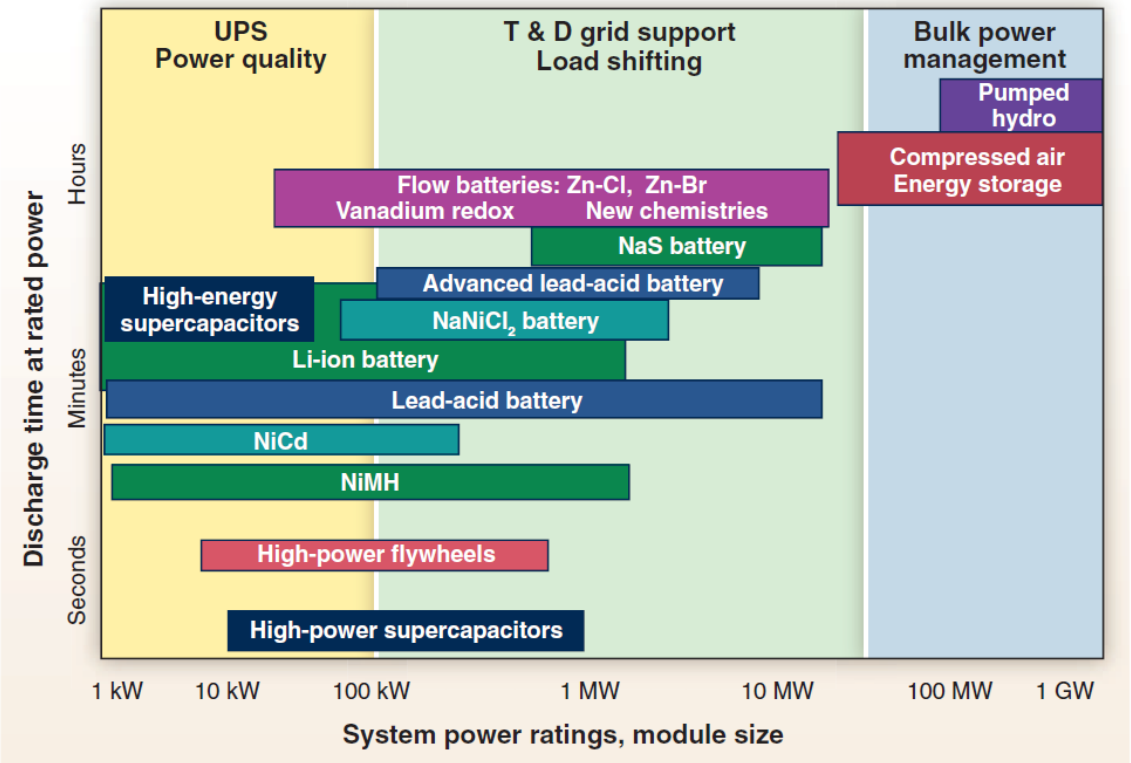

Figure 1-2. Comparison of discharge time and power rating[2].

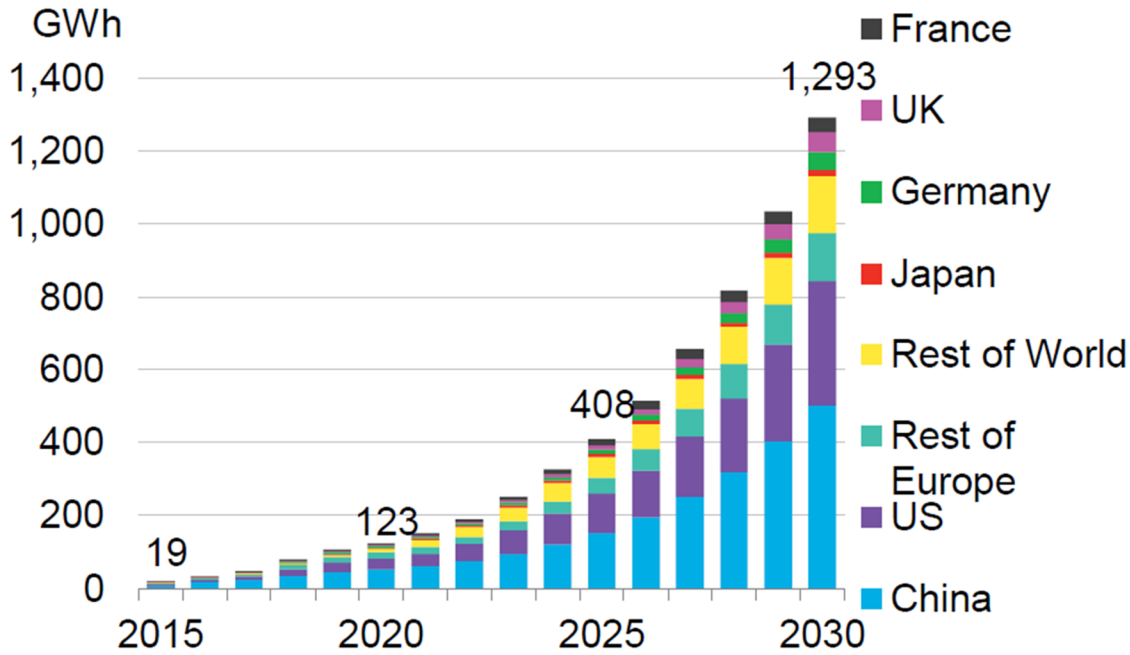

Figure 1-3. Forecasted demand for lithium-ion batteries from EVs, 2010-2030 [6].

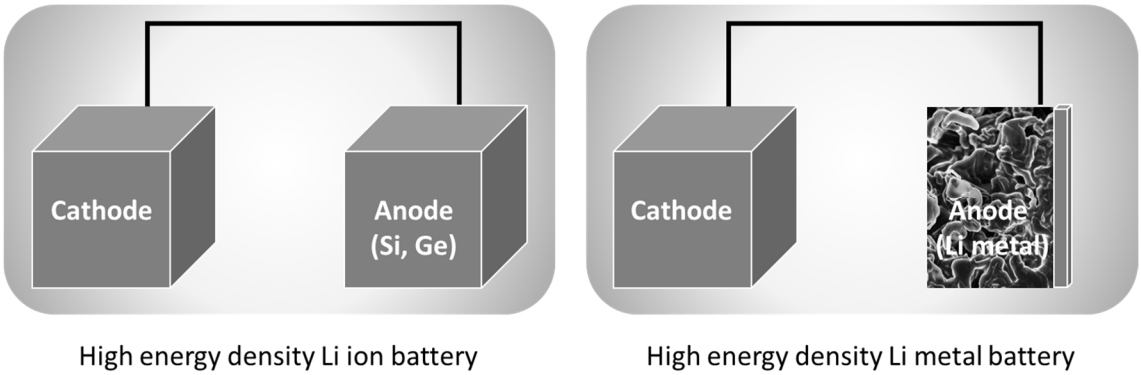

Figure 1-4. Schematic diagram of the number of host materials in LIB and LMB.

1.2 Anode materials for high energy density LIB

Since SONY launched commercial available LIB in 1991, sweeping changes have occurred in modern life in terms of mobile electronic devices and electric transportation[17-19]. The essential components of LIB are two Li-ion host electrodes of anode/cathode, electrolyte, and separator[20]. Most of early LIBs are based on a graphite anode with $LiCoO_2$ (LCO) or $LiMnO_2$ (LMO) cathode which exhibits the limited energy density of 80 Wh kg^{-1} and 200 Wh cm^{-3} [21]. Therefore, many companies and researchers have followed the development of high energy density battery systems with much interest in the extension of various applications. In particular, research on a new class anode materials has been widely performed[22-24].

Among various candidates of LIB anode host materials, in particular, group IV elements (Si, Ge, etc.) have great potential for realizing the high energy density battery. This is because they exhibit relatively higher specific capacity (Si: 3572 mA h g^{-1} and 8319 mA h cm^{-3}, Ge: 1384 mA h g^{-1} and 7367 mA h cm^{-3} at room temperature) owing to their large number of Li-ion intake in fully lithiation state ($Li_{15}Si_4$ and $Li_{15}Ge_4$ at room temperature) while graphite delivers only 372 mA h g^{-1} and 866 mA h cm^{-3} of specific capacity with stoichiometry of LiC_6[25-27]. In addition, their low lithiation/delithiation voltage (~370 mV vs. Li/Li^+) during alloying/dealloying reaction allow high operating voltage, resulting in higher energy density[28]. However, their original nature of large volume expansion (>300%) and low electric conductivity (Si: 1000 S/m, Ge: 2000 S/m) provoke poor cyclability and low Coulombic efficiency[29-31]. To overcome the intrinsic properties of Si and Ge, robust design in terms of structure and conductivity is necessary.

As mentioned before, the biggest challenges in alloying type anodes such as Si and Ge based materials are the large volume expansion at fully lithiated states and the intrinsic property of low electric conductivity. Various strategies have been carried out to offset the disadvantages[32-41]. In the case of volume expansion, compensation space such as porous structure[34-36, 41], tubular structure[40] or secondary particle[38] is commonly utilized. Therefore, during the lithiation process, volume expansion occurs within the extra space leading to minimum distension at the bulk level. The intrinsic property of low conductivity is settled through the introduction of a conductive layer[32-33, 37, 39] and elemental doping[38]. Owing to the enhanced conductivity of anode materials, electrochemical tests represent not only the higher Coulombic efficiency but also the long cycle life. A synergetic interaction between surplus space and high electric conductivity induces stable cycle performance. These Si and Ge anode materials based high energy density LIB would mark a new epoch in battery applications.

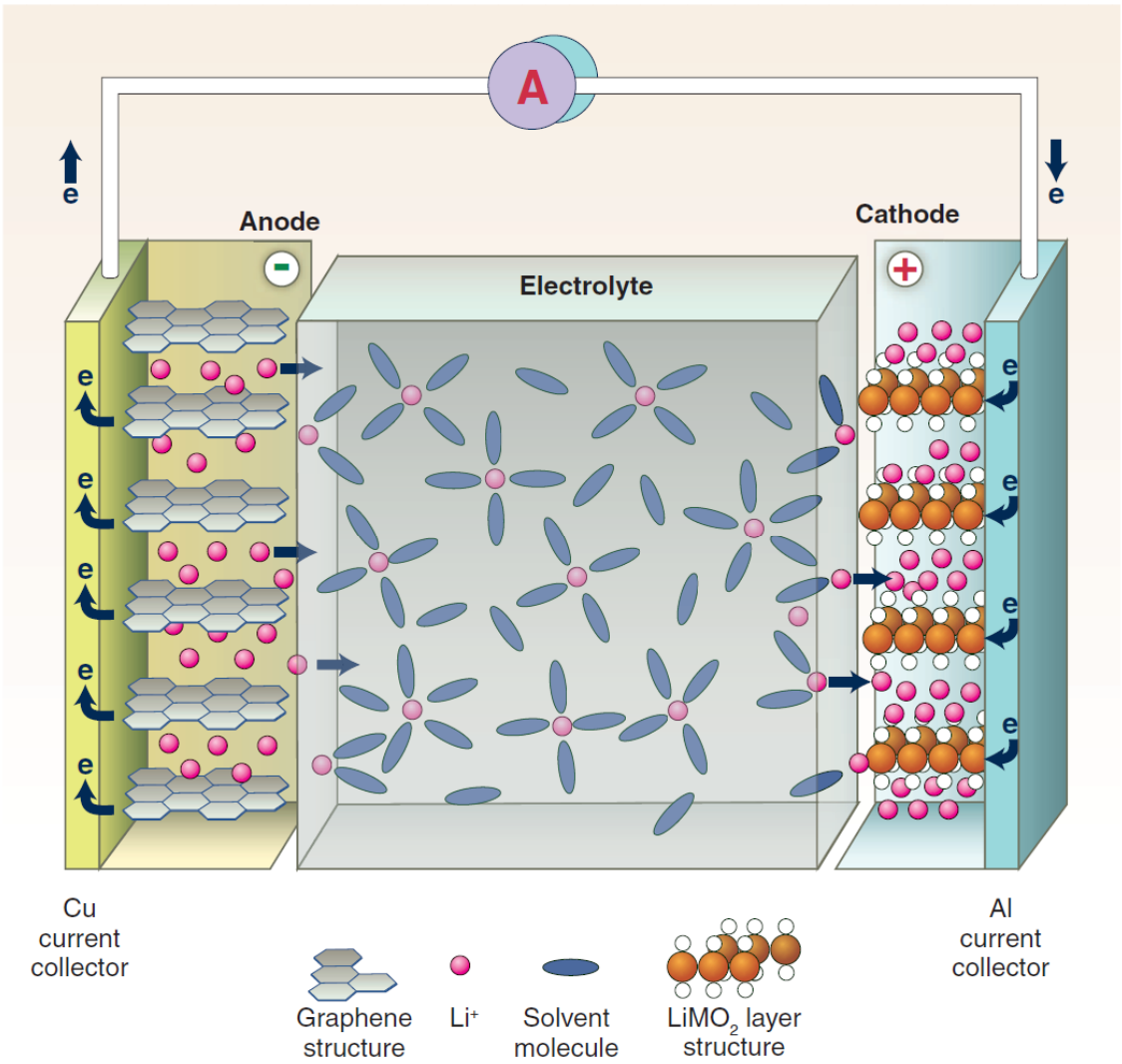

Figure 1-5. Schematic diagram of a general LIB[2].

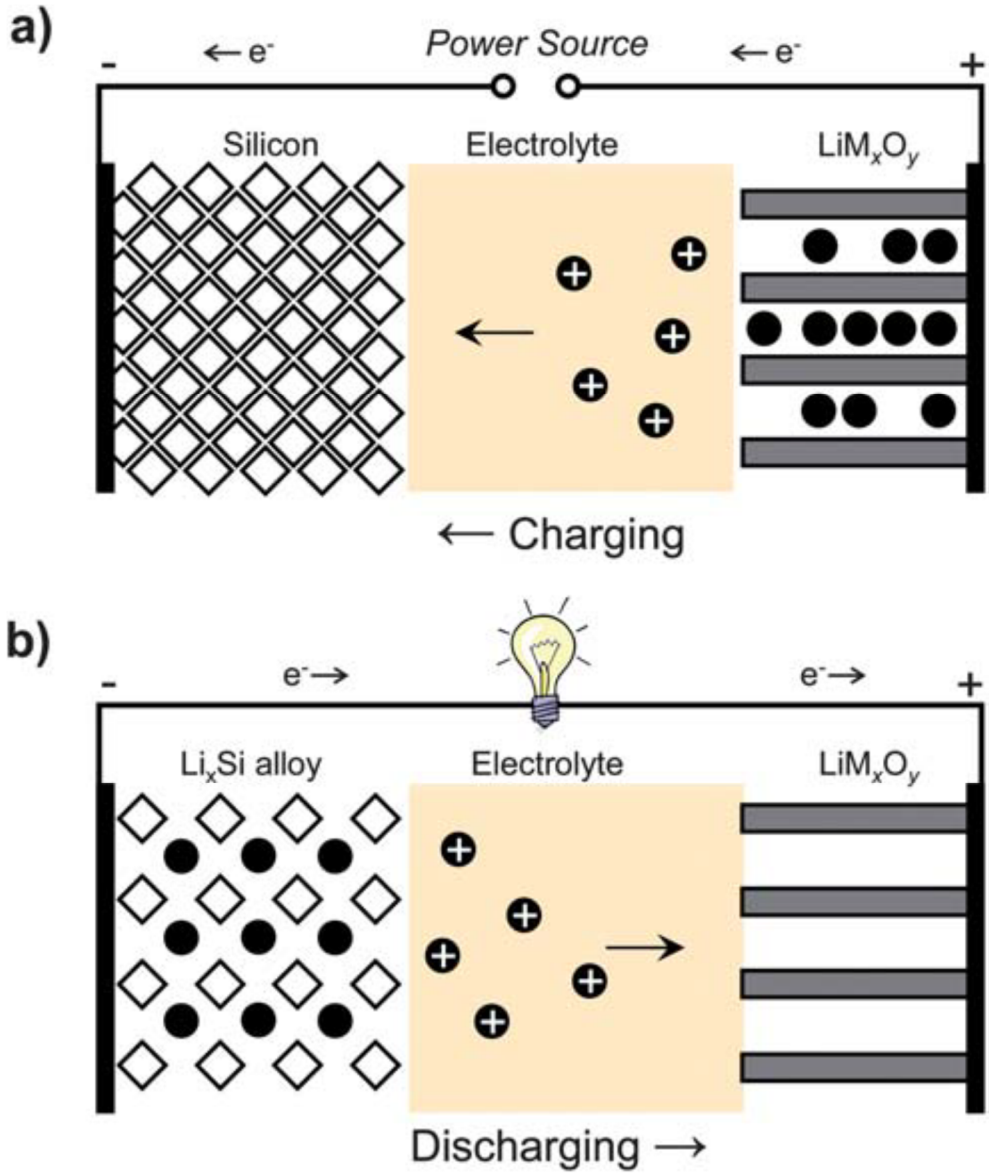

Figure 1-6. Schematic of a lithium battery containing a silicon anode and lithium metal oxide cathode during a) charging and b) discharging[28].

1.3 Design of high energy density LMB

Since LIB invented in 1991 by SONY, the energy density of LIB has increased (80 to 270 Wh kg^{-1} and 200 to 770 Wh L^{-1}) over the past 25 years[42]. However, the LIB has an obvious physicochemical limit of energy density (420 Wh kg^{-1} and 1400 Wh L^{-1}), thus the necessity of a new kind of battery system has been emphasized owing to the demands for higher energy density battery[43]. Accordingly, the lithium metal which represents the lowest electrochemical potential (-3.04 V vs. the standard hydrogen electrode) and high theoretical specific capacity (3,860 mA h g^{-1}) is in the spotlight as a new system[44]. The LMB consisting of Li metal anode and a cathode electrode (lithium oxide, sulfur, oxygen) delivers much higher theoretical energy density (Li metal for 13000 Wh kg^{-1} and 6900 Wh L^{-1}; Li-S for 2500 Wh kg^{-1} and 2800 Wh L^{-1}; Li-O_2 for 3458 Wh kg_{Li2O2}^{-1} and 7989 Wh L_{Li2O2}^{-1}) than LIBs[45-47]. Therefore, LMB is considered as a top priority for the beyond LIBs.

However, direct usage of Li metal as an anode causes the critical issue of Li dendrite growth[48]. The thermodynamically unstable interface between Li metal and the liquid electrolyte not only lowers the solidification barrier but also allows the local concentration of Li-ion flux, resulting in the uncontrollable heterogeneous deposition during Li plating/stripping[49]. This needle-like Li metal represents a high shear modulus (~1 x 10^9 Pa) which is enough value to penetrate the polymer separator during cycling and causes an internal short circuit[48]. The internal short circuit triggers serious safety concerns of battery explosion and thermal runaway which strongly hinders the practical usage of LMBs. Therefore, lots of attentions have concentrated on the inhibition of Li dendrite growth.

The uneven Li deposition also provokes various issues including continuous solid electrolyte interphase (SEI) crack/formation, electrolyte depletion, low Coulombic efficiency, and poor cyclability. Therefore, for the better operation of LMBs, diverse approaches for Li dendrite suppression such as 3D-structured anode (cage the Li metal into the 3D matrix), electrolyte additives (induce the homogeneous Li nucleation), gel-polymer electrolyte (Li dendrite inhibition through the mechanical strength), and artificial SEI (prevent side reaction) have been suggested[50-53]. In spite of the great efforts against Li dendrite suppression, the current LMB performance is still far from the commercial level. In addition, the operation and failure mechanism of LMBs still remain as an unknown world. Therefore, fundamental understanding and inhibition of Li dendrite growth in terms of high Coulombic efficiency, safety, and cycle retention property is a key precondition of LMB commercialization.

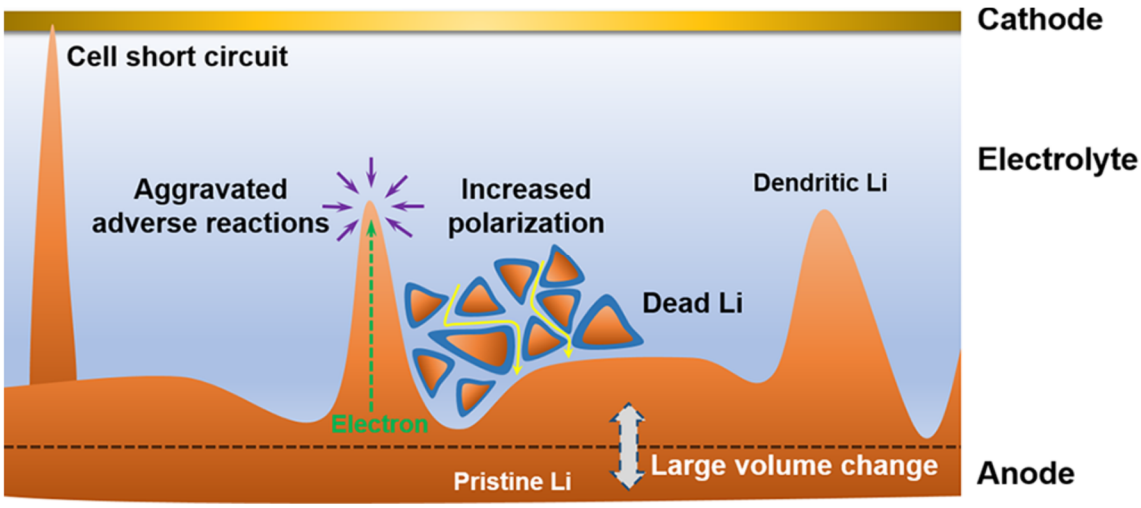

Figure 1-7. Schematic of dilemma for Li metal anode in rechargeable batteries[48].

1.4 Reference

1. Ryu, J.; Hong, D.; Lee, H. Y.; Park, S. Practical considerations of si-based anodes for lithium-ion battery applications. Nano research **2017**, *10*, 3970-4002.
2. Dunn, B.; Kamath, H.; Tarascon, J.-M. Electrical Energy Storage for the Grid: A Battery of Choices. *Science* **2011**, *334*, 928−935.
3. Armand, M.; Tarascon, J. M. Building better batteries. *Nature* **2008**, *451*, 652-657.
4. Evarts, E. C. To the limits of lithium. *Nature* **2015**, *526*, S93-S95.
5. Grande, L.; Paillard, E.; Hassoun, J.; Park, J. B.; Lee, Y. J.; Sun, Y. K.; Passerini, S.; Scrosati, B. The lithium/air battery: still an emerging system or a practical reality? *Adv. Mater.* **2015**, *27*, 784-800.
6. Curry C. Lithium-ion battery costs and market. *Bloomberg New Energy Finance*, **2017**.
7. Pelegov, D. V.; Pontes, J. Main drivers of battery industry changes: Electric vehicles-a market overview. *Batteries*, **2018**, *4*, 65.
8. Li, M.; Lu, J.; Chen, Z.; Amine K. 30 years of lithium-ion batteries. *Adv. Mater.* **2018**, *30*, 1800561.
9. Palacin, M. R.; Guibert, A. Why do batteries fail? *Science*, **2016**, *351*, 1253292.
10. Shin, M.; Song, W. J.; Han, J. G.; Hwang, C.; Lee, S.; Yoo, S.; Park, S.; Song, H. K.; Yoo, S.; Choi, N. S.; Park, S. Metamorphosis of seaweeds into multitalented materials for energy storage applications. *Adv. Energy Mater.* **2019**, *9*, 1900570.
11. Wang, B.; Ryu, J.; Choi, S.; Zhang, X.; Pribat, D.; Li, X.; Zhi, L.; Park, S.; Ruoff, R. S. Ultrafast-charging silicon-based coral-like network anodes for lithium-ion batteries with high energy and power densities. *ACS Nano* **2019**, *13*, 2307-2315.
12. Lee, J. I.; Shin, M.; Hong, D.; Park, S. Efficient Li-ion-conductive layer for the realization of highly stable high-voltage and high-capacity lithium metal batteries. *Adv. Energy Mater.* **2019**, *9*, 1803722.
13. Ryu, J.; Chen, T.; Bok, T.; Song, G.; Ma, J.; Hwang, C.; Luo, L.; Song, H. K.; Cho, J.; Wang, C.; Zhang, S.; Park, S. Mechanical mismatch-driven rippling in carbon-coated silicon sheets for stress-resilient battery anodes. *Nat. Commun.* **2018**, *9*, 2924.
14. Shin, M.; Song, W. J.; Son, H. B.; Yoo, S.; Kim, S.; Song, G.; Choi, N. S.; Park, S. Highly stretchable separator membrane for deformable energy-storage devices. *Adv. Energy Mater.* **2018**, *8*, 1801025.
15. Wang, B.; Ryu, J.; Choi, S.; Song, G.; Hong, D.; Hwang, C.; Chen, X.; Wang, B.; Li, W. Song, H. K.; Park, S.; Ruoff, R. S. Folding graphene film yields high areal energy storage in lithium-

ion batteries. *ACS Nano* **2018**, *12*, 1739-1746.

16. Palacin, M. R. Recent advances in rechargeable battery materials: A chemist's perspective. *Chem. Soc. Rev.* **2009,** *38*, 2565-2575.
17. Li, W.; Dahn, J. R.; Wainwright, D. S. Rechargeable lithium batteries with aqueous electrolytes. *Science* **1994**, *264*, 1115-1118.
18. Johnson, B. A.; White, R. E. Characterization of commercially available lithium-ion batteries. *J. Power Sources* **1998**, *70*, 48-54.
19. Megahed, S.; Scrosati, B. Lithium-ion rechargeable batteries. *J. Power Sources* **1994**, *51*, 79-104.
20. McDowell, M. T.; Lee S. W.; Nix W. D.; Cui Y. 25th anniversary article: Understanding the lithiation of silicon and other alloying anodes for lithium-ion batteries. *Adv. Mater.* **2013,** *25*, 4966-4984.
21. Blomgren, G. E. The development and future of lithium ion batteries. *J. Electrochem. Soc.* **2017**, *164*, A5019-A5025.
22. Nitta, N.; Wu, F.; Lee, J. T.; Yushin, G. Li-ion battery materials: present and future. *Materials Today* **2015**, *18*, 252-264.
23. Chen, Y. M.; Yu, X. Y.; Li, Z.; Paik, U.; Lou, X. W. Hierarchical mos2 tubular structures internally wired by carbon nanotubes as a highly stable anode material for lithium-ion batteries. *Sci. Adv.* **2016**, *2*, e16000021.
24. Roy, P.; Srivastava, S. K. Nanostructured anode materials for lithium ion batteries. *J. Mater. Chem. A.* **2015**, *3*, 2454-2484.
25. Hu, L.; Wu, H.; Gao, Y.; Cao, A.; Li, H.; Mcdough, J.; Xie, X.; Zhou, M.; Cui, Y. Silicon-carbon nanotube coaxial sponge as li-ion anodes with high areal capacity. *Adv. Energy Mater.* **2011**, *1*, 523-527.
26. Son, I. H.; Park, J. H.; Kwon, S.; Park, S.; Rummeli, M. H.; Bachmatiuk, A.; Song, H. J.; Ku, J.; Choi, J. W.; Choi, J. M.; Doo, S. G.; Chang, H. Silicon carbide-free graphene growth on silicon for lithium-ion battery with high volumetric energy density. *Nat. Commun.* **2015**, *6*, 7393.
27. Jung, H.; Park, M.; Yoon, Y. G.; Kim, G. B. Amorphous silicon anode for lithium-ion rechargeable batteries. *J. Power Sources*, **2003**, *115*, 346-351.
28. Szczech, J. R.; Jin, S. Nanostructured silicon for high capacity lithium battery anodes. *Energy Environ. Sci.* **2011**, *4*, 56-72.
29. Reece, S. Y.;Hamel, J. A.;Sung, K.;Jarvi, T. D.;Esswein, A. J.;Pijpers, J. J. H.; Nocera, D. G. Wireless solar water splitting using silicon-based semiconductors and earth-abundant catalysts. *Science* **2011**, *334*, 645-648.

30. Putley, E. H. The electrical conductivity of germanium. *Proc. Phys. Soc. A* **1949**, *62*, 284-292.

31. Cui, G.; Gu, L.; Zhi, L.; Kaskhedikar, N.; Aken, P. A. van; Mullen, K.; Maier, J. A germanium-carbon nanocomposite material for lithium batteries. *Adv. Mater.* **2008**, *20*, 3079-3083.

32. Ryu, J.; Hong, D.; Choi, S.; Park, S. Synthesis of ultrathin Si nanosheets from natural clay for lithium-ion battery anodes. *ACS Nano* **2016**, *10*, 2843-2851.

33. Park, H.; Choi, S.; Lee, S. J.; Cho, Y. G.; Hwang, G.; Song, H. K.; Choi, N. S.; Park, S. Design of an ultra-durable silicon-based battery anode material with exceptional high-temperature cycling stability. *Nano energy* **2016**, *26*, 192-199.

34. Ryu, J.; Hong, D.; Shin, M.; Park, S. Multiscale hyperporous silicon flake anodes for high initial coulombic efficiency and cycle stability. *ACS Nano* **2016**, *10*, 10589-10597.

35. Hong, D.; Ryu, J.; Shin, S.; Park, S. Cost-effective approach for structural evolution of si-based multicomponent for Li-ion battery anodes. *J. Mater. Chem. A* **2017**, *5*, 2095-2101.

36. Choi, S.; Cho, Y. G.; Kim, J.; Choi, N. S.; Song, H. K.; Wang, G.; Park, S. Mesoporous germanium anode materials for lithium-ion battery with exceptional cycling stability in wide temperature range. *Small* **2017**, *13*, 1603045.

37. Kim, C.; Hwang, G.; Jung, J. W.; Cho, S. H.; Cheong, J. Y.; Shin, S.; Park, S.; Kim, I. D. Fast, scalable synthesis of micronized ge3n4@c with a high tap density for excellent lithium storage. *Adv. Funct. Mater.* **2017**, *27*, 1605975.

38. Ryu, J.; Hong, D.; Shin, S.; Choi, W.; Kim, A.; Park, S. Hybridizing germanium anodes with polysaccharide-derived nitrogen-doped carbon for high volumetric capacity of li-ion batteries. *J. Mater. Chem. A* **2017**, *5*, 15828-15837.

39. Lee, J. I.; Ko, Y.; Shin, M.; Song, H. K.; Choi, N. S.; Kim, M. G.; Park, S. High-performance silicon-based multicomponent battery anodes produced via synergistic coupling of multifunctional coating layer. *Energy Environ. Sci.* **2015**, *8*, 2075-2084.

40. Ryu, J.; Choi, S.; Bok, T.; Park, S. Nanotubular structured si-based multicomponent anodes for high-performance lithium-ion batteries with controllable pore size via coaxial electro-spinning. *Nanoscale* **2015**, *7*, 6126-6135.

41. Choi, S.; Kim, J.; Choi, N. S.; Kim, M. G.; Park, S. Cost-effective scalable synthesis of mesoporous germanium particles via a redox-transmetalation reaction for high-performance

energy storage devices. *ACS Nano* **2015**, *9*, 2203-2212.

42. Janek, J.; Zeier, W. G. A solid future for battery development. *Nat. Energy* **2016**, *1*, 16141.
43. Yang, Y.; Zheng, G. Cui, Y. Nanostructured sulfur cathodes. *Chem. Soc. Rev.* **2013**, *42*, 3018-3032.
44. Sun, Y.; Liu, N.; Cui, Y. Promises and challenges of nanomaterials for lithium-based rechargeable batteries. *Nat. Energy* **2016**, *1*, 16071.
45. Seh, Z. W.; Sun, Y.; Zhang, Q.; Cui, Y. Designing high-energy lithium-sulfur batteries. *Chem. Soc. Rev.* **2016**, *45*, 5605-5634.
46. Cheng, H.; Scott, K. Carbon-supported manganese oxide nanocatalysts for rechargeable lithium-air batteries. *J. Power Sources* **2010**, *195*, 1370-1374.
47. Wu, F.; Yu, Y. Toward true lithium-air batteries. *Joule* **2018**, *2*, 814-824.
48. Cheng, X. B.; Zhang, Rui, Zhao, C. Z.; Zhang Q. Toward safe lithium metal anode in rechargeable batteries: a review. *Chem. Rev.* **2017**, *117*, 10403-10473.
49. Li, X.; Zheng, J. M.; Ren, X. D.; Engelhard, M. H.; Zhao, W. G.; Li, Q. Y.; Zhang, J. G.; Xu, W. Dendrite-free and performance-enhanced lithium metal batteries through optimizing solvent compositions and adding combinational additives. *Adv. Energy Mater.* **2018**, *8*, 1703022.
50. Liu, S. F.; Xia, X. H.; Zhong, Y.; Deng, S. J.; Yao, Z. J.; Zhang, L. Y.; Cheng, X. B.; Wang, X. L.; Zhang, Q.; Tu, J. P. 3D TiC/C core/shell nanowire skeleton for dendrite-free and long-life lithium metal anode. *Adv. Energy Mater.* **2018**, *8*, 1702322.
51. Li, W. Y.; Yao, H. B.; Yan, K.; Zheng, G. Y.; Liang, Z.; Chiang, Y. M.; Cui, Y. The synergetic effect of lithium polysulfide and lithium nitrate to prevent lithium dendrite growth. *Nat. Commun.* **2015**, *6*, 7436.
52. Manthiram, A.; Yu, X.; Wang, S. Lithium battery chemistries enabled by solid-state electrolytes. *Nat. Rev. Mater.* **2017**, *2*, 16103.
53. Li, N. W.; Yin, Y. X.; Yang, C. P.; Guo, Y. G. An artificial solid electrolyte interphase layer for stable lithium metal anodes. *Adv. Mater.* **2016**, *28*, 1853-1858.

Chapter II. Cost-effective approach for structural evolution of Si-based multicomponent for Li-ion battery anodes

2.1 Introduction

Troubleshooting stubborn problems of Si-based anode materials have been achieved using various approaches to adapt great demands for more effective energy storage devices, specifically lithium-ion batteries (LIBs) in recent years. Si delivers the highest specific (~3579 mAh g^{-1} for $Li_{15}Si_4$ at room temperature) and volumetric capacities (~7000 mAh cm^{-3}) among various alloying materials toward lithium, along with low working potential (< 0.4V *versus* Li/Li^+) and abundance in nature.[1-6] However, lithium ion insertion/extraction brings about a dramatic volume expansion (>300% at fully lithiated state) and accordingly results in mechanical failure and pulverization of electrodes.[7-9] Consequently, continuous decomposition of electrolytes through those cracks leads to the formation of thicker solid-electrolyte-interphase (SEI) layers and eventually drastic capacity fading due to its electrically insulating nature.[7-9]

The foregoing issues of Si anodes, structural disruption and surface instability have been principally resolved by downscaling the dimension in nanometer and introducing passivation layers. Various nanostructured Si materials have been investigated as promising anode materials which showed undoubtedly improved cycling retention and high-rate durability by shortening the diffusion length of lithium ion.[10-25] However, surface side reactions and irreversible trapping of lithium ion by a plenty of defect sites diminish the structural advantages together with easy agglomeration. As noted, these problems reduce the coulombic efficiency of electrochemical cells for extended cycles and cannot be stabilized, which will impede the commercialization of these materials.[26,27]

Accordingly, special emphasis on nanocomposite materials (Si/inactive and Si/active) have been highlighted.[28-35] Among various candidates, Al_2O_3 can promote both structural and interfacial stability of Si-based composites. Numerous studies have revealed that thin Al_2O_3 passivation layers form a Li-Al-O glass film, which is known as lithium ion conductor and electron insulator, during first lithiation, leading to the prevention of electrolyte decomposition at low potential range. Furthermore, superior mechanical property of Al_2O_3 layers can enhance the structural integrity.[36, 37]

For example, Nguyen *et al.* demonstrated the synthesis of Al_2O_3 and hard to be practically applicable. Likewise, He *et al*. showed Al_2O_3 coated patterned amorphous Si by atomic layer

deposition (ALD) to modify the surface of Si anode.[39] It indicated tremendous improvement on interfacial stability and electrochemical performances, while relatively low coulombic efficiency (<99%) during cycles still remains big challenges. Meanwhile, Kim *et al*. reported carbon coated Si-$NiSi_2$-Al_2O_3 composites synthesized by sequential mechanical milling.[40] It showed great strengths on feasibility of commercial implementation and improved electrochemical properties in terms of electrode stability, cell impedance and coulombic efficiency per cycle. However, only 700 mAh g^{-1} of reversible capacity was attained after repeated cycles at the expense of anode capacity. Recently, Hwang *et al.* demonstrated nanoporous Si/Al_2O_3 foam anodes, which still showed large electrode swelling problem (>130%) not comparable to commercial anode materials.[41]

In this regard, we report Si-based multicomponent anodes *via* selective etching and subsequent wet-oxidation of Al-Si alloy (ASWO) to achieve novel architecture of Al_2O_3 passivated porous Si multicomponents showing excellent electrochemical performance. Depending on the amounts of Al remained after controlled etching process, disparate behaviour of micro-structure was obtained. Relatively Al-rich phase evolved to form a large portion of Al_2O_3 layers which left behind structural asymmetry at the core of spheres. Instead, Si-rich phase retained uniform distribution of Al_2O_3 over the spheres which lose structural robustness in absence of the cores. Optimized Si-based multicomponent anodes have structural integrity which originates from Al/Al_2O_3 core support and interfacial stability leading to uniform SEI formation. Its remarkable battery performance was evaluated both in lithium half-cell and full-cell composed of lithium cobalt oxide (LCO)/ natural graphite (NG)-Si multicomponent, which can show a stable cycling (cycle retention of 81.9% at a rate of 0.2C after 500 cycles in half cell and 75.3% at a rate of 1C after 200 cycles in full cell), rate capability (92.5% capacity conservation at 5C rate compared to 0.2C rate) and suppressed swelling problem (18.2% after 30 cycles).

2.2 Experimental

Synthesis of ASWO

10g of Al-Si alloy powder (325 mesh, 99%, Al:Si = 88 : 12 (w/w), Alfa Aesar) was dispersed in 400 mL of 3 M hydrochloric acid (35-37%, Samchun chemical Co., Ltd, South Korea) for 15 min, 20 min, 30 min and 60 min with stirring. After selective etching process, the powder was filtered and rinsed with deionized water and ethanol. The filtered sample was dried at 70 ºC for 24 h. After drying, wet oxidation process was conducted in the condition of 600 ºC for 40 min with inserting water-vapour. The water vapour was supplied into the tube furnace by bubbling deionized (DI) water assisted with N_2 gas (5 L min^{-1}).

Physical characterizations

Scanning electron microscopy (SEM, Verios 460, FEI) was used to characterize the surface morphologies of ASWO samples at an acceleration voltage of 10 kV and a current of 0.8 nA. The dimensions and internal structures of ASWO were determined using transmission electron microscopy (TEM, JEOL-2100) and HRTEM (JEOL-2100C) at an acceleration voltage of 200 kV. To investigate the microstructures and degrees of crystallinity of ASWO samples, X-ray diffraction (XRD) analysis (D8 ADVANCE, Bruker) between 10° to 90° were performed using Cu-Kα radiation (λ = 1.5418 Å); Raman spectroscopy (alpha300R confocal microscope, WITec) was also employed for this purpose. The BET surface area and pore sizes were characterized using automatic physisorption analyser (Micrometriticx, ASPS 2020).

Electrochemical test

To evaluate the electrochemical performances of ASWO, coin-type half and full cells were fabricated using CR 2016 type cells in an argon-filled glove box. First, slurry consisting of ASWO, super-P carbon black, a 1 : 1 mixture of poly(acrylic acid) (PAA, weight average molecular weight of ~100 kg/mol, Aldrich), and sodium carboxymethyl cellulose (CMC, 4 wt% in H2O, Aldrich) as a binder with a mass ratio of 7 : 1 : 2. The active loading mass of Si electrode was 1-1.5 mg cm^{-2}. Second, Si/natural graphite (NG) electrode was composed of Si, NG, super-P, and binder in a weight ratio of 15:75:2:8 in water. The resulting slurry was spread using a doctor blade on Cu foil. The loading mass of active materials was ~2 mg cm^{-2}. Finally, the LiCoO2 (from LG Chem. Co. Ltd.) electrodes were fabricated by mixing the LCO, super-P with a binder, at a weight ratio of 85:7.5:7.5 in NMP solution. The LCO mixture was coated onto an Al current collector. The average LCO loading of electrode was around 4 mg cm^{-2}. All the other specific

electrochemical test conditions are summarized in Table S1 (ESI†). The potential windows for all cycled cells ranged from 0.005 to 1.5 V for anode half cell and 3 to 4.3 V for cathode half cell and full cell versus Li/Li^+. The electrolyte was comprised of 1.3M LiPF6 in 3:7 v/v ethylene carbonate/diethyl carbonate with 10 wt% fluorinated ethylene carbonate additives to improve the cycling stability. Polyethylene film (Celgard 2400) was used as a separator. These were all carefully assembled in an Ar-filled glove box. After cycling, each cell was opened in the glove box and washed with dimethyl carbonate to remove residual electrolyte and any other impurities. Then it was dried at room temperature. Galvanostatic discharge/charge test results were made by a WBCS3000K8 (WonATech Co., Ltd.). EIS measurements were carried out between 10 000-0.1 Hz with an amplitude of 10 mV at a fully-delithiated state (~1.2 V).

2.3 Results and discussion

Synthetic procedure of wet-oxidized Al-Si (denoted as ASWO-X, X for remaining amount of Al after acid etching) is briefly described in Fig. 2-1. Bare Al-Si alloy has a spherical structure with broad size distribution (1-10 μm) presenting dense surface (Fig. S1, ESI†). X-ray diffraction (XRD) pattern of pristine Al-Si alloy exhibits distinct peaks for Al and Si without any impurities (Fig. S1d, ESI†).

Firstly, the etched Al-Si alloy were prepared from commercial Al-Si alloy by HCl treatment, which selectively reacts with Al, leading to the porous micro-Si particles with Al residue distributed randomly over the spheres. Four different types of etched Al-Si samples with varied Al amounts (4, 10, 20 and 40 wt%) were obtained by a facile control of etching time (60, 45, 30 and 20 min) (Fig. S2, ESI†). Gradual decreasing trend in Al contents was also verified by XRD analysis along with stationary Si peaks (Fig. S3, ESI†). From the scanning electron microscopy (SEM) images, tightly blocked structure is shown with more porosity during acid treatment (Fig. S2a-d, ESI†). Etching started from the edges of Al-Si alloy to the cores, which reveals uniform distribution of Al element covering micron-sized Al-Si alloy. As HCl etchant was soaked into the Al-Si alloy, it left numerous mesopores which looks like a foam structure with significantly increased Brunauer-Emmett-Teller (BET) surface area of 62.1 m^2g^{-1} in case of Al-Si-4 sample, compared to pristine Al-Si alloy (0.58 m^2g^{-1}) (Fig. S4, ESI†). The evolution of porous architecture was clearly corroborated by transmission electron microscopy (TEM), scanning transmission electron microscopy (STEM) - high angle annular dark field (HAADF) images and energy-dispersive X-ray spectroscopy (EDX) analysis (Fig. S5, ESI†). The EDX mapping results show that Al-rich phases are observed in the core region, while Si framework is not dependent on etching time (Fig. S5d, 5h, 5l and 5p, ESI†). In addition, highly crystalline phase of etched Al-Si alloy with characteristic d-spacing values of 0.32 nm and 0.21 nm for Si and Al, respectively, was not damaged at all after whole etching process.

Subsequently, thermal oxidation process at 600 °C for 40 min in a wet atmosphere was carried out to introduce amorphous Al_2O_3 layers on the etched Al-Si samples. Unlike etched Al-Si samples, ASWO lose its fine spherical structure in case of containing a large amount of Al, demonstrating that excessive formation of Al_2O_3 layers partially prevent the spherical shape (Fig. S6a-d, ESI†). It has been known that oxygen vapour hardly oxidized Si at this condition, while it prefer to combine with Al.[41] As expected, a series of ASWO samples were successfully oxidized showing high oxygen compositions through wet-oxidation compared to etched Al-Si (Fig. S6e, ESI†).

To investigate specific wet-oxidation mechanism and how it affects overall structure, ASWO samples were characterized by TEM, STEM-HAADF and EDX mapping techniques (Fig. 2-2). Two major differences arising from wet-oxidation process are evolution of structural asymmetry which mainly contributed to Al diffusion at elevated temperature and formation of thin Al_2O_3 layers on the outer shells.

Melting temperature of Al (~660 ºC) is pretty close to the working temperature (~600 ºC), which Al can partially diffuse from the core and also outer shells at the same time. This phenomenon gets worse at larger Al amounts, so that anisotropic diffusion of Al was observed only in case of ASWO-20 and ASWO-40 samples. It can be primarily contributed to densely condensed Al element at the core and additionally unidirectional flow of vapours during the wet-oxidation. As a result, asymmetric distribution of Al was observed in both samples even though appropriate Al_2O_3 layers were formed on the outer shells (Fig. 2-2i-p). From the EDX mapping results of oxygen, above two samples contain a large portion of pure Al at the core and diffused Al formed excessive passivation layers which will disrupt lithium ion diffusion later. Meanwhile, ASWO-04 sample did not show distinctive change in morphology and elemental distribution (Fig. 2-2a, c-d). Instead, passivation layers could not be formed on the shells due to not enough amount of Al indicating that mechanical failure of typical problem of Si cannot be mitigated (Fig. 2-2b). Synthetically, ASWO-20 sample strongly manifests ideal formation of Si-based multicomponent system. There was no asymmetry in structure and Al distribution with amorphous Al_2O_3 layers firmly coated (Fig. 2-2e-h). As mentioned, Al is supposed to diffuse from core to outer shells and unavoidably Al loss occurred in all of the samples. Assuming no change in Si contents, we can simply calculate the ratio of Si to Al before and after wet-oxidation. Obviously, Al loss took place irrespective of remained Al amounts, which ASWO-10 sample particularly showed the lowest level of loss (Fig. S6f, ESI†). This means diffusion kinetic of vapour and Al gets well-balanced to minimize the loss of building novel structure.

Along with structural analysis, the transition of crystal structure in ASWO samples was identified by XRD and Raman analysis (Fig. 2-3). Strong diffraction peaks are assigned to polycrystalline phase of Si (JCPDS 13-0558) and metallic Al (JCPDS 89-4037), respectively, along with newly formed small peaks of Al2O3 (JCPDS 29-0063) in case of ASWO-20 and ASWO-40.[42-44] It is attributed to thicker formation of Al_2O_3 layers in outer shells from diffused Al, which will increase the surface resistance. Likewise, Raman spectrum also shows typical crystalline Si peaks located at 303 cm^{-1}, 520 cm^{-1}, 950 cm^{-1} found in bulk Si, while Al-related peaks are overlapped with Si peaks at around 300 cm^{-1}, due to high intensity of Si. In addition, trace of Al_2O_3 layers were merely detected because of poor crystallinity and small amounts.[45, 46]

Nitrogen adsorption analysis reveals that macropores of >50 nm in foam-like structure is maintained even after wet-oxidation (Fig. S7, ESI†). However, tiny mesopores of <10 nm are slightly decreased through surface oxidation in Baraett-Joyner-Halenda (BJH) pore size distribution curves in accordance with TEM results (Fig. S7b, ESI†). From the loss of pores, BET surface was recorded fairy lower values in ASWO group (ASWO-4 : 61.3 m^2g^{-1}, ASWO-10 : 34.9 m^2g^{-1}, ASWO-20 : 23.1 m^2g^{-1}, ASWO-40 : 13.3 m^2g^{-1}) compared to etched Al-Si group (Al-Si-04 : 62.1 m^2g^{-1}, Al-Si-10 : 51.2 m^2g^{-1}, Al-Si-20 : 27.6 m^2g^{-1}, Al-Si-40 : 20.6 m^2g^{-1}). The more Al_2O_3 layers were formed, the larger decrease of surface area was observed.

Given careful and elaborate analysis, structural integrity consisting of porous micro-Si and appropriate level of passivation layers has been realized in ASWO-10 sample as a novel Si-multicomponent system. To evaluate electrochemical properties of ASWO electrodes, 2016R coin-type half cells comprising Li-metal as a counter electrode were fabricated. The galvanostatic first cycle charge/discharge curve in the potential range of 0.005 – 1.5 V at a rate of C/20 is described (Fig. 2-4a). In order to investigate exactly how passivation layers influence on its electrochemical properties, we also prepared several cells assembled with etched Al-Si samples. The poor coulombic efficiency and capacity decaying of electrodes containing a large portion of Al are ascribable to its detrimental effect on the interface (Fig. S8a and S8b, ESI†). On the other hands, a series of ASWO electrodes showed relatively lower reversible specific capacity of 1420.0 mAh g^{-1}, 1278.6 mAh g^{-1}, 1171.8 mAh g^{-1} and 724.0 mAh g^{-1} corresponding to initial coulombic efficiency (ICE) of 80.1%, 78.8%, 76.1% and 75.1% for ASWO-04, ASWO-10, ASWO-20, and ASWO-40, respectively. At an expense of forming Al_2O_3 layers, the capacity decreases. However, the Al_2O_3 layers can prevent the direct side reaction of metallic Al with electrolyte, so that ASWO electrodes show suitable ICE and capacity values for Si/inactive composite materials.[21, 22, 33]

As the synergistic effect of porous structure and uniform passivation layers, outstanding cycling stability at a rate of 0.2 C in case of ASWO electrodes were obtained against etched Al-Si electrodes (Fig. 2-4b). Interfacial instability which brought about in absence of Al_2O_3 layers resulted in serious capacity drop and fluctuating coulombic efficiency (Fig. S8c, ESI†). Meanwhile, the ASWO-10 electrode shows capacity retention of 81.9% after 500 prolonged cycles with a high capacity of ~810 mAh g^{-1}. Others are listed as follows; the final capacity of 875.8 mAh g^{-1} (79.1%, ASWO-04), 388.4 mAh g^{-1} (45.6%, ASWO-20) and 126.3 mAh g^{-1} (23.9%, ASWO-40) after 500 cycles. This comparable result of ASWO-10 electrode demonstrates that its symmetrical Al core shell helped to sustain the original structure and uniform SEI formed at early stage of cycling guaranteeing structural integrity. Instead, excessive formation of insulating layers on porous Si structure brought about limited capacity and caused structural failure in cases of ASWO-20 and ASWO-40 electrodes. Similarly, moderately formed Al_2O_3 layers in ASWO-10

can enhance the lithium ion diffusion through Li-Al-O intermediate layers rather than acting as a barrier of lithium ion in case of ASWO-20 and ASWO-40, which can be corroborated by rate capability test varying charge rate at a fixed discharge rate of C/5 (Fig. 2-4c). ASWO-20 and ASWO-40 showed uninspiring rate performance (the capacity drop ratio from 0.2 C to 5 C were 19.7% and 47.7%, respectively), while ASWO-04 and ASWO-10 achieved impressive results (6.23% and 7.21%) accompanied by full recovery except ASWO-40.

To further verify the effects of Al_2O_3 passivation layers, electrochemical impedance spectroscopy (EIS) analysis was conducted for all the ASWO electrodes at different stages before and after 1st, 2nd and 3rd cycling (Fig. 2-4d and Fig. S9, ESI†). For the pristine electrodes, all has a high charge transfer resistance over 100 Ω due to the absence of SEI layer, which can be also ascribed to poor electron and lithium ion conducting property of silicon observed in typical silicon-based anode materials.[47] Compared to other electrodes except ASWO-4, all the electrodes have similar charge transfer resistance in fresh cells. In case of ASWO-4, it is worth noting that almost negligible amounts of passivation layers rather hinder the surface kinetics although alumina has insulating nature by any means. This can be attributed to the fact that our passivation layers are amorphous, not fully crystallized. It was settled down after first cycle, in which ASWO-10 has the lowest charge transfer and SEI resistance because it has uniformly formed SEI layers. Before formation cycles (or 1st cycle), there was no efficient pathway for lithium ions and then randomly approached lithium ions may increase the charge transfer resistance. However, SEI layers provides the channels for lithium ions and help to react with silicon materials evenly over the structure, which prevent direct contact of liquid electrolyte. Without SEI formation, electrolytes are continuously decomposed to make thicker SEI layers, adversely impeding lithium ion kinetics. Those behaviour is observed in case of ASWO-4 and ASWO-40. From subsequent cycles, interface of ASWO-10 was stabilized very fast to show distinguishable two semicircles. The newly formed circles can be assigned to effects of lithiated alumina and uniform SEI covering all the active materials, while others showed dramatically increased resistance, which seemed to be broken and continuous SEI formation getting thicker.

One of the key issues on Si-based anode materials is how to effectively mitigate a huge volume expansion during cycling in terms of electrode and materials itself. In the same vein, electrode swelling problem is significantly resolved in case of ASWO-10 electrode (expansion of 15.4% in the full-lithiation and 18.2% after 30 cycles at a rate of 0.2 C), while other electrodes cannot be effectively mediated exhibiting 53.3% (85.7%) for ASWO-04, 39.0% (37.4%) for ASWO-20 and 85.1% (89.1%) for ASWO-40, respectively, for full-lithiation (after 30 cycles) (Fig. 2-5 and S11).

In addition, change in macrostructures was clearly shown (Fig. S12, ESI†). For example, ASWO-04 lost its spherical structure due to absence of core and passivation layers (Fig. S11a,

ESI†). ASWO-20 has closed structure and ASWO-40 is covered with lots of by-products (Fig. S11c and d, ESI†). However, ASWO-10 still shows a porous spherical structure, which was supported by homogeneously distributed Al core and effective passivation effect from Al2O3 layers within the Si framework.

To demonstrate the feasibility of ASWO electrode in full cell configuration, a coin-type full cell (2032R) coupled with $LiCoO_2$ (LCO) cathode and ASWO-X/NG anode was investigated (Fig. 2-6). The structure and electrochemical performance of LCO is displayed in Fig. S12 (ESI†). In case of anode, ASWO samples were blended with natural graphite to balance with LCO cathode, which delivered a reversible capacity of ~600 mAh g^{-1} after 100 cycles at a rate of C/5 (Fig. S13, ESI†). This assembled full cell was tested with potential window of 3-4.3V. The full cell consisting of ASWO-10/NG anode shows the most notable electrochemical results including ICE of 91.0% in the first charge/discharge profiles (Fig. 2-6a inset) and negligible capacity decay after 200 cycles at a rate of 1 C delivering 0.744 mAh cm^{-2} corresponding to the capacity retention of 75.3% (Fig. 2-6a). This capacity retention is similar to that of ASWO and ASWO/NG electrodes. Nevertheless, at such a high C-rate, this full cell can still work with a high reversible capacity of 0.744 mAh cm^{-2} comparing to other coupled full cells (Fig. S14, ESI†). Rate capability of the full-cell was also investigated by varying charge-discharge rates from C/10 to 5C for each 5 cycles (Fig. 2-6b). Unlike observed trend in ASWO half cell, specific capacities of full cell decreased gradually with the increasing current density due to rising polarization. This also can be attributed to a limited durability of cathode. Interestingly, coulombic efficiency after 200 cycles reached 99.94% and average coulombic efficiency during prolonged cycles is over 99% discarding the first, implying that LCO/ASWO-10/NG full cell can compare favourably with other Si-based composite materials. This remarkable electrochemical result may be attributed to unique structured Si-based multicomponent consisting of porous Si passivated with thin Al_2O_3 layers. Furthermore, to date silicon materials have been utilized in a form of additive for graphite-based anode materials to increase the specific capacity of cell. Even though several nanostructured Si anodes are demonstrated to have outstanding electrochemical performances, still it requires complex and exquisite process with high price. However, pristine Al-Si alloy is commercially available in relatively lower price and only some experimental set-ups for wet chemical etching and annealing chamber are included to produce unique porous architecture of Si multicomponent, where no wonder our approach is definitely cost-effective among various synthetic methods. Additionally, its electrochemical performances are comparable to those of other previous reports (Table S2, ESI†).

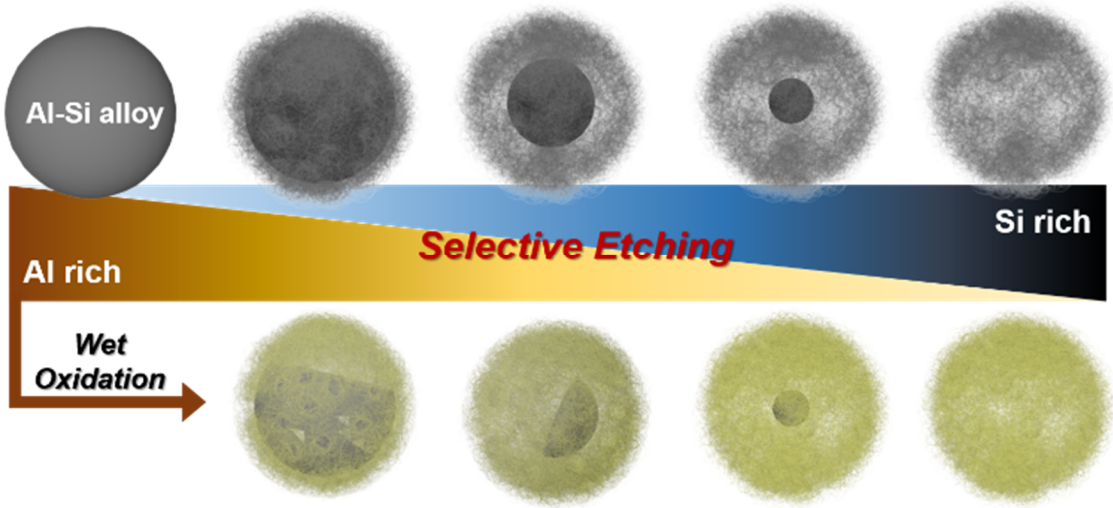

Figure 2-1. Schematic illustration of synthetic approach for Si-based multicomponent from commercial Al-Si alloy through selective etching and wet-oxidation**.**

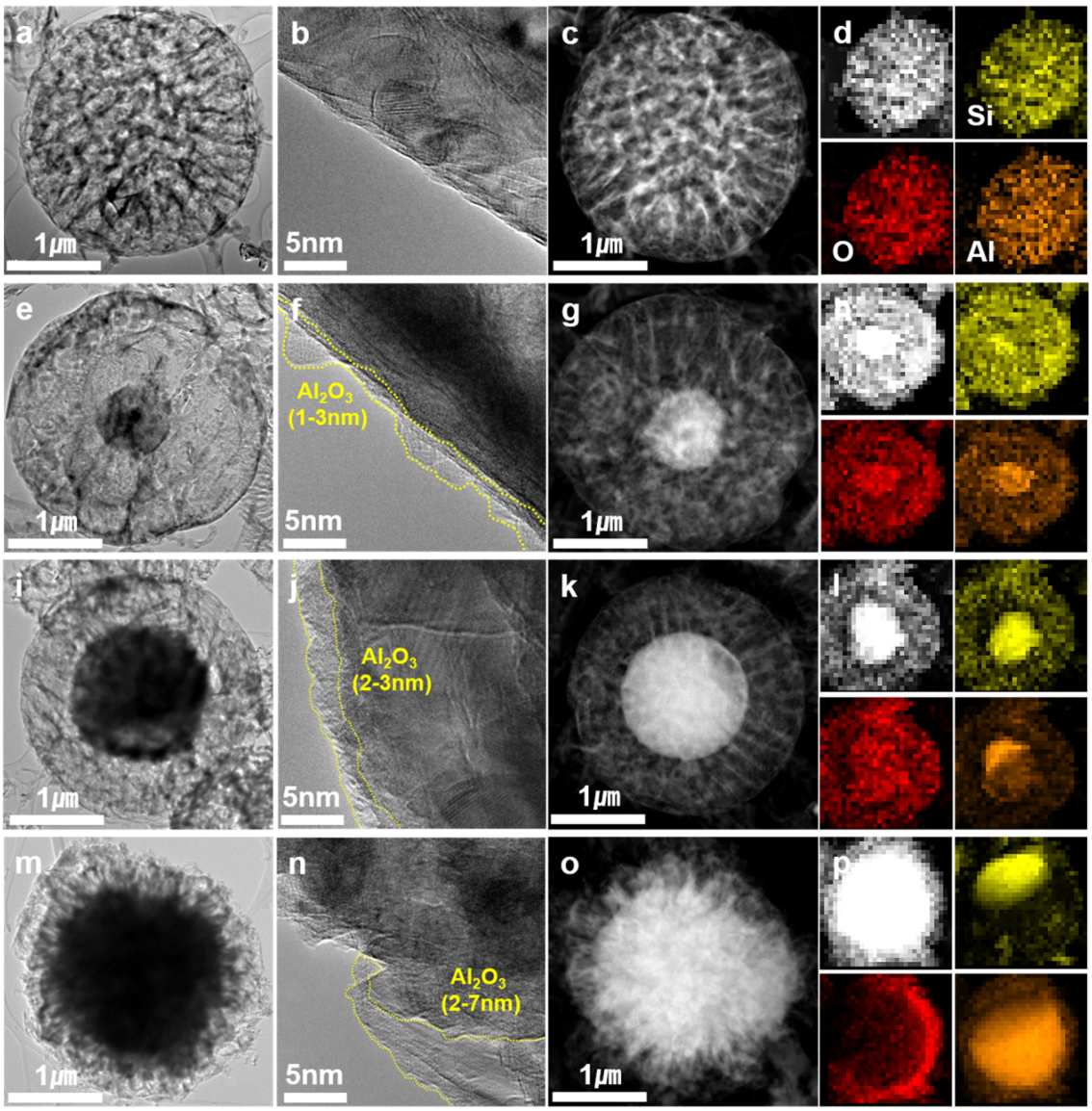

Figure 2-2. Structural characterization of a series of wet-oxidized etched Al-Si (ASWO). TEM images, STEM-HAADF image and EDX mapping data for (a-d) ASWO-04, (e-h) ASWO-10, (i-l) ASWO-20 and (m-p) ASWO-40 samples in regular order. Dotted lines (as visual aid) indicate amorphous Al_2O_3 layers on the surface.

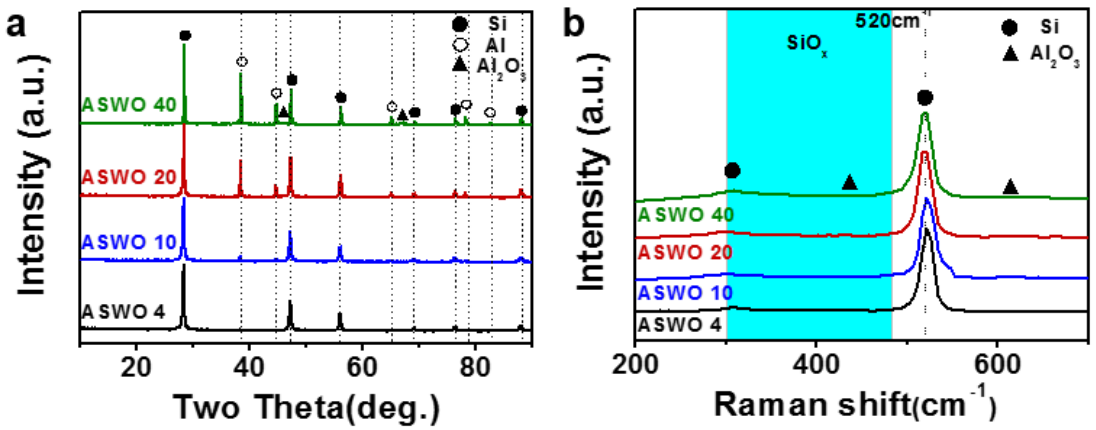

Figure 2-3. Physical properties of wet-oxidized etched Al-Si (ASWO). (a) XRD pattern and (b) Raman spectrum of ASWO.

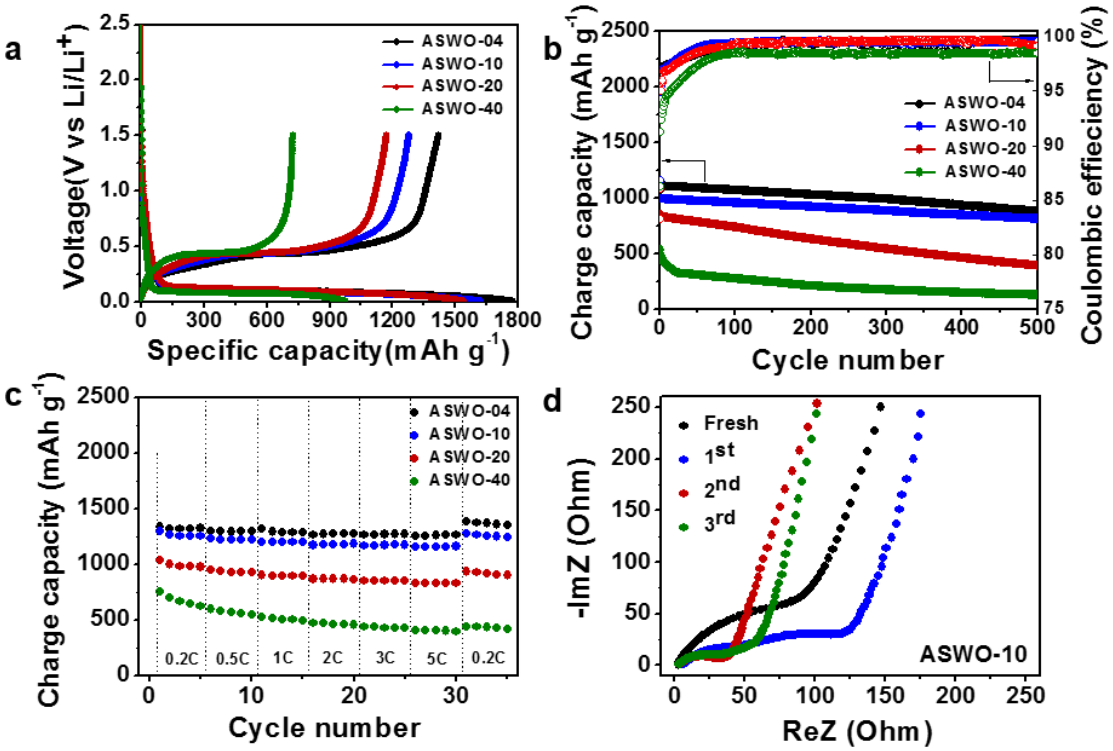

Figure 2-4. Electrochemical properties of ASWO in half cell. (a) Galvanostatic first cycle charge/discharge voltage profiles at a rate of C/20 in the potential window of 0.005-1.5V, (b) cyclic performances for 500 cycles at a rate of C/5, (c) rate capability of ASWO electrodes at various current density and (d) ex-situ impedance analysis of ASWO-10 electrode (pristine, first, second, and third cycled electrodes).

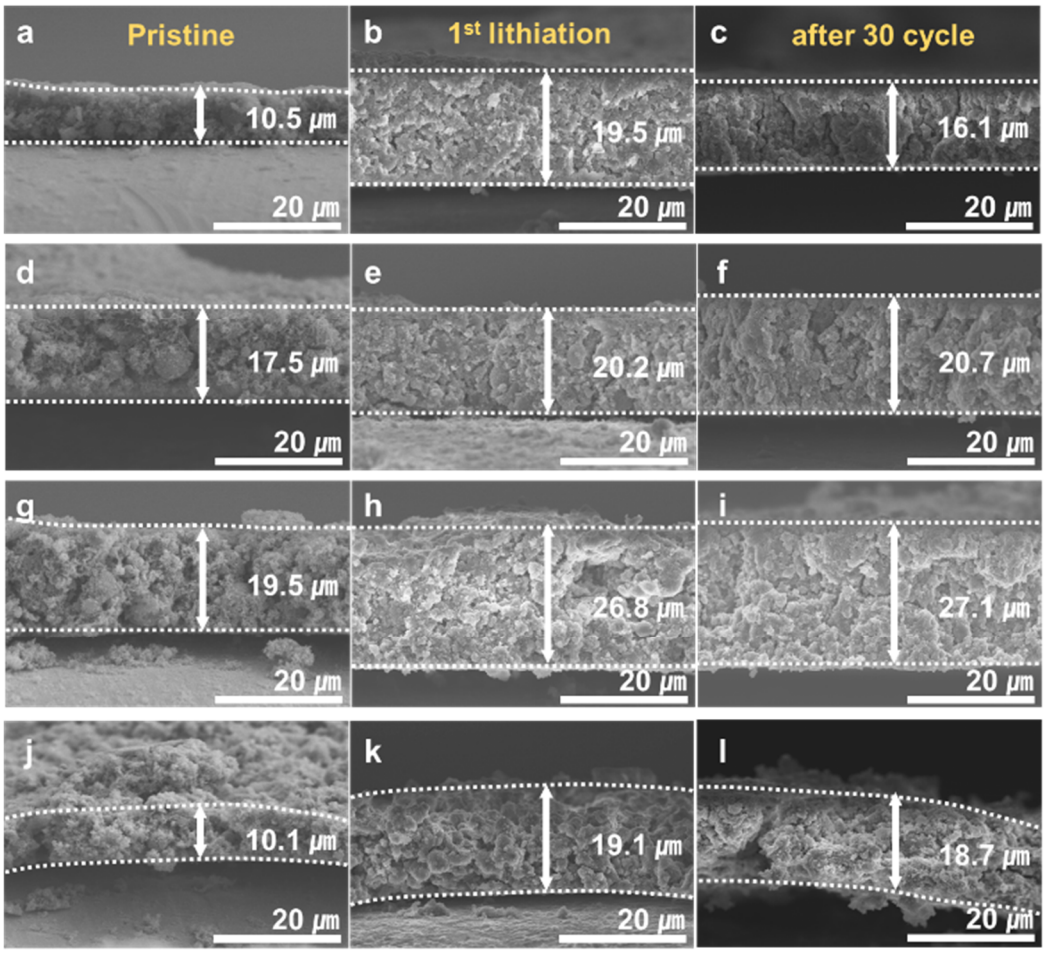

Figure 2-5. Electrode swelling results of ASWO series. SEM images of ASWO (a-c) 04, (d-f) 10, (g-i) 20 and (j-l) 40, respectively for pristine, after 1st lithiation and after 30 cycles.

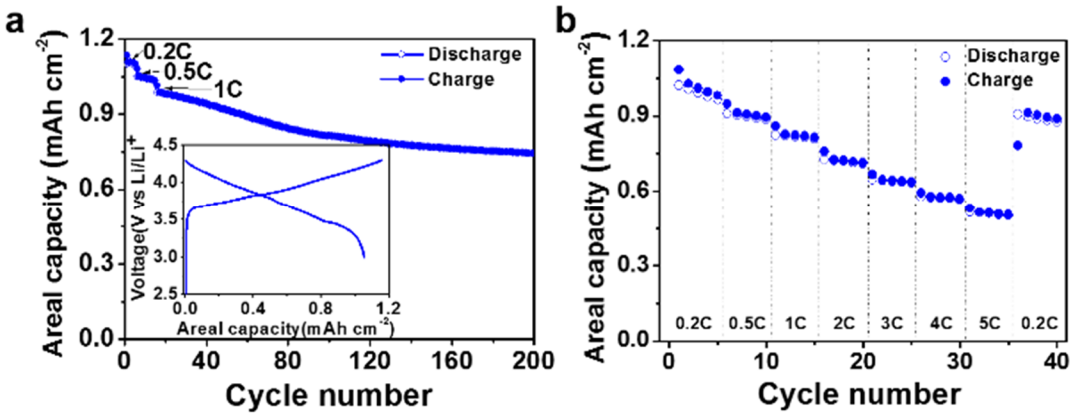

Figure 2-6. Electrochemical properties of $LiCoO_2$‖ASWO-10/NG full cell. (a) Cycling performance at 1C rate after 200 cycles (inset. first cycle charge-discharge profiles at C/10 rate) and (b) Rate capability of $LiCoO_2$‖ASWO-10/NG full cell.

2.4 Conclusion

The novel architecture comprised of porous foam-like Si passivated by suitable range of thin Al_2O_3 layers has been successfully fabricated through selective acid etching and subsequent wet-oxidation utilizing commercial Al-Si alloy. Centralized Al metal will diffuse to the outer shell to form passivation layers evenly over the Si framework, which left behind Al core as a support to retain macrostructure. During electrochemical measurement, thin Al_2O_3 layers effectively suppress direct contact of Si surface with electrolyte and simultaneously enhance the lithium ion diffusion through lithium ion-conducting layers to introduce stable and uniform SEI. In the half cell test, ASWO-10 electrodes exhibited capacity retention of 81.9% after 500 cycles at C/5 along with excellent rate capability (92.5% retention at 5C). Similar trend was also observed in ASWO blended with NG electrode, showing 98.2% retention after 100 cycles at C/5. Finally, the full cell consisting of ASWO-10/NG anode and LCO cathode delivers noticeable cycling stability of 75.3% after 200 cycles at such a high C-rate of 1C, validating promising anode materials for next-generation batteries. Our work promises a cost-effective approach for the novel structured Si-based multicomponent system.

2.5 Reference

1. Obrovac, M. N.; Christensen L. Structural changes in silicon anodes during lithium insertion/extraction. *Electrochem. Solid State Lett.* **2004,** *7*, A93-A96.
2. Li, J.; Dahn J. R. An in situ x-ray diffraction study of the reaction of li with crystalline si. *J. Electrochem. Soc.* **2007,** *154*, A156-A161.
3. Son, S. B.; Kim S. C.; Kang C. S.; Yersak T. A.; Kim Y. C.; Lee C. G.; Moon S. H.; Cho J. S.; Moon J. T.; Oh K. H.; Lee S. H. A highly reversible nano-si anode enabled by mechanical confinement in an electrochemically activated lixti4ni4si7 matrix. *Adv. Energy. Mater.* **2012,** *2*, 1226-1231.
4. Kasavajjula, U.; Wang C. S.; Appleby A. J. Nano- and bulk-silicon-based insertion anodes for lithium-ion secondary cells. *J. Power Sources* **2007,** *163*, 1003-1039.
5. Lee, W. J.; Hwang T. H.; Hwang J. O.; Kim H. W.; Lim J.; Jeong H. Y.; Shim J.; Han T. H.; Kim J. Y.; Choi J. W.; Kim S. O. N-doped graphitic self-encapsulation for high performance silicon anodes in lithium-ion batteries. *Energy Environ. Sci.* **2014,** *7*, 621-626.
6. Jung, H. J.; Park M.; Yoon Y. G.; Kim G. B.; Joo S. K. Amorphous silicon anode for lithium-ion rechargeable batteries. *J. Power Sources* **2003,** *115*, 346-351.
7. Mukherjee, R.; Krishnan R.; Lu T. M.; Koratkar N. Nanostructured electrodes for high-power lithium ion batteries. *Nano Energy* **2012,** *1*, 518-533.
8. Bruce, P. G.; Scrosati B.; Tarascon J. M. Nanomaterials for rechargeable lithium batteries. *Angew. Chem. Int. Ed.* **2008,** *47*, 2930-2946.
9. Arico, A. S.; Bruce P.; Scrosati B.; Tarascon J. M.; Van Schalkwijk W. Nanostructured materials for advanced energy conversion and storage devices. *Nat. Mater.* **2005,** *4*, 366-377.
10. Dai, F.; Zai J. T.; Yi R.; Gordin M. L.; Sohn H.; Chen S. R.; Wang D. H. Bottom-up synthesis of high surface area mesoporous crystalline silicon and evaluation of its hydrogen evolution performance. *Nat. Commun.* **2014,** *5*,
11. Wada, T.; Ichitsubo T.; Yubuta K.; Segawa H.; Yoshida H.; Kato H. Bulk-nanoporous-silicon negative electrode with extremely high cyclability for lithium-ion batteries prepared using a top-down process. *Nano Lett.* **2014,** *14*, 4505-4510.
12. Lin, Y. M.; Klavetter K. C.; Abel P. R.; Davy N. C.; Snider J. L.; Heller A.; Mullins C. B. High performance silicon nanoparticle anode in fluoroethylene carbonate-based electrolyte for li-ion batteries. *Chem. Commun.* **2012,** *48*, 7268-7270.
13. Ryou, M. H.; Kim J.; Lee I.; Kim S.; Jeong Y. K.; Hong S.; Ryu J. H.; Kim T. S.; Park J. K.; Lee H.; Choi J. W. Mussel-inspired adhesive binders for high-performance silicon

nanoparticle anodes in lithium-ion batteries. *Adv. Mater.* **2013,** *25*, 1571-1576.

14. Zamfir, M. R.; Nguyen H. T.; Moyen E.; Lee Y. H.; Pribat D. Silicon nanowires for li-based battery anodes: A review. *J. Mater. Chem. A* **2013,** *1*, 9566-9586.
15. Chan, C. K.; Peng H. L.; Liu G.; McIlwrath K.; Zhang X. F.; Huggins R. A.; Cui Y. High-performance lithium battery anodes using silicon nanowires. *Nat. Nanotechnol.* **2008,** *3*, 31-35.
16. Park, M. H.; Kim M. G.; Joo J.; Kim K.; Kim J.; Ahn S.; Cui Y.; Cho J. Silicon nanotube battery anodes. *Nano Lett.* **2009,** *9*, 3844-3847.
17. Wu, H.; Chan G.; Choi J. W.; Ryu I.; Yao Y.; McDowell M. T.; Lee S. W.; Jackson A.; Yang Y.; Hu L. B.; Cui Y. Stable cycling of double-walled silicon nanotube battery anodes through solid-electrolyte interphase control. *Nat. Nanotechnol.* **2012,** *7*, 309-314.
18. Ryu, J.; Hong D.; Choi S.; Park S. Synthesis of ultrathin si nanosheets from natural clays for lithium-ion battery anodes. *ACS Nano* **2016,** *10*, 2843-2851.
19. Su, L. W.; Jing Y.; Zhou Z. Li ion battery materials with core-shell nanostructures. *Nanoscale* **2011,** *3*, 3967-3983.
20. Yi, R.; Dai F.; Gordin M. L.; Sohn H.; Wang D. H. Influence of silicon nanoscale building blocks size and carbon coating on the performance of micro-sized si-c composite li-ion anodes. *Adv. Energy. Mater.* **2013,** *3*, 1507-1515.
21. Luo, W.; Wang X. F.; Meyers C.; Wannenmacher N.; Sirisaksoontorn W.; Lerner M. M.; Ji X. L. Efficient fabrication of nanoporous si and si/ge enabled by a heat scavenger in magnesiothermic reactions. *Sci. Rep.* **2013,** *3*,
22. Chen, H. T.; Xu J.; Chen P. C.; Fang X.; Qiu J.; Fu Y.; Zhou C. W. Bulk synthesis of crystalline and crystalline core/amorphous shell silicon nanowires and their application for energy storage. *ACS Nano* **2011,** *5*, 8383-8390.
23. Wang, B.; Li X. L.; Zhang X. F.; Luo B.; Zhang Y. B.; Zhi L. J. Contact-engineered and void-involved silicon/carbon nanohybrids as lithium-ion-battery anodes. *Adv. Mater.* **2013,** *25*, 3560-3565.
24. Chen, D. Y.; Mei X.; Ji G.; Lu M. H.; Xie J. P.; Lu J. M.; Lee J. Y. Reversible lithium-ion storage in silver-treated nanoscale hollow porous silicon particles. *Angew. Chem. Int. Ed.* **2012,** *51*, 2409-2413.
25. Cho, J. Porous si anode materials for lithium rechargeable batteries. *J. Mater. Chem.* **2010,** *20*, 4009-4014.
26. Tan, L.; Zhang S.; Deng C. Fast lithium intercalation chemistry of the hierarchically porous li2fep2o7/c composite prepared by an iron-reduction method. *J. Power Sources* **2015,** *275*, 6-13.

27. Meng, Y.; Yu T. T.; Zhang S.; Deng C. Top-down synthesis of muscle-inspired alluaudite na2+2xfe2-x(so4)(3)/swnt spindle as a high-rate and high-potential cathode for sodium-ion batteries. *J. Mater. Chem. A* **2016,** *4*, 1624-1631.
28. Zheng, Y.; Yang J.; Wang J. L.; NuLi Y. N. Nano-porous si/c composites for anode material of lithium-ion batteries. *Electrochim. Acta* **2007,** *52*, 5863-5867.
29. Liu, Y.; Wen Z. Y.; Wang X. Y.; Yang X. L.; Hirano A.; Imanishi N.; Takeda Y. Improvement of cycling stability of si anode by mechanochemcial reduction and carbon coating. *J. Power Sources* **2009,** *189*, 480-484.
30. Kim, T.; Park S.; Oh S. M. Preparation of core-shell si/nisi2/carbon composite and its application to lithium secondary batteries. *Electrochem. Commun.* **2006,** *8*, 1461-1467.
31. Chen, Y.; Qian J. F.; Cao Y. L.; Yang H. X.; Ai X. P. Green synthesis and stable li-storage performance of fesi2/si@c nanocomposite for lithium-ion batteries. *ACS Appl. Mater. Interaces* **2012,** *4*, 3753-3758.
32. Luo, J. Y.; Zhao X.; Wu J. S.; Jang H. D.; Kung H. H.; Huang J. X. Crumpled graphene-encapsulated si nanoparticles for lithium ion battery anodes. *J. Phys. Chem. Lett.* **2012,** *3*, 1824-1829.
33. Liu, B.; Wang X. F.; Chen H. T.; Wang Z. R.; Chen D.; Cheng Y. B.; Zhou C. W.; Shen G. Z. Hierarchical silicon nanowires-carbon textiles matrix as a binder-free anode for high-performance advanced lithium-ion batteries. *Sci. Rep.* **2013,** *3*,
34. Lahiri, I.; Oh S. M.; Hwang J. Y.; Kang C.; Choi M.; Jeon H.; Banerjee R.; Sun Y. K.; Choi W. Ultrathin alumina-coated carbon nanotubes as an anode for high capacity li-ion batteries. *J. Mater. Chem.* **2011,** *21*, 13621-13626.
35. Li, Y.; Sun Y. J.; Xu G. J.; Lu Y.; Zhang S.; Xue L. G.; Jur J. S.; Zhang X. W. Tuning electrochemical performance of si-based anodes for lithium-ion batteries by employing atomic layer deposition alumina coating. *J. Mater. Chem. A* **2014,** *2*, 11417-11425.
36. Xiao, X. C.; Lu P.; Ahn D. Ultrathin multifunctional oxide coatings for lithium ion batteries. *Adv. Mater.* **2011,** *23*, 3911-3915.
37. Li, B.; Yao F.; Bae J. J.; Chang J.; Zamfir M. R.; Le D. T.; Pham D. T.; Yue H.; Lee Y. H. Hollow carbon nanospheres/silicon/alumina core-shell film as an anode for lithium-ion batteries. *Sci. Rep.* **2015,** *5*, 7659.
38. Nguyen, H. T.; Zamfir M. R.; Duong L. D.; Lee Y. H.; Bondavalli P.; Pribat D. Alumina-coated silicon-based nanowire arrays for high quality li-ion battery anodes. *J. Mater. Chem.* **2012,** *22*, 24618-24626.
39. He, Y.; Yu X. Q.; Wang Y. H.; Li H.; Huang X. J. Alumina-coated patterned amorphous silicon as the anode for a lithium-ion battery with high coulombic efficiency. *Adv. Mater.* **2011,** *23*,

4938-4941.

40. Kim, S. O.; Manthiram A. A facile, low-cost synthesis of high-performance silicon-based composite anodes with high tap density for lithium-ion batteries. *J. Mater. Chem. A* **2015,** *3*, 2399-2406.
41. Hwang, G.; Park H.; Bok T.; Choi S.; Lee S.; Hwang I.; Choi N. S.; Seo K.; Park S. A high-performance nanoporous si/al2o3 foam lithium-ion battery anode fabricated by selective chemical etching of the al-si alloy and subsequent thermal oxidation. *Chem. Commun.* **2015,** *51*, 4429-4432.
42. Mukherjee, S.; Berger L. Switching of composite media by wall propagation. *J. Appl. Phys.* **2006,** *99*, 08Q909.
43. Rashad, M.; Pan F. S.; Tang A. T.; Asif M. Effect of graphene nanoplatelets addition on mechanical properties of pure aluminum using a semi-powder method. *Prog. Nat. Sci. Mater.* **2014,** *24*, 101-108.
44. Boumaza, A.; Favaro L.; Ledion J.; Sattonnay G.; Brubach J. B.; Berthet P.; Huntz A. M.; Roy P.; Tetot R. Transition alumina phases induced by heat treatment of boehmite: An x-ray diffraction and infrared spectroscopy study. *J. Solid. State. Chem.* **2009,** *182*, 1171-1176.
45. Khorasaninejad, M.; Walia J.; Saini S. S. Enhanced first-order raman scattering from arrays of vertical silicon nanowires. *Nanotechnology* **2012,** *23*, 275706.
46. Naglieri, V.; Joly-Pottuz L.; Chevalier J.; Lombardi M.; Montanaro L. Follow-up of zirconia crystallization on a surface modified alumina powder. *J. Eur. Ceram. Soc.* **2010,** *30*, 3377-3387.
47. Radvanyi, E.; Van Havenbergh K.; Porcher W.; Jouanneau S.; Bridel J. S.; Put S.; Franger S. Study and modeling of the solid electrolyte interphase behavior on nano-silicon anodes by electrochemical impedance spectroscopy. *Electrochim. Acta* **2014,** *137*, 751-757.

Chapter III. Hybridizing germanium anodes with polysaccharide-derived nitrogen-doped carbon for high volumetric capacity of Li-ion batteries

3.1 Introduction

The looming depletion of fossil fuels and grave environmental issues raised energy challenges. As a result, a significant demand has been made for highly efficient energy storage systems.[1] Rechargeable Li-ion batteries (LIBs) have been demonstrated as one of the most reliable devices in a wide range of applications such as mobile electronics and electric vehicles in the past few decades.[2] In order to further meet the stringent requirements, extensive researches have been dedicated to developing new electroactive materials and their derivatives with high gravimetric/volumetric energy density, which can be hardly achievable by current carbon-based materials. Among various candidates, group IV elements (in particular, Si and Ge) showing a high degree of lithiation (LixM, where $x \geq 3.75$) have theoretical capacities of 3579 mAh g^{-1} ($x=3.75$ for Si) and 1600 mAh g^{-1} ($x=4.4$ for Ge), respectively, which is far beyond that of graphite anodes.[3-7] Although Ge exhibits several disadvantages of low capacity, less abundance, and expensive price compared to Si, the Li-ion diffusivity and electronic conductivity of Ge are much greater than those of Si,[8-11] which indicates that Ge could be an promising active material for high-power battery anodes.[12-15]

Nonetheless, as the typical Li-alloying anodes do, Ge undergoes a large volume change of 370% during Li-ion uptake.[1, 7, 16] This causes a serious mechanical failure, resulting in a rapid degradation of electrochemical performance, and hinders the actual utilization of the Ge anode in both high-power and high-energy battery, of which are main issues to be overcome.[7, 17, 18] To address the above challenges, various approaches have been suggested by miniaturizing Ge in nanoscale (e.g., nanowires,[19-22] nanotubes,[23] porous structures,[13, 24-28] and thin film[8]) and by introducing buffer layers on outermost surface of Ge. From significant studies, it has been shown that different dimensionality significantly affects cycle retention of Ge anodes by relieving a mechanical stress and preventing pulverization of electrode materials. The reduced size gives a large surface area for the redox reactions and electron transfer between the battery components.[13, 29-34] For example, Ngo *et al.* reported a simple synthesis process of Ge particles interconnected by carbon buffer layer, in which GeO_2 and citric acid were used as precursors for Ge and the buffer layers, respectively.[31] Depending on the thermal annealing conditions, they fabricated

different composite materials with an exceptional cycling stability which was enabled by low loading level (<0.5 mg cm^{-2}). Recently, Li *et al.* synthesized a unique structure of Ge nanoparticles in carbon nanoboxes showing structural integrity over hundreds of cycles at a low loading level of 0.8 mg cm^{-2}.[32] In addition, several studies have shown improved cyclability, excellent rate capabilities, and high-rate durability, while Ge anode with a high volumetric energy has not been disseminated yet.

While light-weight and inexpensive carbon buffer layers provide substantial advantages for Ge anodes, it is believed that most of the carbon does not participate in the redox reaction. As a result, loss of specific energy inevitably occurs. If a large portion of active materials are covered with a carbon layers, improved electrochemical properties are obviously guaranteed. The use of different types of carbon materials (e.g., graphene, reduced graphene oxide, and carbon nanotube) will redeem these points at the expense of increased manufacturing costs.[35-37] In this regard, Ge-based materials, particularly in combination with a carbon buffer layer, are effective anode materials to use completely the energy which generated from both Ge and carbon derivatives.

Herein, we demonstrate a simple way to hybridize a Ge anode with a natural carbon source. A polysaccharide, particularly an agarose gel coupled with a nitrogen-containing polymer, conformally encapsulates commercially available GeO_2 particles. During the subsequent thermal annealing process, carbonization gradually occurs to form nitrogen-doped carbon buffer, while GeO_2 is reduced to Ge nanoparticles (GeNPs) by carbothermic reaction. This self-organized unique structure realizes the dimensional design of Ge anodes with nitrogen-doped carbon buffer layers enabled by cost-effective and environmentally-benign procedure. Agarose-derived nitrogen-doped hard carbon (ANHC) is important in electrodes that draw GeNPs together to produce micrometer-scale secondary particles, which resolve a typical problem of nanoparticles like low density. Also, spatial confinement prevents each Ge NPs from severe pulverization and promotes stable solid-electrolyte-interphase (SEI) formation by restricting direct contact of GeNPs with electrolytes. Hybridized ANHC/Ge anodes have a long-term operation in a Li-ion cell, showing capacity retention of ~100% after 500 cycles even with a high loading level (>4 mg cm^{-2}) in half-cell. Most notably, this research underlines a demonstration of high volumetric energy density (~1010 Wh/L) of ANHC/Ge/$LiCoO_2$ full cell recording unprecedented performance among various Ge-based Li-ion full cells.

3.2 Experimental

Preparation of ANHC/Ge

Agarose (Type I, Sigma-Aldrich) was dissolved in water at 90 ℃ for 1 h under vigorous stirring (solution A). When the solution A became transparent, it was transferred to solution B containing certain amounts of melamine-co-formaldehyde (MF, average molecular weight (Mn) = 432 g/mol, 84 wt% in n-butanol, Sigma-Aldrich) which is diluted by N,N-dimethyl formamide (DMF) at 110 ℃ for uniform mixing. Then, GeO_2 powder (99.999%, Germanium Corporation of America) was added to the solution (A+B) and stirred for 3 h to completely dissolve GeO_2. Then, the mixture was poured into the petri dish and immediately kept it in refrigerator for 30 mins. After complete gelation of solution, it was cut into small pieces for annealing and dried at 70 ℃ overnight. These gelated GeO_2/C cubes were annealed at 250 ℃ for 2 h in air (2 ℃ min^{-1} for stabilization, partially carbonized GeO_2/C cube), 500 ℃ for 1 h in argon (5 ℃ min^{-1} for crystallization of GeO_2, partially carbonized GeO_2/C cube), and 900 ℃ 2 h in argon (5 ℃ min^{-1} for carbothermic reduction, micro-sized Ge/C powder) in sequence. Then, the powders were collected and ball-milled for a short period of time to down-sizing (nano-sized Ge/C powder). Finally, outermost surface was coated with carbon via a typical chemical vapor deposition (CVD) method and it is now called ANHC/Ge. To make ANHC/GeO_2, we just skipped carbothermal process. Furthermore, different types of ANHC can be prepared without adding GeO_2 powders. In the absence of solution B and GeO_2, bare hard carbon materials named as AHC was prepared. At the end of the step, carbon coating via CVD process with acetylene gas was conducted for all the samples (AHC, ANHC, and ANHC/GeO_2). Also, pure Ge samples was easily produced by calcination of ANHC/Ge samples at 450 ℃ for 5 h in air.

Material Characterization

Scanning electron microscopy (SEM, Verios 460, FEI) was used to characterize the surface morphologies of AHC, ANHC, ANHC/GeO_2 and ANHC/Ge samples (ANHC/Ge series) at an acceleration voltage of 10 kV and current of 0.8 nA. The dimensions and internal structures of ANHC/Ge series were determined by transmission electron microscopy (TEM, JEOL-2100) and HRTEM (JEOL-2100C) at an acceleration voltage 200 kV. To investigate the microstructures and degrees of crystallinity of ANHC/Ge series, X-ray diffraction (XRD) analysis (D8 ADVANCE, Bruker) between 10° to 90° were performed using Cu-Kα radiation (λ = 1.5418 Å). Raman spectroscopy (alpha300R confocal microscope, WITec) was also employed for this purpose. The

BET surface area and pore sizes were characterized using automatic physisorption analyser (Micrometriticx, ASPS 2020). The amounts of carbon materials were determined by TGA (Thermogravimetric Analysis, TA-Q500). The XPS (ThermoFisher, K-alpha) analysis were carried out to obtain quantitative/qualitative information on surface oxidation state of ANHC/Ge series. Along with EDX and XPS quantification, C, N, and O amounts were determined by elemental analyzer (Thermo, Flash 2000).

Electrochemical Tests

To evaluate the electrochemical performances of ANHC/Ge series, coin-type half and full cells were fabricated using CR 2016 type cells in an argon-filled glove box. Slurry consisting of ANHC/Ge series, super-P carbon black, a mixture of poly(acrylic acid) (PAA, weight average molecular weight of 100 kg/mol, Aldrich) and sodium carboxymethyl cellulose (CMC, 6 wt% in H2O, Aldrich) (PAA/CMC = 1/1, wt/wt) as a binder with 8 : 1 : 1 mass ratio were prepared. The loading mass of AHC, ANHC, ANHC/Ge, and pure Ge electrodes were 2 mg cm^{-2}, 1.9-6.4 mg cm^{-2}, 2.25-4.4 mg cm^{-2}, and 1.2 mg cm^{-2} respectively. $LiCoO_2$ (LCO, LG Chem.) electrodes were fabricated by mixing the LCO and super-P with a polyvinylidene fluoride (PVDF) binder at a weight ratio of 85:7.5:7.5 in N-methyl-2-pyrrolidone (NMP) solution. The LCO slurry was coated onto an Al current collector with average loading level of 25-26 mg cm^{-2}. The electrolyte was comprised of 1.3M $LiPF_6$ in ethylene carbonate/diethyl carbonate (3/7, v/v) with 10 wt% fluorinated ethylene carbonate additives to improve the cycling stability. Polyprolylene film (Celgard 2400) was used as a separator. These were carefully assembled in an argon-filled glove box. After cycling, each cell was opened in the glove box and washed with dimethyl carbonate to remove residual electrolyte and any other impurities. Then it was dried at room temperature. Galvanostatic discharge/charge test results were made by a WBCS3000K8 (WonATech Co., Ltd.). EIS measurements were carried out between 10 000–0.1 Hz with an amplitude of 10 mV at a fully-delithiated state (~1.5 V).

3.3 Results and discussion

Typically, an aqueous suspension of natural polysaccharides (agarose) is starting material for agarose-derived hard carbon (AHC) based materials. The homogeneous agarose solution was mixed with a nitrogen-containing polymer, MF, originally dissolved in n-butanol. Dilution of MF with DMF was necessary to increase the compatibility of both solutions. Thereafter, the prepared GeO_2 sol was added to the above solution at 110 ℃ under vigorous stirring until it became clear. The mixture was poured into a cold bath to promote gelation and completely dried.[38-40] The gelated GeO_2/C sample cut into a cube shape, and then pre-heated to 250 ℃ in air to soften the samples. Afterwards, it was further annealed at 500 ℃ for 1 h and 900 ℃ for 2 h in argon at which powder-type Ge/C sample was obtained by the carbothermal reduction process. Then, its size was reduced by a ball-milling process. Without annealing at 900 ℃ for 2 h heating step, partially carbonized ANHC/GeO_2 cube was obtained. In addition, AHC and ANHC can be easily prepared excluding MF and GeO_2. Furthermore, pure Ge was obtained through the heat treatment of ANHC/Ge at 450 ℃ for 5 h in air.

The AHC samples showed high purity and plate-like morphology by scanning electron microscopy (SEM) and energy-dispersive X-ray spectroscopy (EDX) analysis (Fig. S1†). After ball-milling, hard carbon of hundreds-of-micrometer was evenly decomposed into particles of less than 2 μm and showed non-porous features in nitrogen adsorption isotherms and Barret-Joyner-Halenda (BJH) pore size distribution curve. Likewise, a similar structure of ANHC was shown, except that MF effectively bound to the agarose matrix due to nitrogen dopoing. The residual MF, which was not involved in nitrogen-doping, was thermally decomposed. This resulted in the creation of void spaces as shown in Brunauer-Emmett-Teller (BET) surface and pore volume (Fig. S2†). Further, it is clarified how nitrogen atoms are arranged in the hard carbon matrix by transmission electron microscopy (TEM) image and X-ray photoelectron spectroscopy (XPS) analysis (Fig. S3†). Owing to the simple synthesis process and sufficient surface functionalities of the polysaccharides, the nitrogen doping level could simply be adjusted from 1 to 10 % depending on the amount of MF (Fig. S4†).[42, 43]

Fig. 3-1a shows schematic illustration of a simplified procedure for converting ANHC/GeO2 to ANHC/Ge. The ionized GeO_2 sol (GeO_3^{2-}) was repositioned in the form of a monolith wrapped in ANHC with a size of 0.5-1.5 μm during heat treatment. TEM image and scanning-transmission electron microscopy (STEM) – high annular dark-filed (HAADF) image clearly showed relatively heavy GeO_2 body completely covered with lightweight nitrogen-doped hard carbon peels (Fig. S5†). Because of the amorphous nature of GeO_2 at this stage, no specific crystal plane was

observed. As the temperature rises above 800 ℃, the outer carbon shell begins to participate in carbothermal reduction and the inner GeO_2 monolith self-assembles into a homogeneous dispersion of Ge nanoparticles (less than 25 nm in diameter) in the ANHC shell. This continuous transition from ANHC to ANHC/Ge was elucidated by Raman spectroscopy (Fig. 3-1b) and X-ray diffraction (XRD) measurements (Fig. S6†). Both results showed that the ANHC sample has the typical properties of a non-graphitic carbon material with a D/G ratio of 1.73. The loaded GeO_2 particles had characteristic peaks of amorphous property ranging from 300 cm^{-1} to 900 cm^{-1}.[44] However, with the help of further heat treatment, ANHC reduced GeO_2 into Ge by carbothermic process and partially graphitized as displayed in D/G ratio of 1.48. The reduced Ge showed a diamond cubic phase (JCPDS card no. 40-0545) in the XRD and a crystalline Ge peak at 301 cm^{-1} in the Raman spectrum.

Despite the significant loss of oxygen from GeO_2 and possibly evolved CO_2, the synthesized ANHC/Ge showed a similar particle size distribution, but rather presented a completely different morphology (Fig. 3-1c and 3-1d). From the TEM-EDX mapping results, small black particles were identified as Ge and each Ge nanoparticle represented by a white arrow was fully encapsulated within the ANHC shell (Fig. 3-1e and 3-1f). Another TEM image showed a polycrystalline nature of Ge with a crystallite size which is in good agreement with those calculated from XRD.[45] From the observed lattice fringes and corresponding selected area diffraction (SAED) pattern, the distance of (111) plane was estimated as 0.325 nm and the (220) plane was 0.28 nm (Fig. 3-1g). The STEM image further demonstrated the evolution of encapsulated structure with uniform size of Ge nanoparticles and dispersion throughout the sample (Fig. 3-1h and 3-1i).

Although the overall particle size did not change much, many voids remained inside the ANHC shell by reducing GeO_2. The compact wrap structure of ANHC/GeO_2 has a type-II nitrogen sorption isotherm corresponding to the non-porous morphology. However, after carbothermic reduction, specific surface area significantly increased from 19.9 $m^2 g^{-1}$ to 272.4 $m^2 g^{-1}$ (Fig. S7a†). This resulted from the generation of gaseous carbon dioxide and/or carbon monoxide species and reduction of GeO_2 to Ge. In terms of pore volume there was no significant difference before and after reduction. However, in the BJH pore size distribution curve derived from mesoporous properties of ANHC shell, one prominent peak appeared at about 5 nm. In addition to morphological changes during the self-assembly process, quantitative variations were also monitored by low magnification EDX mapping and thermo-gravimetric analysis (TGA). As shown in the EDX elemental spectrum, the amount of oxygen (relative to Ge) in the ANHC/Ge sample was significantly reduced without changing the remainder compared to the ANHC/GeO_2

sample (Fig. S8a-d†). As a further comparison, pure Ge samples obtained from calcination of the ANHC/Ge were analyzed through SEM, corresponding EDX mapping, and XRD (Fig. S9a-c†). Moreover, ANHC amounts in both samples were estimated using TGA in air atmosphere. It is suggested that approximately 38 wt% and 52 wt% of ANHC are involved in the ANHC/GeO_2 and ANHC/Ge samples, respectively (Fig. S8e-f†). Since on-set temperature for Ge oxidation is known as the above 800°C, TGA analysis was performed at below 800°C.[46]

Various chemical bonding properties were characterized by XPS analysis as shown in Fig. 3-2. In the core spectrum of Ge 3d level, there are four major deconvolution peaks, each consisting of Ge-Ge (29.8eV), Ge-O (31.5eV/32.7eV) and Ge-C (30.5eV).[47] The dominant Ge-O peak originates from the rearranged GeO_2 monolith, and the interfacial carbon atoms can be easily bonded to the Ge over the whole particle by thermal annealing (Fig. 3-2a). However, the peak associated with Ge-O was completely reduced and the pure metallic Ge-Ge peak appeared along with small shoulder peak of Ge-C (Fig. 3-2b). This chemical bond between Ge and C enhances structural integrity and cycle stability in later electrochemical tests. The high-resolution XPS spectrum of C 1s contains several peaks and shows an increase in C-N peak (285.6eV) after reduction at high temperature (Fig. 3-2c-d). In general, doped elements tend to penetrate the carbon network and have strong covalent bonds. In addition, it has been revealed that heat treatment at high temperature accompanying the reduction process preferentially produces pyrrolic nitrogen sites that can further improve the conductivity of the material (Fig. 3-2e-f).

In order to verity the lithium storage characteristics of AHC-based materials, we first tested in a coin-type half cell with a lithium metal counter and a reference electrode with a voltage range of 0.01-3.0V (Fig. S10†). The first discharge/charge curves of the three electrodes showed different voltage plateaus, the amount of Li-ion uptake and the corresponding Coulombic efficiency. Unlike conventional graphite anodes, the initial reversible capacity was as high as 450 mAh g^{-1} and 572 mAh g^{-1} for AHC and ANHC-10 electrodes, respectively. This result demonstrates that there are some different storage behaviors for hard carbon materials with nitrogen doping (Fig. S10a†).[48-52] Typically, various dopants in the non-graphitized carbon domains provide highly active sites for Li-ions to deliver an unusually high capacity over that of some alloy-type anodes provide.[51, 52]

Among various dopants, nitrogen is attractive for carbon anodes due to its relatively higher electronegativity and smaller atom size. Penetration of nitrogen atom in carbon networks can generate nanopores which may contribute to provide extra capacity. Furthermore, nitrogen enhances the interaction between active materials and Li ions, resulting in easy Li insertion.[51] Despite the initial capacity loss in the first formation cycle, the ANHC-10 electrodes showed a

stable capacity retention over several thousand cycles even at high mass loading of 6.4 mg cm^{-2} (>2.2 mAh cm^{-2}). This result is attributed to increased electrical conductivity of highly doped samples, narrow size distribution after milling, plate-like structure suitable for high density packing, and low surface area. Carbon-based anodes usually have a low tap density and high mass loading can hardly be achieved by conventional methods.[53]

The effect of doping concentration on electrochemical performance was also investigated. As expected, the initial coulombic efficiencies and the cycle retention for 100 cycles did not show a significant difference, while the slightly improved rate capability was shown in Fig. S11.† From the state of the precursor, the doping agent can form a chemical bonding with the agarose matrix, allowing the mixture to be homogeneously dispersed, which leads to a relatively high doping limit of >10%. After pressing the electrodes with different loading levels, their volumetric capacity was estimated by diving the areal capacities by measuring the electrode thickness. As summarized in Fig. S12, all the electrodes showed highly suppressed swelling results of less than 40%. Interestingly, its volumetric capacity could be adjusted to ~571 mAh cm^{-3} with a packing density of 1.88 g/cc after 100 cycles, which is comparable to the high volumetric capacity of the recently reported carbon-based anode materials.[53] Some works did not take the swelling of the electrode or the change in porosity into account after prolonged cycles, when calculating volumetric capacities. This leads to a slight overestimation value, but the electrodes always expand by more than 30%. With this in mind, some specifications of the ANHC electrodes are beyond traditional graphite-based anodes, suggesting a potential feasibility in practical battery applications.

Fig. 3-3 shows a series of electrochemical performances using the ANHC/Ge anode in a half cell test. At a rate of C/20, the ANHC/Ge anode delivered a discharge capacity of 1322 mAh g^{-1} with an initial coulombic efficiency of 60.5%, which resulted from a SEI formation and a large amount of ANHC in the composite (Fig. 3-3a). As the next generation anode standard requires reversible capacity of 800-1200 mAh g^{-1}, we did not intend to increase Ge composition.[54] Another reason to limit the Ge amounts in the Ge/C composite is due to the huge volume expansion of Ge anode which results in poor cyclability (Fig. S13†). The shape of the voltage profiles did not change after 500 cycles. This indicates that the robust structural integrity of the ANHC/Ge material is adequately preserved. In the differential capacity (dQ/dV) curve transformed from the voltage profile, the phase transition of the crystalline Ge to amorphous Ge through various stages inside the ANHC shell is observed in the formation of SEI layer in the first cathodic curve (Fig. 3-3b).[55, 56] From subsequent cycles, both cathodic and anodic peaks did not change. In the anodic curve, two peaks of 0.45 and 0.65V are merged into a single peak of 0.55V and assigned to the dealloying process of Li_xGe. In addition, there were no significant peaks associated with common

hard carbon materials in this broad range.

The cyclability of the ANHC/Ge anode was investigated at different current densities of C/2 to 1C for both discharging and charging (Fig. 3-3c). Although small IR drops occurred in the early stage of cycling, their capacity retention after 500 cycles showed 88.5%, 94.0%, and 95.6% with average coulombic efficiency of 99.64, 99.68, and 99.71%, respectively.

As mentioned above, Ge-based anodes are suitable for high-power cells (fast charging or fast delithiation in a half cell configuration and fast discharging in full cell configuration) due to their high conductive nature. Such asymmetric operation focuses on improvement of charging capacity at fixed discharge rate in past research because large companies are about to concentrate on rapid charging (lithiation of anode at full cell), which is a system for future applications such as electric vehicles. So, unlike other studies, we have set up this type of test condition. Interestingly, the ANHC/Ge electrode can effectively withstand the fast penetration of Li-ions, meaning that structural integrity can be maintained without crushing or detaching from the current collector. When the C-rate was increased to 5C, the ANHC/Ge electrode showed a reversible charge capacity of 420 mAh g^{-1} which is still higher than that of graphite anodes (Fig. 3-3d). After the rate capability test, their initial capacities were fully recovered.

From the viewpoint of the volume of the ANHC/Ge electrode, changes in electrode thickness were monitored to accurately convert the areal capacity to the volumetric one (Fig. 3-4). Without the pressing step, the ANHC/Ge electrode with a loading level of 2.25 mg cm^{-2} (1.79 mAh cm^{-2}) has a thickness of 17 μm without further calendering, which delivers a volumetric capacity of 1052.9 mAh cm^{-3} at only consideration of anode side as a conventional calculation method (Fig. 3-4e). Remarkably, the electrode swelling showed 11.8% after 100 cycles and 17.6% after 500 cycles, which corresponds to the reversible volumetric capacities of 784.6 mAh cm^{-3} and 713 mAh cm^{-3}, respectively. These values reflect the volume expansion of the electrodes possible from the practical viewpoint of batteries (Fig. 3-4a-d). This result is very impressive as most of the electrodes containing alloy-type anodes (e.g., Si, Ge, and Sn) exhibit a serious swelling problem of >50% even after several cycles.[57-61] Therefore, their high theoretical volumetric capacity dramatically decreases below half of the capacity initially supplied. Conversely, the unique architecture of ANHC/Ge materials mitigated the volume expansion and, as a result, retained a volumetric capacity of about 70%, despite the loading levels being much higher than the other Ge anodes.[31, 32] Thereafter, the loading level is up to 4.36 mg cm^{-2} (~3 mAh cm^{-2} and ~1570 mAh cm^{-3}) for the fabrication of high energy full cells, which meets current standard for portable electronics.[54] Such a high-mass loaded electrodes showed a stable cycle life over 100 cycles in a half cell with a negligible amounts of decay (Fig. 3-4f-g).

Electrochemical impedance spectroscopy (EIS) analysis was performed between 10 kHz and 0.1 Hz to investigate the interfacial charge transfer phenomena of different electrodes after 1st and 100th cycles, respectively (Fig. 3-3e and 3-3f). At high frequencies (> 10 kHz), the spectrum is usually dominated by the ionic conductivity of the electrolyte, which does not have a big variation in three electrodes used the same electrolytes, unless extremely high frequencies are applied.[62] In the lower frequency range, each active material involved in the redox reaction acts as a surface resistance of the electrode in the form of electron transfer resistance at the electrode interface with the electrolyte and the passivating SEI layers, which corresponds to a diameter of semicircles in the Nyquist plots. With the nitrogen doping, surface or charge transfer resistance of ANHC electrode decreased from 3970 Ω (without doping) to 221 Ω, while ANHC/Ge electrode showed 301 Ω after 1st cycle. After 100 cycles, however, the charge transfer resistance remarkably decreased (Fig. 3-3f). In the case of the ANHC electrode, traces of the second semicircle having a diameter of 63 Ω appear after 100 cycles, possibly due to the accumulated SEI layer on the surface. It is assumed that the SEI layer accumulates on the ANHC material. Similarly, the ANHC/Ge electrode has also a second semicircle trace with a small diameter of less than 20 Ω in the lower frequency range. When the encapsulated Ge particles are escape from the ANHC shell, it causes irregular formation of the SEI network and no similar trend of interfacial resistance is shown. On the other hand, the AHC electrode still shows a large impedance across the interface, suggesting that poor intrinsic conductivity of AHC cannot promote Li-ion transport at the outermost surface.

In order to investigate effective encapsulation of the Ge nanoparticles in the ANHC shell, the tested cells were disassembled in an argon-filled glove box and the electrodes were gently washed with dimethyl carbonate. Then, it was further scratched out to characterize the morphology of single particles through TEM measurement (Fig. 3-5). As schematically shown in Fig. 3-5a, the ANHC/Ge is expected to undergo morphological changes as described below. At the beginning of the cycle, the encapsulated Ge nanoparticles expand considerably to fill the empty space which can sufficiently accommodate a large volume change. Then, each particle experiences repeated expansion/contraction. Eventually some are broken down into smaller pieces (indicated as blue area in Fig. 3-5g), while others are rather coalesced, compared to the pristine state (Fig. 3-5f and 3-5g). Nonetheless, ANHC/Ge preserves an initial morphology by encapsulating Ge nanoparticles inside the carbon shells, which is attributed to flexible carbon layers of ANHC acting as a buffer layer during the large volume change and preventing direct contact of electrolytes to the inside Ge.[63] In addition, the ANHC shell also participates in the redox reaction with Li-ions and increases the energy of cell by minimizing the dead weight of the active substance. The TEM and HAADF-STEM images support the above explanation (Fig. 3-5b-d). Unlike TEM images of pristine state

with abundant vacant space (Fig. 3-1), the internal space was tightly packed with the disintegrated and coalesced Ge particles.

From the elemental mapping results of TEM-EDX, it was also shown that the Ge particles are adequately encapsulated by the conductive ANHC layers and several SEI components uniformly covering ANHC/Ge particle surfaces. Among various components of SEI layers formed on active materials, it is assumed to have predominantly lithium fluoride (LiF) and lithium carbonate derivatives.[64] From the TEM image of high magnification (Fig. S14†), the structure of each layer of ANHC/Ge after cycling was observed, in which the SEI layer of ~3 nm was coated on the surface of ANHC/Ge particle with dense and non-porous features. In order to demonstrate the practical viability of the ANHC/Ge anode, a coin-type full cell was made by matching up with a high mass LCO cathode. To achieve a high volumetric energy density, all the electrodes for the full cell are pressed up to reach a high electrode packing density before assembly having a wide voltage range of 3.0-4.3V.

Fig. 3-6a shows electrode thickness variations of their assembled form including current collectors before and after 300 cycles. The as-cycled electrodes showed 21% and 33% electrode expansion for the anode and the cathode, respectively, but the total thickness of the full cell increased to 25%. For a given electrode area, it is assumed that the volume of full cell increases by 25%, which is the same amount as the decrease in volumetric capacities (or energy). One thing to address here is that the anode made of ANHC/Ge materials has a much lower expansion after several hundred cycles than the cathode. Surprisingly, the initially designed cell capacity of ~3 mAh cm^{-2} (288.4 mAh cm^{-3}) has a capacity retention of 61% after 300 cycles (~2.2 mAh cm^{-2} and 176.15 mAh cm^{-3}) reflecting the overall volume change of the full cell, while the areal capacity shows a 73% retention (Fig. 3-6b). Since there is no comparative study on Ge-based anodes that has been demonstrated in full cells for such a long cycle and a lack of information for calculation of volumetric capacities, the above performance is solely compared with several outstanding Ge-based anodes in half cell and several alloy-type anodes by recalculating those in terms of half cell data (Table S1†). During the prolonged cycles, there is no significant changes in their charge/discharge profiles even with higher current densities (Fig. S15†).[65] The sloping feature in their profiles is due to a large amount of hard carbon and amorphized Ge. This prototype LIB composed of ANHC/Ge and LCO cathode can successfully light up red light-emitting diodes (LEDs) lasting about 1 h (Fig. S16†). This result means that the LIB using the ANHC/Ge anode provides sufficiently high volumetric energy to be used for a long time in order to demonstrate feasibility in practical LIB.

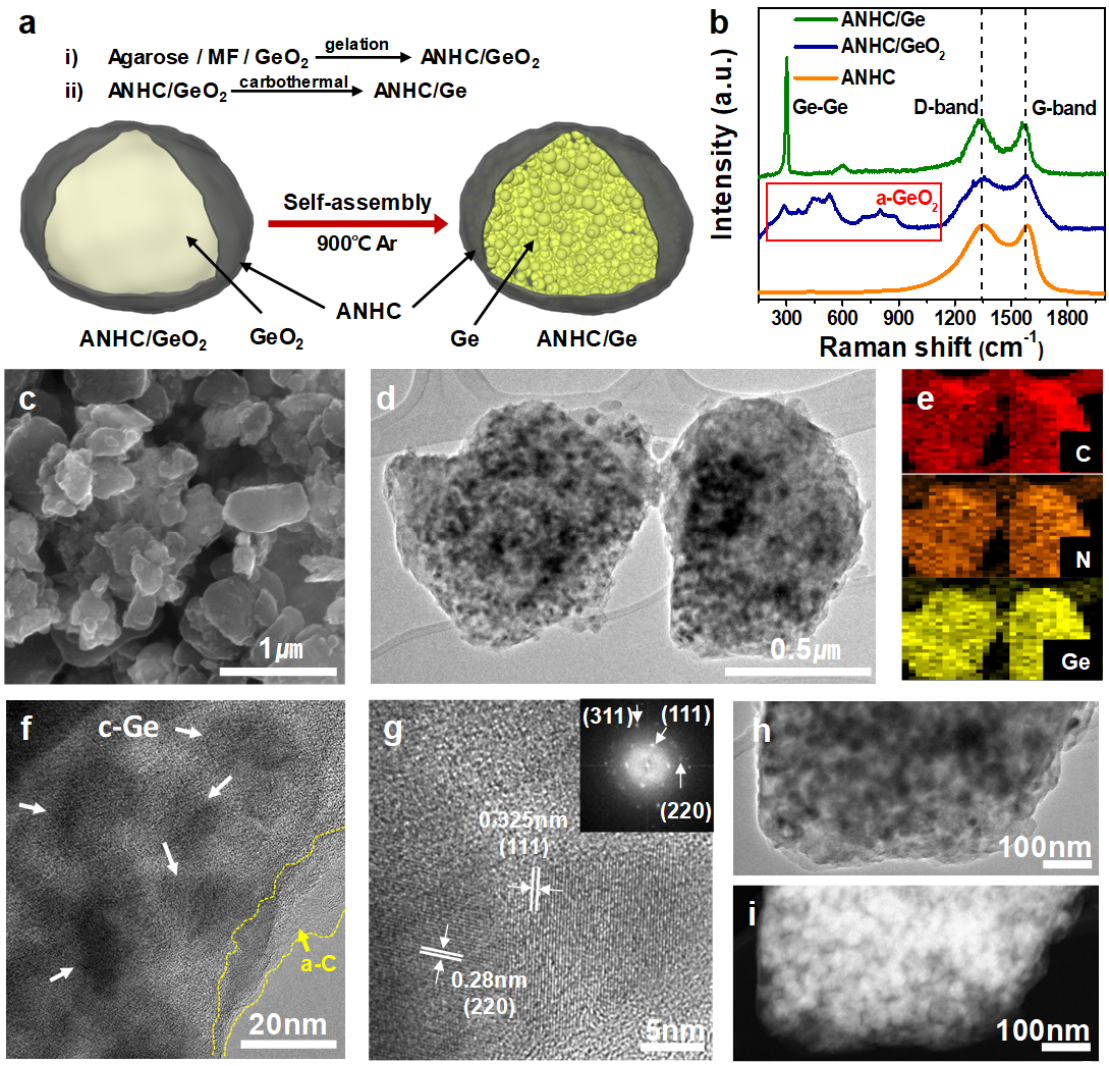

Figure 3-1. (a) Schematic illustration of self-assembly process and morphological changes of ANHC/Ge. (b) Raman spectra of ANHC (bottom), ANHC/GeO_2 (middle), and ANHC/Ge (top). (c) SEM image, (d,f-h) TEM images, (e) TEM-EDX mapping results, and (i) STEM-HAADF image of ANHC/Ge. Inset is SAED pattern showing a formation of polycrystalline Ge.

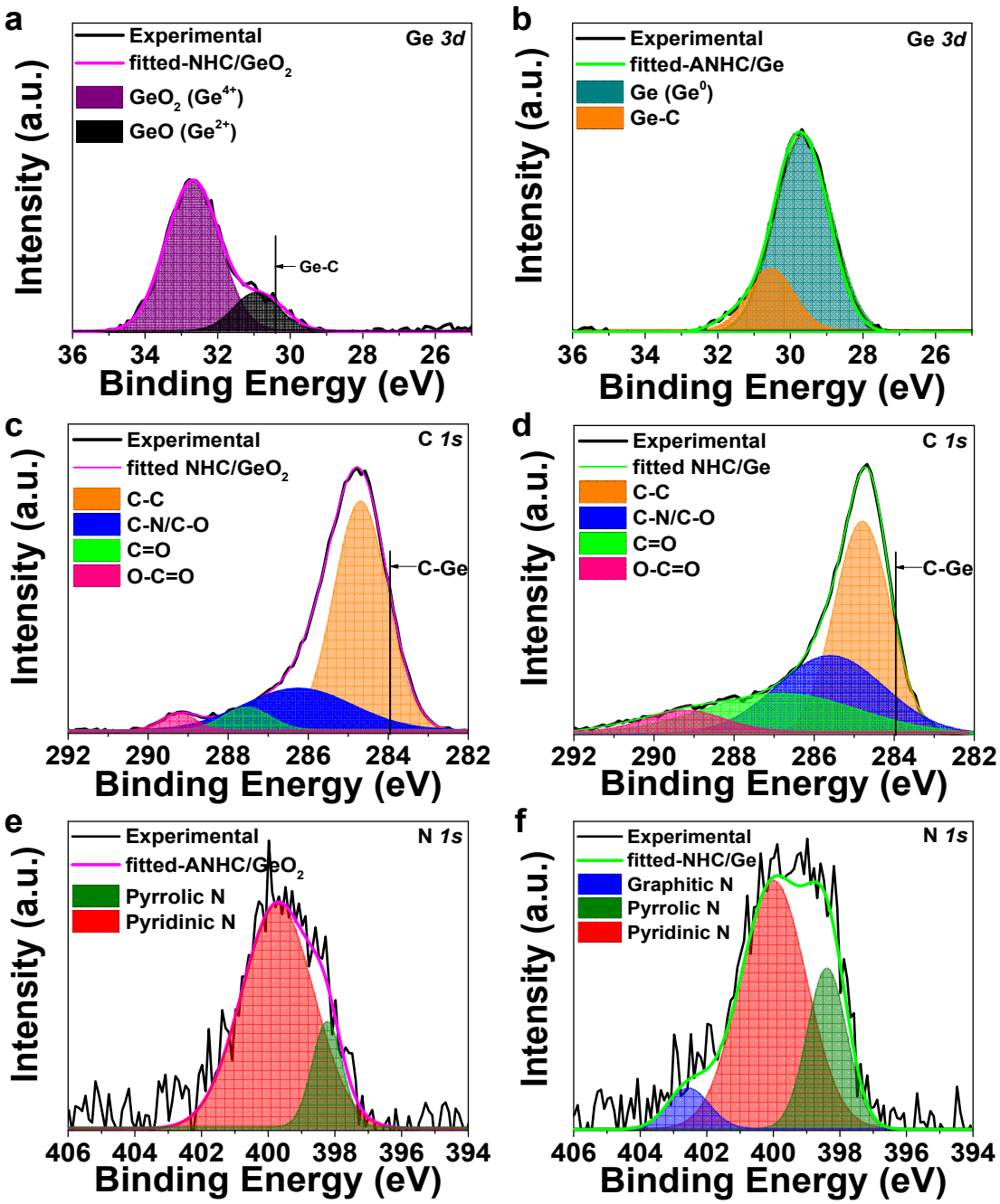

Figure 3-2. XPS analysis of ANHC/GeO_2 and ANHC/Ge. Core-level XPS spectra of (a, c, e) ANHC/GeO_2 and (b, d, f) ANHC/Ge for Ge 3d, C 1s, and N 1s, respectively.

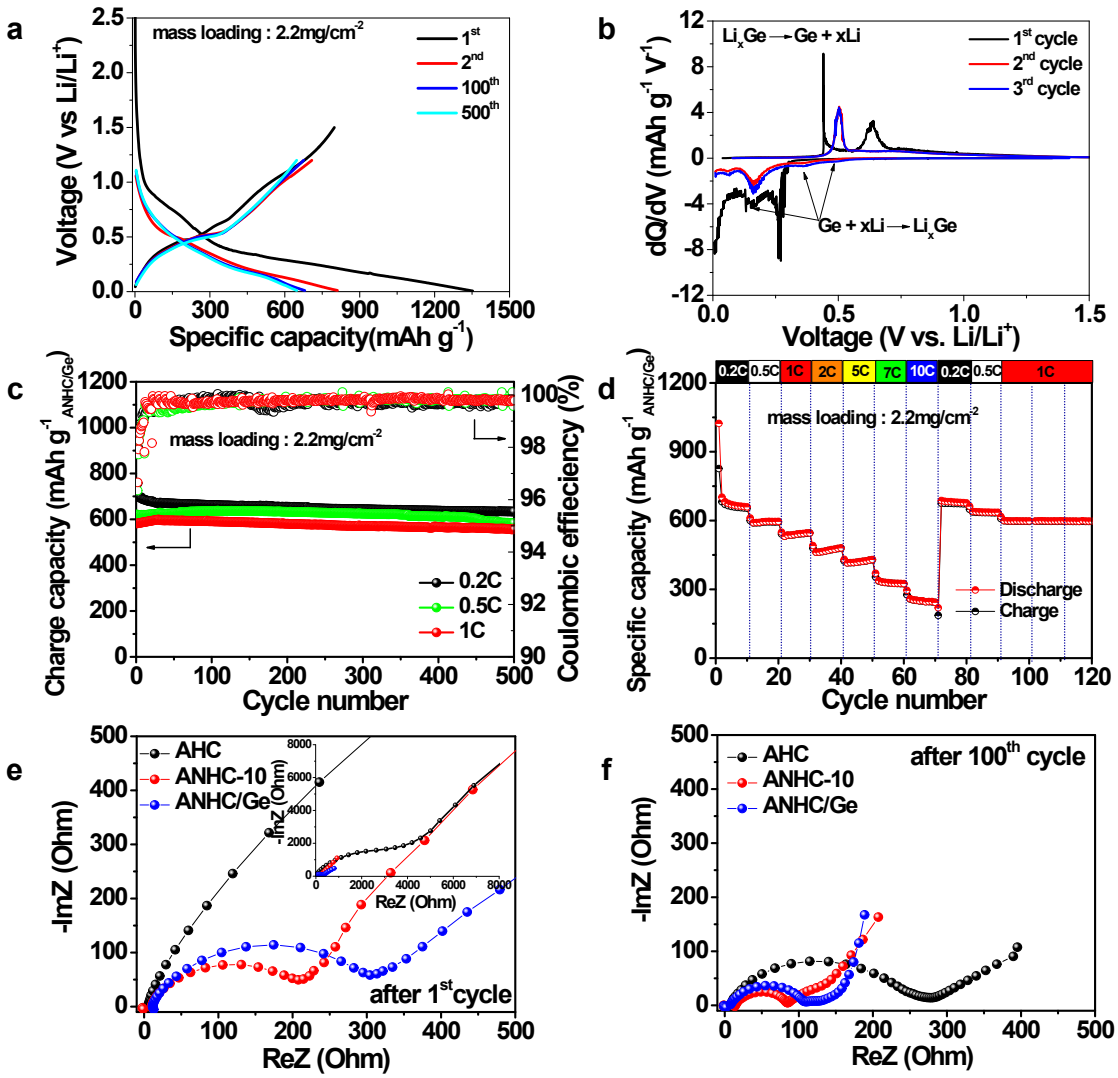

Figure 3-3. Electrochemical performances of ANHC/Ge electrodes. (a) Galvanostatic discharge/charge profiles of ANHC/Ge electrode for 1st, 2nd, 100th, and 500th cycles. (b) dQ/dV plots of ANHC/Ge for initial three cycles. (c) Long-term cycle life of ANHC/Ge electrode at different C-rates. (d) Rate capabilities of ANHC/Ge at various C-rates. (e-f) Electrochemical impedance spectroscopy (EIS) plots for AHC (black), ANHC-10 (red), and ANHC/Ge (blue) after 1th and 100th cycles.

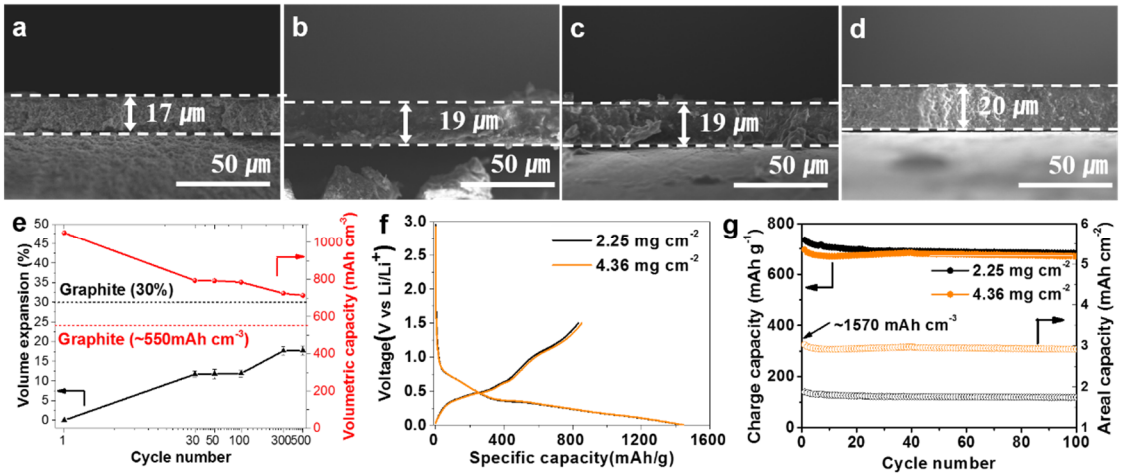

Figure 3-4. Electrode swelling results: cross-sectional SEM images of ANHC/Ge electrodes (a) at pristine state, after (b) 1st cycle, (c) 100th cycle, and (d) 500th cycle. (e) Equivalent plots for electrode swelling results (left ordinate) and corresponding volumetric capacities (right ordinate). Electrochemical results of high mass ANHC/Ge electrode: (f) first galvanostatic discharge/charge curves and (g) cycling stability for 100 cycles at a rate of C/5 along with previous electrode of moderate loading level.

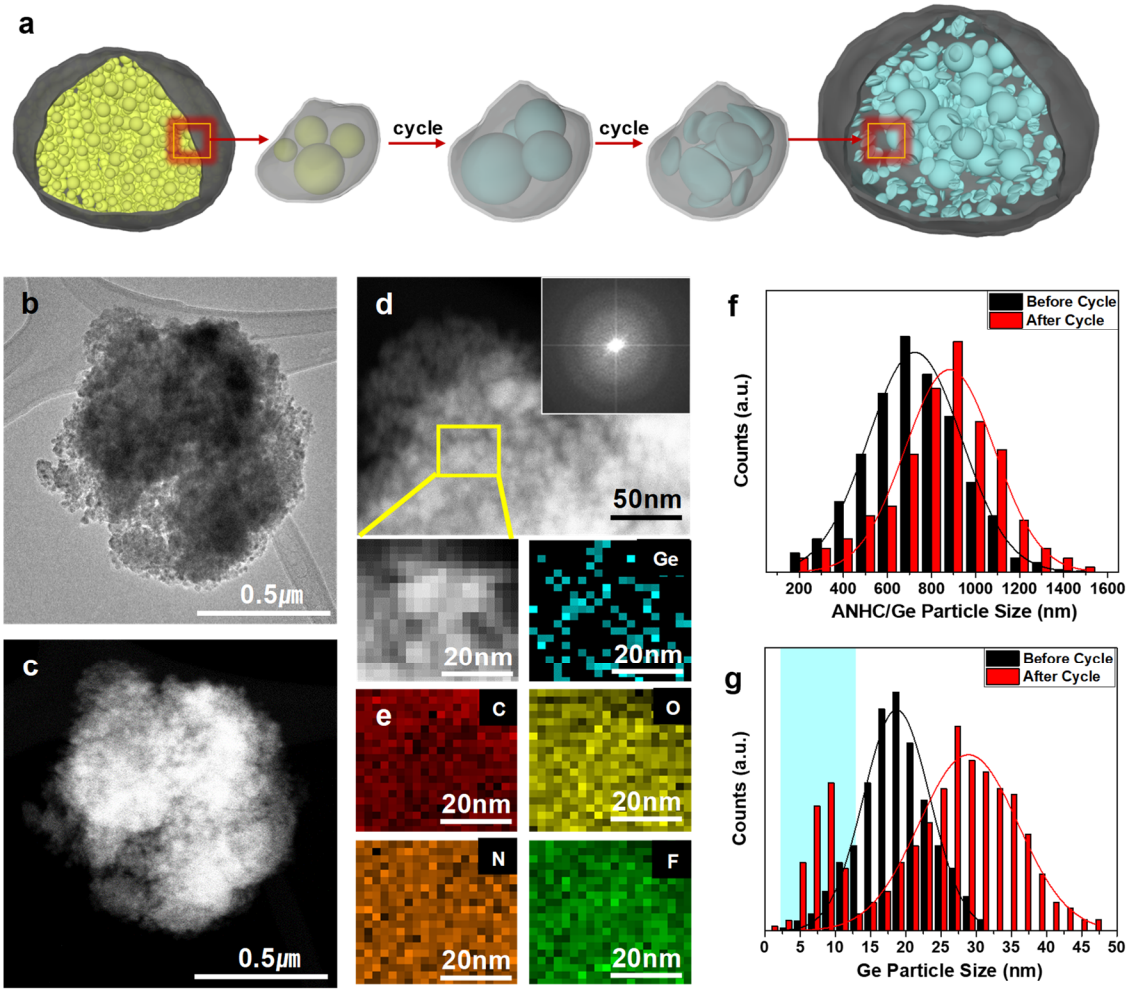

Figure 3-5. Post characterization of ANHC/Ge electrode. (a) Schematic illustration showing structural changes of ANHC/Ge. (b) TEM image, (c, d) STEM-HAADF images, and (e) TEM-EDX mapping results for ANHC/Ge after 100 cycles at 1C rate. The inset is the corresponding SAED pattern showing amorphous nature of Ge particles after cycles. (f, g) Size distribution curves for ANHC/Ge particle and Ge particle before/after 100 cycles at 1C rate.

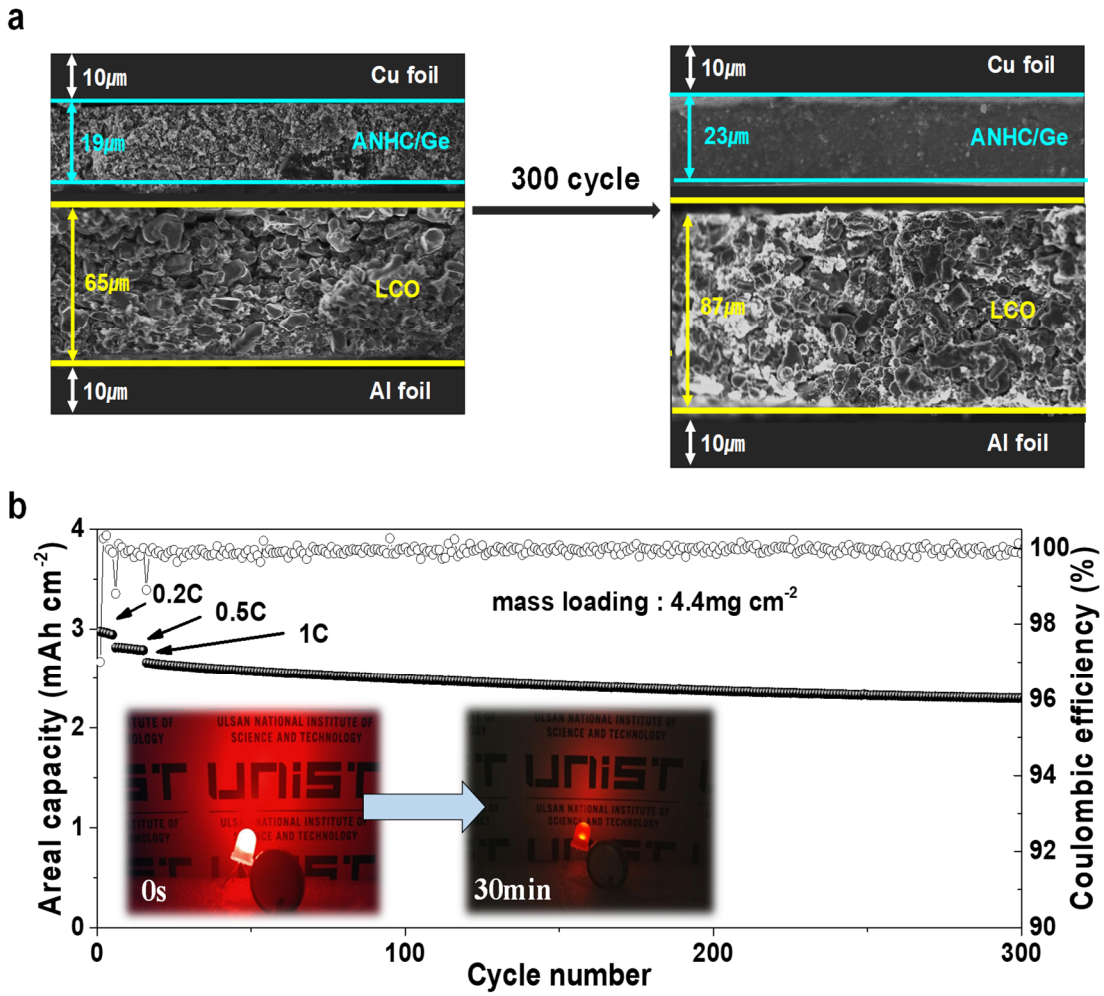

Figure 3-6. Full cell performance of ANHC/Ge anodes. (a) Cross-sectional SEM images of both anode and cathode before/after 300 cycles. (b) Long-term cycle life of full cell at 1C rate (Inset: red LED bulb lit up by as-assembled full cell).

3.4 Conclusions

Hybridization strategies have been developed to enhance the electrochemical performance of Ge anode incorporating with highly conductive carbon buffer layers derived from natural sources. Unlike conventional bottom-up approaches using different kinds of expensive precursors, dissolution of commercially available GeO_2 in an agarose matrix produces a homogeneous dispersion of composite material in nanoscale. After that, carbothermic reduction under an inert atmosphere promoted self-organization of Ge nanoparticles in nitrogen-doped carbon buffer. With this strategy, the nitrogen doping level was easily adjusted to 10%, which can increase the electrical conductivity of ANHC. Effective coupling of Ge anode and ANHC has been demonstrated in half cell and full cell. This novel structure stabilized the Ge anode at the early stage of cycling through a highly conductive and robust nature of ANHC. In addition, the electrode was tightly packed to achieve a high volumetric capacity with an improved cycling stability over hundreds of cycles. When we even took a swelling of ANHC/Ge electrode into account, it still outperformed conventional graphite anodes and typical Ge/C composite anodes in their volumetric capacities. A full cell consisting of an ANHC/Ge anode and an LCO cathode have been successfully constructed to demonstrate long-term stability with ultra-high volumetric capacity, indicating the practical viability in LIBs. This simple methodology can be further applicable to hybridizing protocol with metal oxides soluble in certain solvents with polysaccharides, and open up a potential feasibility in a wide range of applications.

3.5 Reference

1. Park, C. M.; Kim, J. H.; Kim, H.; Sohn, H. J. Li-alloy based anode materials for Li secondary batteries. *Chem. Soc. Rev.* **2010,** *39*, 3115-3141.
2. Ji, L.; Lin, Z.; Alcoutlabi, M.; Zhang, X. Recent developments in nanostructured anode materials for rechargeable lithium-ion batteries. *Energy Environ. Sci.* **2011,** *4*, 2682-2699.
3. Bruce, P. G.; Scrosati, B.; Tarascon, J. M. Nanomaterials for rechargeable lithium batteries. *Angew. Chem. Int. Ed.* **2008,** *47*, 2930-2946.
4. Song, T.; Cheng, H.; Town, K.; Park, H.; Black, R. W.; Lee, S.; Park, W. I.; Huang, Y.; Rogers, J. A.; Nazar, L. F.; Paik, U. Electrochemical properties of si-ge heterostructures as an anode material for lithium ion batteries. *Adv. Funct. Mater.* **2014,** *24*, 1458-1464.
5. Chan, C. K.; Zhang, X. F.; Cui, Y. High capacity li ion battery anodes using ge nanowire. *Nano Lett.* **2008,** *8*, 307-309.
6. Song, T.; Cheng, H.; Choi, H.; Lee, J. H.; Han, H.; Lee, D. H.; Yoo, D. S.; Kwon, M. S.; Choi, J. M.; Doo, S. G.; Chang, H.; Xiao, J.; Huang, Y.; Park, W. I.; Chung, Y. C.; Kim, H.; Rogers, J. A.; Paik, U. Si/Ge double-layered nanotube array as a lithium ion battery anode. *ACS Nano* **2012,** *6*, 303-309.
7. Liu, Y.; Zhang, S.; Zhu, T. Germanium-based electrode materials for lithium-ion batteries. *Chemelectrochem* **2014,** *1*, 706-713.
8. Graetz, J.; Ahn, C. C.; Yazami, R.; Fultz, B. Nanocrystalline and thin film germanium electrodes with high lithium capacity and high rate capabilities. *J. Electrochem. Soc.* **2004,** *151*, A698-A702.
9. Klavetter, K. C.; Wood, S. M.; Lin, Y. M.; Snider, J. L.; Davy, N. C.; Chockla, A. M.; Romanovicz, D. K.; Korgel, B. A.; Lee, J. W.; Heller, A.; Mullins, C. B. A high-rate germanium-particle slurry cast li-ion anode with high coulombic efficiency and long cycle life. *J. Power Sources* **2013,** *238*, 123-136.
10. Yuan, F. W.; Yang, H. J.; Tuan, H. Y. Alkanethiol-passivated ge nanowires as high-performance anode materials for lithium-ion batteries: the role of chemical surface functionalization. *ACS Nano* **2012,** *6*, 9932-9942.
11. Morin, F.J.; Maita, J. P. Electrical properties of silicon containing arsenic and boron. *Phys. Rev.* **1954,** *96*, 21-24.
12. Seng, K. H.; Park, M. H.; Guo, Z. P.; Liu, H. K.; Cho, J. Self-assembled germanium/carbon nanostructures as high-power anode material for the lithium-ion battery. *Angew. Chem. Int. Ed.* **2012,** *51*, 5657-5661.

13. Ngo, D. T.; Le, H. T. T.; Kim, C.; Lee, J. Y.; Fisher, J. G.; Kim, I. D.; Park, C. J. Mass-scalable synthesis of 3d porous germanium-carbon composite particles as an ultra-high rate anode for lithium ion batteries. *Energy Environ. Sci.* **2015,** *8*, 3577-3588.
14. Tan, L. P.; Lu, Z.; Tan, H. T.; Zhu, J.; Rui, X.; Yan, Q.; Hng, H. H. Germanium nanowires-based carbon composite as anodes for lithium-ion batteries. *J. Power Sources* **2012,** *206*, 253-258.
15. Li, X.; Yang, Z.; Fu, Y.; Qiao, L.; Li, D.; Yue, H.; He, D. Germanium anode with excellent lithium storage performance in a germanium/lithium-cobalt oxide lithium-ion battery. ACS Nano **2015,** *9*, 1858-1867.
16. Wu, X. L.; Guo, Y. G.; Wan, L. J. Rational design of anode materials based on group iva elements (si, ge, and sn) for lithium-ion batteries. *Chem. Asian J.* **2013,** *8*, 1948-1958.
17. Yan, C.; Xi, W.; Si, W.; Deng, J.; Schmidt, O. G. Highly conductive and strain-released hybrid multilayer ge/ti nanomembranes with enhanced lithium-ion-storage capability. *Adv. Mater.* **2013,** *25*, 539-544.
18. Bogart, T. D.; Chockia, A. M., Korgel, B. A. High capacity lithium ion battery anodes of silicon and germanium. *Curr. Opin. Chem. Eng.* **2013,** *2*, 286-293.
19. Li, W.; Li, M.; Yang, Z.; Xu, J.; Zhong, X.; Wang, J.; Zeng, L.; Liu, X.; Jiang, Y.; Wei, X.; Gu, L.; Yu, Y. Carbon-coated germanium nanowires on carbon nanofibers as self-supported electrodes for flexible lithium-ion batteries. *Small* **2015,** *11*, 2762-2767.
20. Kennedy, T.; Mullane, E.; Geaney, H.; Osiak, M.; O'dwyer, C.; Ryan, K. M. High-performance germanium nanowire-based lithium-ion battery anodes extending over 1000 cycles through in situ formation of a continuous porous network. *Nano lett.* **2014,** *14*, 716-723.
21. Choi, S.; Kim, J.; Hwang, D. Y.; Park, H.; Ryu, J.; Kwak, S. K.; Park, S. Generalized redox-responsive assembly of carbon-sheathed metallic and semiconducting nanowire heterostructures. *Nano Lett.* **2016,** *16*, 1179-1185.
22. Liu, J.; Song, K.; Zhu, C.; Chen, C. C.; Aken, P. A. van; Maier, J.; Yu, Y. Ge/c nanowires as high-capacity and long-life anode materials for li-ion batteries. *ACS Nano* **2014,** *8*, 7051-7059.
23. Park, M. H.; Cho, Y.; Kim, K.; Kim, J.; Liu, M.; Cho, J. Germanium nanotubes prepared by using the kirkendall effect as anodes for high-rate lithium batteries. *Angew. Chem. Int. Ed.* **2011,** *50*, 9647-9650.
24. Yang, L. C.; Gao, Q. S.; Li, L.; Tang, Y.; Wu, Y. P. Mesoporous germanium as anode material of high capacity and good cycling prepared by a mechanochemical reaction. *Electrochem.*

Commun. **2010,** *12*, 418-421.

25. Cheng, J.; Wang, J.; Li, W.; Liu, X.; Yu, Y. Highly reversible lithium storage in a 3d macroporous ge@c composite. *RSC Adv.* **2014,** *4*, 37746-37751.
26. Xiao, Y.; Cao, M.; Ren, L.; Hu, C. Hierarchically porous germanium-modified carbon materials with enhanced lithium storage performance. *Nanoscale* **2012,** *4*, 7469.7474.
27. Kitschke, P.; Walter, M.; Ruffer, T.; Seifert, A.; Speck, F.; Seyller, T.; Spange, S.; Lang, H.; Auer, A. A.; Kovalenko, M. V.; Mehring, M. Porous ge@c materials via twin polymerization of germanium(ii) salicyl alcoholates for li-ion batteries. *J. Mater. Chem. A* **2016,** *4*, 2705-2719.
28. Hwang, J.; Jo, C.; Kim, M. G.; Chun, J.; Lim, E.; Kim, S.; Jeong, S.; Kim, Y.; Lee, J. Mesoporous ge/geo2/carbon lithium-ion battery anodes with high capacity and high reversibility. *ACS Nano* **2015,** *9*, 5299-5309.
29. Li, X.; Liang, J.; Hou, Z.; Zhu, Y.; Wang, Y.; Qian, Y. A synchronous approach for facile production of ge-carbon hybrid nanoparticles for high-performance lithium batteries. *Chem. Commun.* **2015,** *51*, 3882-3885.
30. Cui, G.; Gu, L.; Zhi, L.; Kaskhedikar, N.; Aken, P. A. van; Mullen, K.; Maier, J. A germanium-carbon nanocomposite material for lithium batteries. *Adv. Mater.* **2008,** *20*, 3079-3083.
31. Ngo, D. T.; Kalubarme, R. S.; Le, H. T. T.; Fisher, J. G.; Park, C. N.; Kim, I. D.; Park, C. J. Carbon-interconnected ge nanocrystals as an anode with ultra-long-term cyclability for lithium ion batteries. *Adv. Funct. Mater.* **2014,** *24*, 5291-5298.
32. Li, D.; Wang, H.; Liu, H. K.; Guo, Z. A new strategy for achieving a high performance anode for lithium ion batteries – encapsulating germanium nanoparticles in carbon nanoboxes. *Adv. Energy Mater.* **2016,** *6*, 1501666.
33. Xiao, Y.; Cao, M. High-performance lithium storage achieved by chemically binding germanium nanoparticles with n-doped carbon. *ACS Appl. Mater. Interfaces,* **2014,** *6*, 12922-12930.
34. Xiao, Y.; Cao, M. Freeze-drying-assisted synthesis of hierarchically porous carbon/germanium hybrid for high-efficiency lithium-ion batteries. *Chem. Asian J.* **2014,** *9*, 2859-2865.
35. Xue, D. J.; Xin, S.; Yan, Y.; Jiang, K. C.; Yin, Y. X.; Guo, Y. G.; Wan, L. J. Improving the electrode performance of ge through ge@c core-shell nanoparticles and graphene networks. *J. Am. Chem. Soc.* **2012,** *134*, 2512-2515.
36. DiLeo, R. A.; Frisco, S.; Ganter, M. J.; Rogers, R. E.; Raffaelle, R. P.; Landi, B. J. Hybrid germanium nanoparticles-single-wall carbon nanotube free-standing anodes for lithium ion

batteries. *J. Phys. Chem. C* **2011,** *115*, 22609-22614.

37. Chockla, A. M.; Panthani, M. G.; Holmberg, V. C.; Hessel, C. M.; Reid, D. K.; Bogart, T. D.; Harris, J. T.; Mullins, C. B.; Korgel, B. A. Electrochemical llithiation of graphene-supported silicon and germanium for rechargeable batteries. *J. Phys. Chem. C* **2012,** *116*, 11917-11923.
38. Kim, C.; Ko, M.; Yoo, S.; Chae, S.; Choi, S.; Lee, E.; Ko, S.; Lee, S. Y.; Cho, J.; Park, S. Novel design of ultra-fast si anodes for li-ion batteries: crystalline si@amorphous si encapsulating hard carbon. *Nanoscale* **2014,** *6*, 10604-10610.
39. Kim, C.; Choi, S.; Yoo, S.; Kwon, D.; Ko, S.; Kim, J. M.; Lee, S. Y.; Kim, I. D.; Park, S. A facile route for growth of cnts on si@hard carbon for conductive agent incorporating anodes for lithium-ion batteries. *Nanoscale* **2015,** *7*, 11286-11290.
40. Hwang, G.; Kim, J. M.; Hong, D.; Kim, C. K.; Choi, N. S.; Lee, S. Y.; Park, S. Multifunctional natural agarose as an alternative materials for high-performance rechargeable lithium-ion batteries. *Green Chem.* **2016,** *18*, 2710-2716.
41. Leveque, G.; Abanades, S. Investigation of thermal and carbothermal reduction of volatile oxides (zno, sno2, geo2, and mgo) via solar-driven vacuum thermogravimetry for thermochemical production of solar fuels. *Thermochim. Acta* **2015,** *605*, 86-94.
42. Sun, L.; Wang, L.; Tian, Ch.; Tan, T.; Xie, Y.; Shi, K.; Li, M.; Fu, H. Nitrogen-doped graphene with high nitrogen level via a one-step hydrothermal reaction of grahpene oxide with urea for superor capacitive energy storage. *RSC Adv.* **2012,** *2*, 4498-4506.
43. Reitz, C.; Breitung, B.; Schneider, A.; Wang, D.; Lehr, M. von der; Leichtweiss, T.; Janek J.; Hahn, H.; Brezesinski, T. Hierarchical carbon with high nitrogen doping level: a versatile anode and cathode host material for long-lie lithium-ion and lithium-sulfur batteries. *ACS Appl. Mater. Interfaces* **2016,** *8*, 10274-10282.
44. Ngo, D. T.; Kalubarme, R. S.; Le, H. T. T.; Park, C. N.; Park, C. J. Conducting additive-free amorphous geo2/c composite as a high capacity and long-term stability anode for lithium ion batteries. *Nanoscale* **2015,** *7*, 2552-2560.
45. Holzwarth, U.; Gibson, N. The scherrer equation versus the 'debye-scherrer equation'. *Nat. notechnol.* **2011,** *6*, 534-534.
46. Ren, J. G.; Wu, Q. H.; Tang, H.; Hong, G.; Zhang, W.; Lee, S. T. Germanium-graphene composite anode for high-energy lithium batteries with long cycle life. *J. Mater. Chem. A* **2013,** *1*, 1821-1826.
47. Hernandez, M. P.; Farias, M. H.; Castillon, F. F.; Diaz, J. A.; Avalos, M.; Ulloa, L.; Gallegos, J. A.; Yee-Madeiros, H. Growth and characterization of polycrystalline ge1-xcx by reactive pulsed laser deposition. *Appl. Surf. Sci.* **2011,** *257*, 5007-5011.

48. Kaskhedikar, N. A.; Maier, J. Lithium storage in carbon nanostructures. *Adv. Mater.* **2009**, *21*, 2664-2680.
49. Yang, S.; Feng, X.; Zhi, L.; Cao, Q.; Maier, J.; Mullen, K. Nanographene-constructed hollow carbon spheres and their favourable electroactivity with respect to lithium storage. *Adv. Mater.* **2010**, *22*, 838-842.
50. Buiel, E.; Dahn, J. R. Li-insertion in hard carbon anode materials for li-ion batteries. *Electrochim. Acta* **1999**, *45*, 121-130.
51. Zheng, F.; Yang, Y.; Chen, Q. High lithium anodic performance of highly nitrogen-doped porous carbon prepared from a metal-organic framework. *Nat. Commun.* **2014**, *5*, 5261.
52. Hou, J.; Cao, C.; Idrees, F.; Ma, X. Hierarchical porous nitrogen-doped carbon nanosheets derived from silk for ultrahigh-capacity battery anodes and supercapacitors. *ACS Nano* **2015**, *9*, 2556-2564.
53. Wang, X.; Lv, L.; Cheng, Z.; Gao, J.; Dong, L.; Hu, C.; Qu, L. High-density monolith of n-doped holey graphene for ultrahigh volumetric capacity of li-ion batteries. *Adv. Energy Mater.* **2016**, *6*, 1502100.
54. Lee, J. K.; Oh, C.; Kim, N. Hwang, J. Y.; Sun, Y. K. Rational design of silicon-based composites for high-energy storage devices. *J. Mater. Chem. A* **2016**, *4*, 5366-5384.
55. Yoon, S.; Park, C. M.; Sohn, H. J. Electrochemical characterizations of germanium and carbon-coated germanium composite anode for lithium-ion batteries. *Electrochem. Solid State Lett.* **2008**, *11*, A42-A45.
56. Laforge, B.; Jodin, L. L.; Salot, R.; Billard, A. Study of germanium as electrode in thin-film battery. *J. Electrochem. Soc.* **2008**, *155*, A181-A188.
57. Choi, S.; Kim, J.; Choi, N. S.; Kim, M. G.; Park, S. Cost-effective scalable synthesis of mesoporous germanium particles via a redox-transmetalation reaction for high-performance energy storage devices. *ACS Nano* **2015**, *9*, 2203-2212.
58. Ryu, J.; Hong, D.; Shin, M.; Park, S. Multiscale hyperporous silicon flake anodes for high initial coulombic efficiency and cycle stability. *ACS Nano* **2016**, *10*, 10589-10597.
59. Ryu, J.; Hong, D.; Choi, S.; Park, S. Synthesis of ultrathin si nanosheets from natural clays for lithium ion battery anodes. *ACS Nano* **2016**, *10*, 2843-2851.
60. Lee, K. J.; Choi, S.; Park, S.; Moon, H. R. General recyclable redox-metallothermic reaction route to hierarchically porous carbon/metal composites. *Chem. Mater.* **2016**, *28*, 4403-4408.

61. Kim, C.; Hwang, G.; Jung, J.; Cho, S.; Cheong, J.; Shin, S.; Park, S.; Kim, I. D. Fast, scalable synthesis of micronized ge3n4@c with a high tap density for excellent lithium storage. *Adv. Funct. Mater.* **2017**, *27*, 1605975.
62. Ruffo, R.; Hong, S. S.; Chan, C. K.; Huggins, R. A.; Cui, Y. Impedance analysis of silicon nanowire lithium ion battery anodes. *J. Phys. Chem. C* **2009**, *113*, 11390-11398.
63. Wang, X.; Yang, A.; Xia, S. Fracture toughness characterization of lithiated germanium as an anode material for lithium-ion batteries. *J. Electrochem. Soc.* **2016**, *163*, A90-A95.
64. Verma, P.; Marie, P.; Novak, P. A review of the features and analyses of the solid electrolyte interphase in Li-ion batteries. *Electrochim. Acta* **2010**, *55*, 6332-6341.
65. Zhang, C.; Lin, Z.; Yang, Z.; Xiao, D.; Hu, P.; Xu, H.; Duan, Y.; Pang, S.; Gu, L.; Cui, G. Hierarchically designed germanium microcubes with high initial coulombic efficiency toward highly reversible lithium storage. *Chem. Mater.* **2015**, *27*, 2189-2194.

Chapter IV. Unraveling the mechanism of carbon nanodot-assisted lithium plating/stripping for stable lithium metal batteries

4.1 Introduction

With the demands for high-energy density storage systems, replacing conventional graphite anodes in lithium-ion batteries provides a significant opportunity to resolve the limitations of a conventional battery in future applications. Among the diverse candidates, Li metal is a suitable choice owing to its high specific capacity (3,860 mA h g^{-1}) and lowest electrochemical potential (-3.04 V vs. the standard hydrogen electrode). However, thermodynamically unsteady states, for example, the rough surface of the current collector or Li metal, cause uncontrollable Li deposition during the electrochemical cycles. This dendritic growth of Li metal raises several critical issues of low Coulombic efficiency, electrolyte depletion, and safety concerns. Therefore, Li dendrite management has been widely studied in the past decades for the stable cycling of Li metal batteries (LMBs).[1-4]

To address the risks originating from Li dendrite formation, several approaches for dendrite suppression have been proposed, such as the artificial solid–electrolyte interface (SEI) coating for depositing Li metal between the current collector and protecting layer,[5-10] high-concentration ether-based electrolyte for smooth Li plating,[11-16] artificial structuring of anode to cage the grown Li metal in the matrix,[17-21] and introduction of electrolyte additives for building a stable interface.[22-26] The aforementioned strategies have accomplished significant progress both in terms of morphology control and electrochemical performance. Nevertheless, it is still highly desirable to improve the insufficient battery performance compared to commercial Li-ion batteries as well as to provide a fundamental mechanistic analysis of Li dendrite suppression for practical usage of Li metal anodes.

The key element for the Li dendrite control lies in the homogeneous deposition of Li during the plating process. Without any treatment, the uneven nucleation of Li deposition and the concomitant growth of needle-like Li metal results in battery failure using conventional lithium hexafluorophosphate-containing carbon electrolytes with the main issues being the continuous SEI/crack formation, electrolyte consumption, and high cell resistance.[23] In this regard, the electrolyte additive strategy for dealing with dendrite formation provides a simple but universally applicable solution that can systematically control the nature of the interface and guide uniform

metal deposition, which are promising for its feasibility on the industrial scale. Although partial improvement in the Li growth morphology and cyclability of LMBs using several additives has been reported, the battery performance and stability still significantly lag the commercial level.[24-26] Therefore, new concepts of Li-ion adsorption materials (such as LMBs) are proposed for the prevention of the disordered Li metal reduction by employing the strong affinity between Li ions and functional groups (Fig. 4-1). In particular, Cheng et al. employed a nanoscale diamond as an electrolyte additive providing nucleation sites for Li toward uniform Li metal deposition.[27] Despite its potential for controlling the Li metal deposition, the large-sized carbon clusters (>500 nm) present limitation in the uniformity of the surface deposition and columnar morphology of the Li metal on the electrode.

Herein, we introduce a nanoscale carbon dot or carbon nanodot (CD) as an electrolyte additive for shuttling the Li ions for achieving a uniform deposition of Li metal. Specifically, CDs are mass-producible in a single step from simple organic precursors and are highly dispersible in a carbonate-containing electrolyte used for LMBs. The synergistic interplay between the highly negative surface charges and configuration of the nitrogen in the CD play a critical role in establishing a strong Li ion affinity, as determined by various characterizations and computational analysis. This CD-based shuttling not only provides the nucleation sites for the Li ions but also assists homogeneous Li plating, eventually leading to excellent battery durability. We further perform ex situ transmission electron microscopy (TEM) analyses for observing the Li plating/stripping morphology to identify the role of the CD shuttles. The novel CD-dispersed electrolytes showed excellent electrochemical performances, delivering 95.5% of the average Coulombic efficiency for 100 cycles in a half cell, stable overpotential value for 500 cycles in a symmetric cell, and 99.9% of the capacity retention after 100 cycles of the full cell. Overall, the CD-assisted homogeneous Li deposition suggests a new design paradigm toward the practical usage of LMBs.

4.2 Experimental

Synthesis of Carbon Nanodots

CDs were synthesized by different carbonization methods. To prepare the N-CD, 960 mg of citric acid (5.0 mmol, Aldrich) and 347 mL of ethylene diamine (5.0 mmol) were dissolved in 10 mL of water under vigorous stirring for 2 min. The solution was placed in a microwave oven (commercial household microwave, 700 W) and heated for 2 min, and a yellow solid was obtained after cooling to room temperature. The solid was diluted in 5.0 mL of water. The yellow suspension was dialyzed (SpectraPore MWCO 500 – 1,000) for 2 days to remove the salts and unreacted chemicals. For the preparation of the U-CD, 3 mmol of citric acid was dissolved in 10 mL of DMF.[34] Urea (10 mmol) was added into the DMF solution, followed by a solvothermal reaction at 180 °C for 12 h in a sealed Teflon-lined autoclave. After cooling to room temperature, an excess of ethyl acetate was added to the dark brown solution to induce precipitation. After several washings using a mixture of ethyl acetate and methanol, the black powder was dried in a vacuum oven.

Material Characterization

The microstructural evolution was investigated via scanning electron microscopy, (S-4800, Hitach), TEM (JEM-2100, JEOL), STEM (Tecnai G2 F20 X-Twin, FEI), Raman (alpha300R, WITec), FT-IR analysis (670-IR, Varian), zeta-potential analysis (Zeta-potential analyzer, Nano-zs, Malvern), XPS (K-alpha, Thermo Fisher), and element analysis (Element Analyzer, Flash 2000, Thermo Fisher).

Density Functional Theory Method

The structural optimization and total energy calculation were performed using Gaussian 09 at the level of PBE/6-31G*.[35-36] The equilibrium structure was confirmed by the absence of a negative frequency mode. For each optimized geometry of the functionalized CD with Li+ bonded, the binding energy, defined as E(CD-Li+) – E(CD) – E(Li+), was calculated with the basis set superposition error corrected by the counterpoise method

Electrolyte Preparation

A series of synthesized CDs was added in 5 mL of 1.3 M $LiPF_6$ ethylene carbonate/diethyl carbonate (EC/DEC, 3/7 vol.%) solution under argon atmosphere with the target concentration of 0.01–5 mg mL^{-1}. Then, vigorous stirring and ultrasonication were conducted for the uniform distribution of the CD particles. The achieved CD suspensions maintained the degree of dispersion for over a month, which enabled homogeneous Li plating.

***Ex situ* TEM Measurements**

Ex situ TEM analysis was performed with Li plating/stripping on a copper TEM grid. By using a 2032-coin type Li/Cu half-cell system and locating the TEM grid between the current collector and Li metal, electrochemical Li plating/stripping successfully occurred on the TEM grid. To determine the role of the U-CD fundamentally, various states (bare, electrolyte dropping, rinsing, Li plating, Li stripping, and Li re-plating) of the TEM grid with and without the U-CD were prepared. A series of TEM grids was obtained by disassembling the coin cells in an argon-filled glove box and then transported to the TEM holder.

Electrochemical Characterization

Electrochemical tests were performed using a 2032 coin-type Li/Cu half-cell, Li/Li symmetric-cell, and Li/cathode full-cell. The Li/Cu half-cell was composed of a Cu current collector, polymer separator (Celgard 2400), and a lithium electrode (20 μm, 300 μm thickness, Honjo). In the case of the symmetric cell, the Cu current collector was substituted by 300 μm lithium. For the full cell, a 20 μm-thick lithium electrode was combined with the $LiCoO_2$ (LCO, L&F Inc.) electrode. The LCO cathode consisted of 95 wt.% of an active material, 2.5 wt.% binder (polyvinylidene fluoride (PVDF, KUREHA KF 1100), and 2.5 wt.% super-P (TIMCAL), which was prepared by the slurry coating method with a loading level of ~7 mg cm^{-2}. The electrolyte was a 1.3 M $LiPF_6$ solution in EC/DEC (3/7 vol.%) with 0.01–5 mg mL^{-1} carbon dot additives included to improve the cycling stability. The operating conditions were 1.0 V stripping cut-off voltage with a specific capacity of 1 mA h cm^{-2} at 0.1–1 C-rate for the Li/Cu half-cell, 0.5–1 mA h cm^{-2} at 1–5 C-rate for the Li/Li symmetric-cell, and 3.0–4.45 V voltage window with 0.1–1 C-rate for the Li/LCO full-cell. The electrochemical properties were measured using a cycle tester (WBCS3000 battery systems, Wonatech).

4.3 Results and discussion

The chemical structures and related surface states of the CDs are precisely tunable with different types of precursors and synthetic protocols.[28] Accordingly, we prepared various CDs with different physical and chemical properties (Fig. 4-2a). A urea-based nitrogen-functionalized carbon nanodot (U-CD) was prepared through a solvothermal decomposition of citric acid and urea in N,N-dimethylformamide (DMF) (see experimental section for details). Additionally, we synthesized an ethylene diamine-based nitrogen-functionalized carbon nanodot (N-CD) from microwave pyrolysis using citric acid and ethylenediamine as reported in our previous study.[29] After purification, all the CDs were well-dispersed in various concentrations (in the range of 0.01 to 5 mg mL^{-1}) of the carbonate electrolyte, without any noticeable precipitation for several months (Figure S1, Supporting Information). The synthesized CDs represent the negative ζ-potential values of –5.0 ± 1.6 (N-CD) and –25.1 ± 0.6 mV (U-CD) in water, suggesting the presence of negatively charged groups on the surface of the CDs (Figure S2, Supporting Information). Moreover, Fourier transform infra-red (FT-IR) spectroscopy was performed to identify the functional groups of the U-CD and N-CD (Figure S3, Supporting Information). The FT-IR spectra reveal that both the U-CD and N-CD display a broad peak at 3222 cm^{-1} correspondings to the O-H and N-H stretching. Interestingly, the peak intensity of carboxylic acid is considerably higher with the U-CD than that achieved with the N-CD at 1709 cm^{-1}, which is in accordance with the ζ-potential measurement.

Elemental analysis (EA) and X-ray photoelectron spectroscopy (XPS) measurements were performed to further investigate the chemical compositions and structures of the N-CD and U-CD. The major components of the N-CD and U-CD are determined to be C, N, and O (Figure S4, Supporting Information). The deconvoluted C 1s and N 1s XPS spectra reveal the presence of O and N-based functional groups in the CDs, which can serve as the interaction sites with Li ions (Figure S5, Supporting Information). The high-resolution C 1s spectra yield the different fractions of the oxygen functional groups in the N-CD and U-CD (Fig. 4-2b and Figure S6a, Supporting Information). The U-CD is found to contain 3.2% of the carboxylic acid groups (288.6 eV), whereas the N-CD only contains 1.0% of the carboxylic acid groups, which is in good agreement with the ζ-potential and FT-IR results.

It is well known that both oxygen groups and nitrogen-related edge states such as pyrrolic-N and pyridinic-N are critical for the formation of Li–CD clusters owing to the presence of the lone-pair electrons of N.[30] As shown in Fig. 4-2c and Figure S6b (Supporting Information), the N-CD and U-CD include N configurations such as pyrrolic-N, pyridinic-N, and graphitic-N.

Interestingly, however, the fractions of the different N configurations in each CD are significantly different. Specifically, pyrrolic-N (7.6%) and graphitic-N (4.4%) are dominant in the N-CD, whereas the U-CD includes the major contents of 9.1% of pyrrolic-N and 7.8% of pyridinic-N. Thus, the combination of the negative charges and abundant surface states allows the U-CD to provide more active sites for Li-ion absorption.

To prove this assignment, the binding energy of the interaction between the Li ions and functional groups of the CDs was calculated by the density functional theory (DFT) method (Note S1, Supporting Information). The structure of the CDs was simplified by placing different functional groups in a two-dimensional (2D) graphitic structure, albeit with the fact that its three-dimensional (3D) model allows a better description to understand the correlation between the Li ions and functional groups. Based on the combined experimental results from the EA and XPS and focusing on the most probable role of the edge functional groups, we constructed a small sp2-carbon model, which possesses various distinct functional groups and structures, such as carbonyl, carboxylic, pyrrolic-N, and pyridinic-N groups (Fig. 4-2d and Figure S7–S9, Supporting Information). First, we examined the binding effect between each functional group and Li ions. According to the DFT calculation of the O-related groups, functional groups such as carbonyl (-2.84 eV) and carboxylic (-2.68 eV) present in the CDs are preferred for Li-ion absorption compared to the N-related groups (Fig. 4-2e). Among the N configurations, the pyridinic-N (-2.29 eV) has a slightly larger binding energy than the pyrrolic-N (-2.10 eV). The negative Mulliken charges of the respective O and N atoms (-0.62 for the ketone O, -0.60 for the pyridinic-N, and -0.58 for the pyrrolic-N) suggest that the major interaction is of ionic type. However, when Li ions are placed between two functional groups, the binding energies of the pyridinic-N and pyrrolic-N increase significantly owing to the synergetic effect (Fig. 4-2f). In particular, the combination of the pyridinic-N and carboxylic acid groups is strong, as indicated by the strong binding energy of -3.45 eV, whereas the binding energy of the pyrrolic-N interaction with the carboxylic acid groups is only -1.80 eV (Table S1, Supporting Information). This is because the Li ions bonded to the pyridinic-N can form another ionic bond with a carbonyl, which is not possible for pyrrolic-N owing to a long distance to the nearby oxygen group. We, therefore, expect that the U-CD, which contained abundant carboxylic acid groups and N-edge states, can provide strong interaction and uniform nucleation sites for the Li ions.

Ex situ TEM was utilized to illuminate the role of the CDs during cycling.[31,32] Among the various CDs, we selected the U-CD owing to its strongest affinity for Li ions. To prepare the TEM sample, we used the electrochemical plating/stripping method performed on a Cu-based TEM grid instead of a Cu current collector. Various TEM samples (e.g., bare grid, electrolyte dropping,

rinsing, plating, and stripping) have been designed for the thorough investigation of the Li growth morphology in the presence of the U-CD. As shown in Figure S10 (Supporting Information), the U-CD-dispersed electrolyte cannot get adsorbed physically on the current collector without applying an electrochemical driving force.

To confirm the supporting effect of the U-CD, we observed the behavior of the Li plating/stripping with and without the U-CD through the TEM and high-angle annular dark-field scanning transmission electron microscopy (HAADF-STEM) analysis. Li plating performed without the CDs resulted in significant growth of the Li dendrite covering the entire grid with the development of a thick SEI layer (Fig. 4-3a, e, i). These disordered Li branches were broken during the stripping process and exposed to the reaction between the Li and electrolyte, resulting in continuous SEI formation and cracking, which in turn resulted in low Coulombic efficiency and poor cyclability (Fig. 4-3b, f, j). For the U-CD-containing electrolyte, strong interactions of the U-CD surface shuttled the Li ion for achieving a uniform Li plating. The corresponding TEM images exhibit a uniform distribution of approximately 5 nm-sized particles along the inner and outer sur-faces of the grid with smooth Li stacking (Fig. 4-3c, g, k). The well-overlaid U-CD successfully suppresses dendrite growth without any side reaction, thereby yielding an immaculate Li surface and a stable SEI. More importantly, there are no macroscopic shape differences between the U-CD-aided stripping and plating samples (Figure 3l). The microscopic images and EDS analysis indicate that the SEI is converted into a porous structure owing to the liberation of the surface containing U-CD, which thereby decreases the density of the adsorbed U-CD (Fig. 4-3d, h, and Figure S11, Supporting Information). Furthermore, we verify that the partially desorbed U-CD is recyclable, and examination of a series of TEM images indicates that there are few structural differences even after 100 cycles, which supports a long-term operation of the LMBs (Figure S12, Supporting Information).

For further exploration of the role of the CD additives, we performed an electrochemical analysis. The results of the Li/Cu half-cell test indicate that the overpotential values are reduced in the order of the pristine electrolytes, N-CD, and U-CD (Fig. 4-4a). The initial Coulombic efficiency (ICE) of three samples is practically identical at approximately 95.0%; however, the cycle durability for each sample is distinguishable (Figure S13, Supporting Information). This demonstrates that the CD additives reduce the cell resistance effectively during Li deposition, which can be attributed to the combination of the negative surface charges and binding energy against the Li ions as determined by the DFT calculation. As such, the U-CD demonstrates the lowest overpotential and most stable cyclability with an average Coulombic efficiency of 95.5%. Moreover, the Li/Li symmetric-cell tests were used to verify the resistance decrease in the

presence of the CD additives, which agreed well with the Li/Cu half-cell results obtained with a U-CD that had good cycle performances over 100 cycles (Fig. 4-4b and Figure S14, Supporting Information). Additionally, to determine the optimal condition of the electrolyte, we conducted a Li/Li symmetric-cell test un-der diverse concentrations of the U-CD in a wide range from 0.01 to 5.0 mg mL^{-1} (Figure S15, Supporting Information). The 0.5 mg mL^{-1} of the U-CD exhibits the best performance among them (Fig. 4-4c-d, Table S2, and Figure S16–S17, Supporting Information). This is because the dilute sample cannot attract Li ions effectively, whereas an extremely high concentration of the CD increases the cell resistance instead (Note S2, Supporting Information).

The morphology of the Li deposition was investigated from various aspects. We inspected the cycled Li metal in the absence and presence of the U-CD. For Li deposition on a Cu foil without the CDs, agglomeration of Li metal occurs with cycle progression, whereas plating with the U-CD results in uniform Li metal distribution (Figure S18, Supporting Information). These Li growth trends are also observed in the symmetric cell (Figure S19, Supporting Information). The XPS spectra of the cycled Li metal exhibit a reduced overall peak intensity in the U-CD sample, which successfully prevents the formation of extra SEI originating from the surface crack and electrolyte decomposition (Figure S20, Supporting Information).[26,33] In addition, the morphological differences are confirmed using a scanning electron microscope (SEM). The images of the sample without the U-CD additives display a broken Li array and thick degradation layer (Fig. 4-5a, c). In contrast, the U-CD allows not only suppression of Li dendrite growth but also the formation of a stable SEI with minimal electrolyte consumption and degradation (Fig. 4-5b, d). A smooth Li accumulation morphology assisted by the U-CD is observed and confirms that the overpotential is closely related to the morphology of the Li layer. Lastly, an ultrathin 20 μm-thick Li foil (approximately 4 mA h cm^{-2}) was matched with the $LiCoO_2$ (LCO) cathode to perform a full-cell test to confirm the practical usage of the LMB. The ICE value is determined to be 93.5% for the sample without the CD and 96.6% for the sample with the U-CD (Fig. 4-5e). The battery efficiency gap stands out during the cycling test, which shows the average Coulombic efficiency is 98.1% without the CD and 99.1% with U-CD. In addition, after 100 cycles, the capacity retention efficiency of the system is 57.9% without the CD and 99.9% with the U-CD (Fig. 4-5f). The U-CD-aided outstanding battery improvement is also verified under manifold cycling conditions (Figure S21, Supporting Information).

The well-designed nitrogen-functionalized CDs exhibited Li dendrite suppression ability and excellent electrochemical performance as the electrolyte additive. This CD effectively guided the Li plating and stripping processes as follows: The combination of the surface negative charges of

the CD and strong binding energy of the Li ions to the various carbon and nitrogen configurations attracted the Li ions by an electrostatic force at the initial stage of the electrochemical tests. It also built CD–Li-ion clusters, resulting in the enhancement of the Li-ion shuttle ability. Therefore, the CD–Li-ion moved together to the current collector under the electric field, and the solution flowed during the plating. In this stage, the CD–Li-ion groups are affected by the repulsive force for each other, resulting in a uniform distribution on the current collector. The well-guided Li ions that are adjacent to the current collector accept electrons and are reduced to Li metal with the confinement of the CDs. This reduced Li metal is affected by the initial nuclei size, which causes Li metal surface fluctuation. Thus, minimizing the seed size is critical for obtaining a uniform deposition. Because 2~5 nm-sized CDs are well-distributed in the entire system, homogeneous Li stacking can occur with uniform SEI formation. In the process of Li stripping, the solid phase Li returns to its ionic state by losing electrons with the escape of the trapped CDs. However, basically, the CDs can-not penetrate the SEI; therefore, only the outer-surface-adsorbed particles re-disperse into the electrolyte, leaving a porous interface trace. These CDs reunite with the Li ions owing to the electric force and can be used reversibly during cycling. From these results, we revalidate that the functionalized U-CDs operate well regardless of the cell types, such as a half-cell, symmetric-cell, and even a full-cell, because of the uniform Li plating/stripping induction. We anticipate that the U-CDs can be applied to other types of LMB systems owing to its synthetic feasibility, superior dispersity in conventional electrolytes, and compatibility under battery operating conditions, thus presenting a significant potential in practical usage.

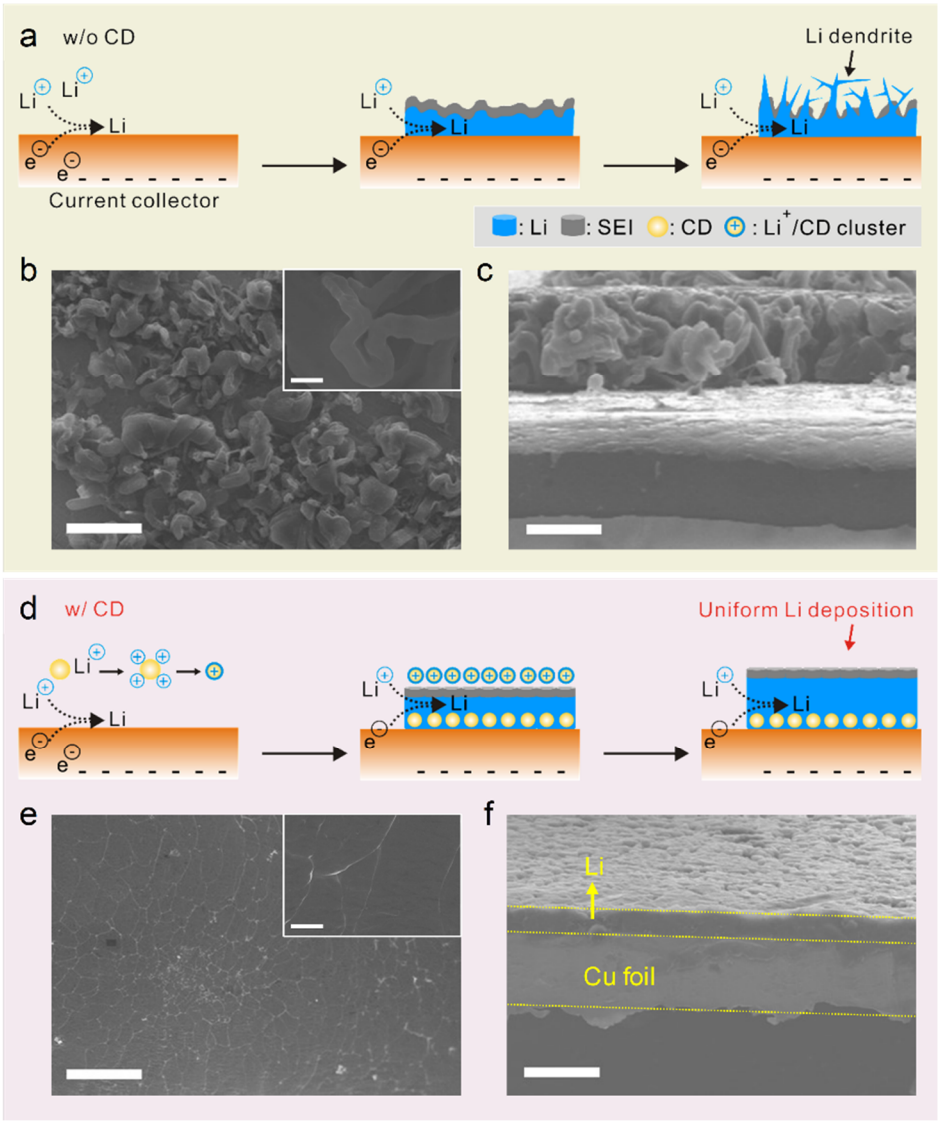

Figure 4-1. Schematic and SEM images of the Li deposition behavior on the current collector. a) Original nature of Li dendrite growth with-out using the carbon dot additives and b–c) corresponding SEM images of the top view (b, inset: high magnification image) and cross-sectional view (c). d) Carbon dot-assisted homogeneous Li plating and e–f) corresponding SEM images of the top view (e, inset: high magnification image) and cross-sectional view f). Scale bars are 20 μm (Inset: 500 nm) (b, c, e, and f).

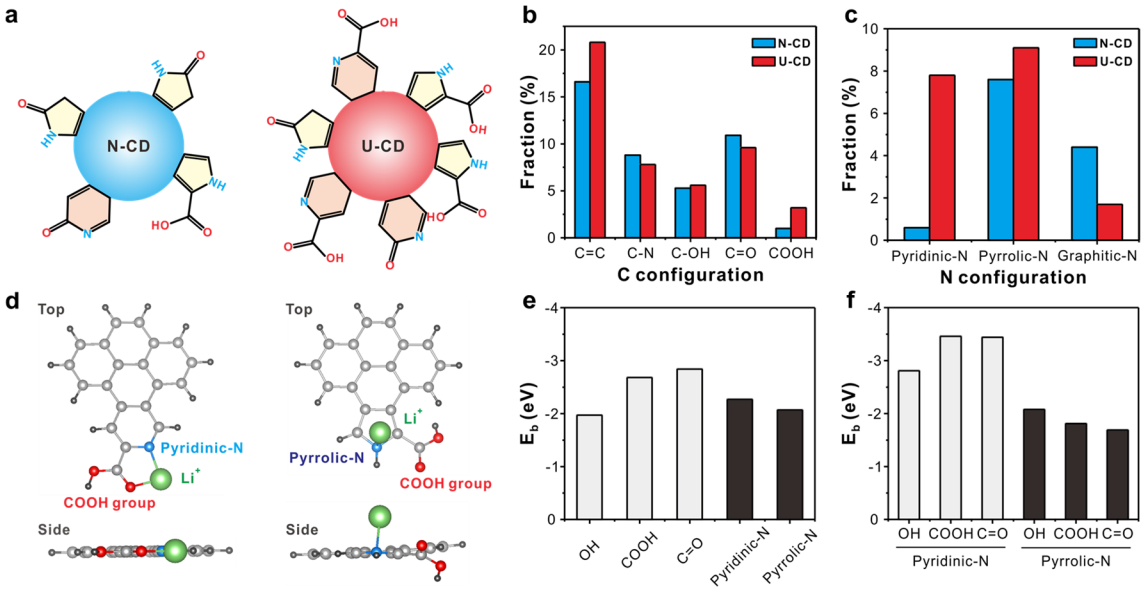

Figure 4-2. Chemical properties of the carbon dot additives. a) Structural illustration of the N-CD and U-CD. b–c) Chemical compositions of the N-CD and U-CD determined by high-resolution XPS spectra of C 1s (b) and N 1s (c), respectively. d) Model structures for the binding energy calculation of a Li ion and functional groups such as pyridinic-N, pyrrolic-N, and COOH. e–f) Binding energy of the Li ions as a function of the single functional group (e) and dual functional groups (f).

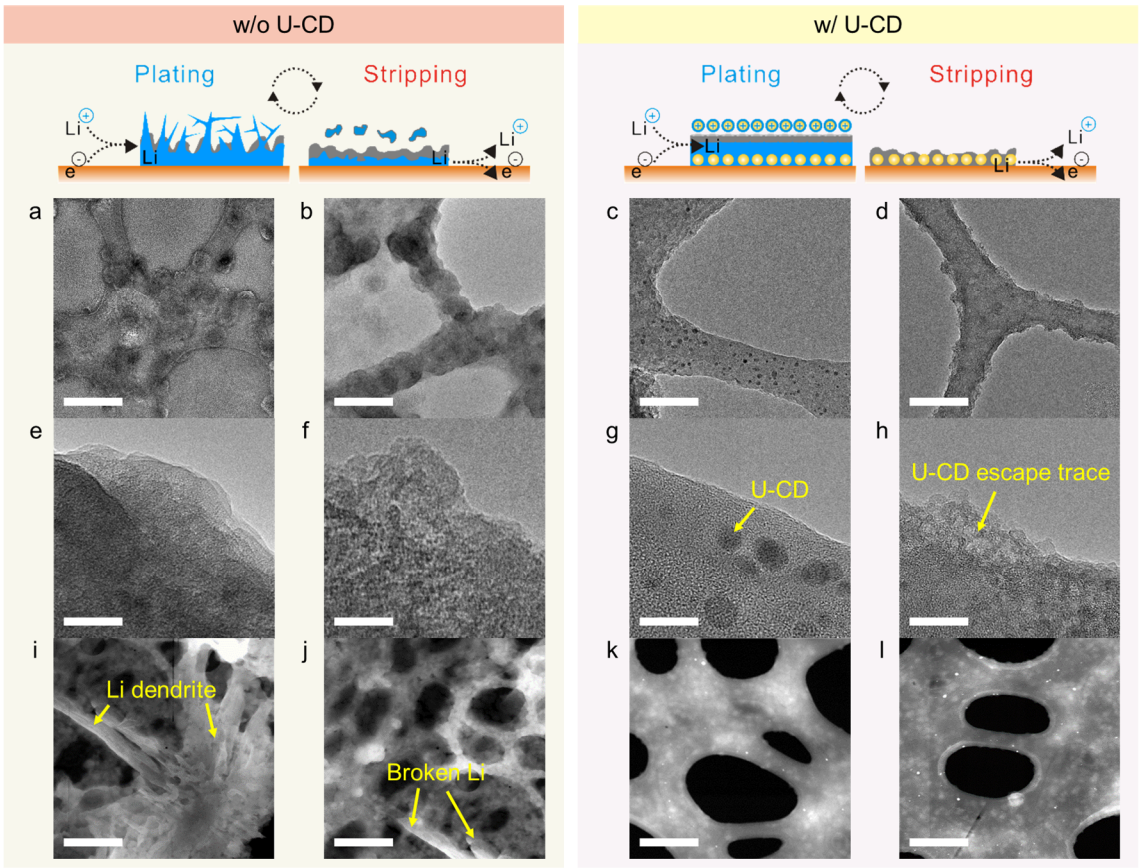

Figure 4-3. Behavior of the Li plating and stripping. A series of TEM images and HAADF-STEM images of a, e, i) plating without U-CD; b, f, j) stripping without U-CD; c, g, k) plating with the U-CD; and d, h, l) stripping with the U-CD. Scale bars are 100 nm (a–d), 10 nm (e–h), and 1 μm (i–l).

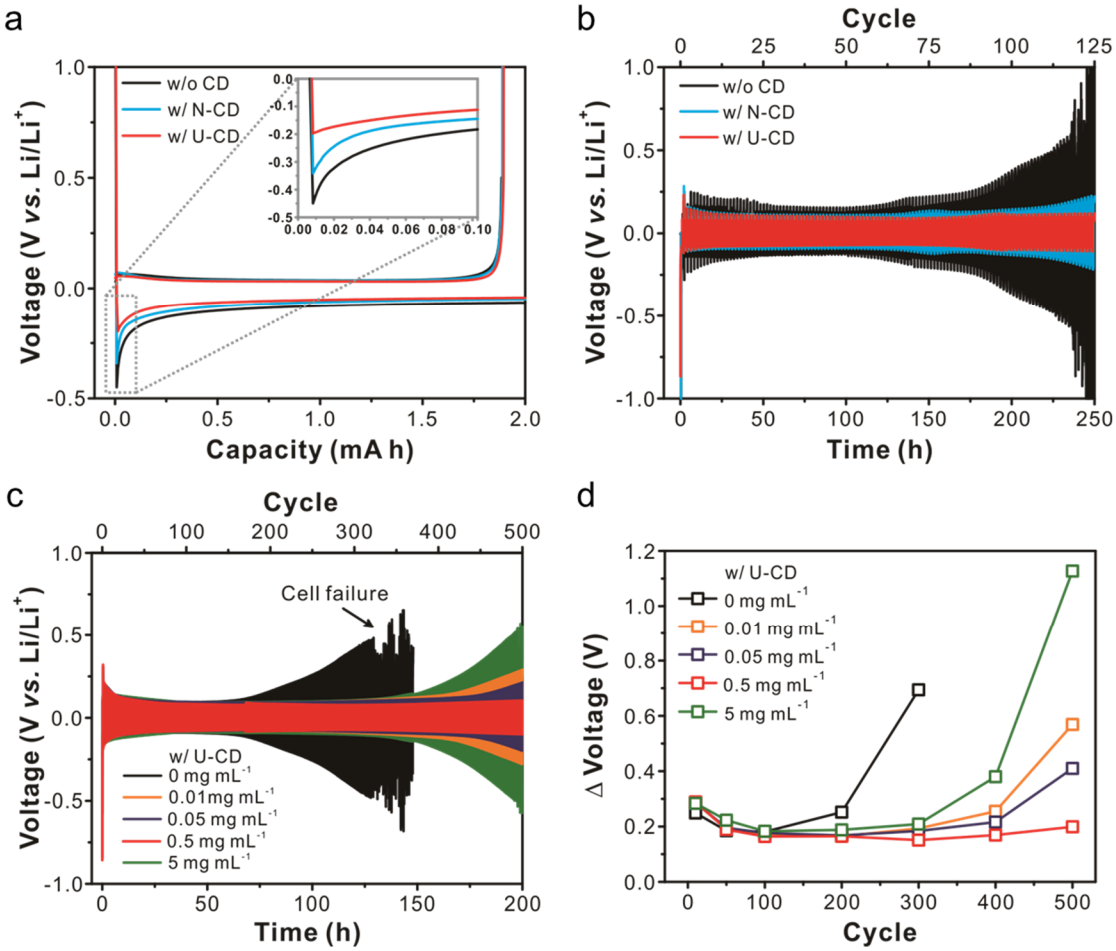

Figure 4-4. Overpotential minimization through U-CD additives. a) Initial galvanostatic voltage profiles of the Li/Cu half-cell at 0.1C-rate with areal capacity of 1 mA h cm^{-2}. b) Cycle retention properties of the Li/Li symmetric-cell at 1C-rate with areal capacity of 1 mA h cm^{-2}. c) Cycle retention properties and d) plots of the voltage differences of the Li/Li symmetric-cell at 5C-rate with areal capacity of 0.5 mA h cm^{-2} and electrolyte concentration control. The electrolyte concentration is 0.5 mg mL^{-1} (a, b).

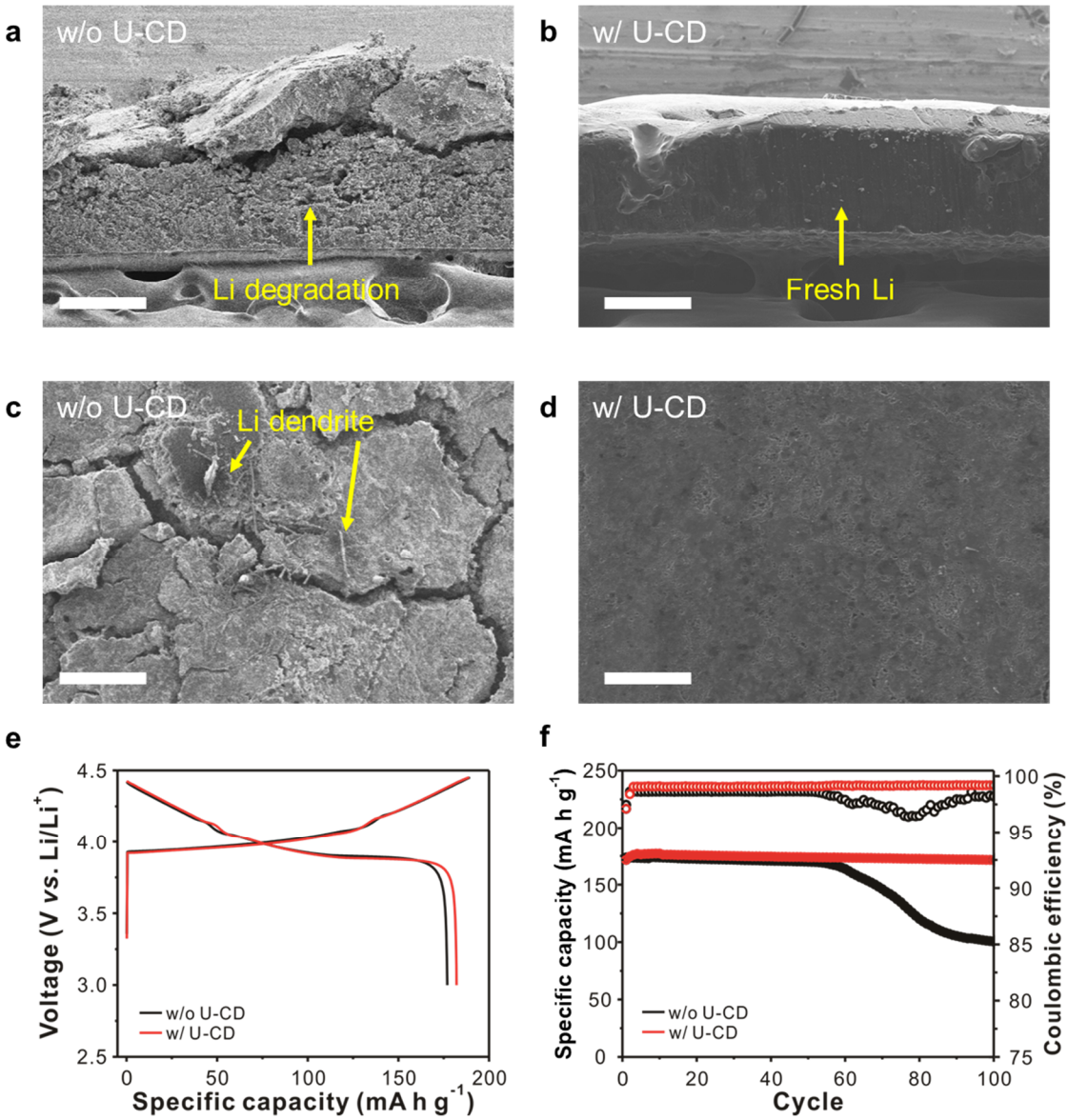

Figure 4-5. Stable electrochemical performances originating from the carbon dot-assisted plating. A series of SEM images of the Li metal a, c) without the CD; b, d) with the U-CD after 500 cycles. e) First-cycle voltage profile of the Li/LCO full-cell at 0.1C-rate with areal capacity of 1 mA h cm^{-2}. f) Cycle retention properties of the 20 μm Li/LCO extreme full-cell test at 1C-rate with areal capacity of 1 mA h cm^{-2}. Scale bars are 200 μm (a–d). The electrolyte concentration is 0.5 mg mL^{-1}.

4.4 Conclusions

To summarize, we suggest single-step mass-producible nitrogen-functionalized CDs as electrolyte additives for LMBs. The CDs contain diverse carbon and nitrogen functional groups, which are highly controllable by modifying the ratio of the organic precursors. The functionalized CDs exhibit tremendous potential for the suppression of unsteady Li deposition and display excellent electrochemical performances, which are attributed to the combination of the surface electric attraction force and strong Li ion affinity. Specifically, the small size of the CDs induces small initial Li nuclei, resulting in ideal Li stacking with stable SEI. This unique advancement of the CDs is also investigated in battery cycling tests. The Li/Cu half-cell tests conducted with the CDs deliver the lowest overpotential and 95.5% average Coulombic efficiency for 100 cycles at 1C-rate, whereas the results without the CDs show only 89.0% average Coulombic efficiency. In addition, the stable cycling of the CD-assisted Li/Li symmetric-cell tests continues up to 500 cycles under the condition of 0.5 mA h cm^{-2} and 2.5 mA cm^{-2}. In contrast, the potential difference of the pure Li/Li symmetric-cell already increases drastically before approaching 200 cycles. Even under extreme conditions of a 20-μm Li anode with an LCO cathode full-cell test, to which CD additives are applied, 99.1% average Coulombic efficiency for 100 cycles at 1C-rate and 99.9% capacity retention after 100 cycles are delivered (98.1% average Coulombic efficiency, 57.9% capacity retention without CD). One of the strengths of the electrolyte additive studied is its excellent applicability, posing a high potential in an industrial setup. Therefore, the systematic borderless CD additive-guided uniform Li plating will provide a new design paradigm for future LMBs.

4.5 Reference

1. Lin, D. C.; Liu, Y. Y.; Cui, Y. Reviving the lithium metal anode for high-energy batteries. *Nat. Nanotechnol.* **2017**, *12*, 194-206.
2. Zhang, R.; Li, N. W.; Cheng, X. B.; Yin, Y. X.; Zhang, Q.; Guo, Y. G. Advanced micro/nanostructures for lithium metal anodes. *Adv. Sci.* **2017**, *4*, 1600445.
3. Ye, H.; Xin, S.; Yin, Y. X.; Guo, Y. G. Advanced porous carbon materials for high-efficient lithium metal anodes. *Adv. Energy Mater.* **2017**, *7*, 1700530.
4. Lu, Y. Y.; Tu, Z. Y.; Archer, L. A. Stable lithium electrodeposition in liquid and nanoporous solid electrolytes. *Nat. Mater.* **2014**, *13*, 961-969.
5. Cheng, X. B.; Yan, C.; Chen, X.; Guan, C.; Huang, J. Q.; Peng, H. J.; Zhang, R.; Yang, S. T.; Zhang, Q. Implantable solid electrolyte interphase in lithium-metal batteries. *Chem* **2017**, *2*, 258-270.
6. Kim, M. S.; Ryu, J.-H.; Deepika; Lim, Y. R.; Nah, I. W.; Lee, K.-R.; Archer, L. A.; Il Cho, W. Langmuir–Blodgett artificial solid-electrolyte interphases for practical lithium metal batteries. *Nat. Energy* **2018**, *3*, 889-898.
7. Li, N. W.; Shi, Y.; Yin, Y. X.; Zeng, X. X.; Li, J. Y.; Li, C. J.; Wan, L. J.; Wen, R.; Guo, Y. G. A flexible solid electrolyte interphase layer for long-life lithium metal anodes. *Angew. Chem., Int. Ed.* **2018**, *57*, 1505-1509.
8. Li, N. W.; Yin, Y. X.; Yang, C. P.; Guo, Y. G. An artificial solid electrolyte interphase layer for stable lithium metal anodes. *Adv. Mater.* **2016**, *28*, 1853-1858.
9. Liu, Y. Y.; Lin, D. C.; Yuen, P. Y.; Liu, K.; Xie, J.; Dauskardt, R. H.; Cui, Y. An artificial solid electrolyte interphase with high Li-ion conductivity, mechanical strength, and flexibility for stable lithium metal anodes. *Adv. Mater.* **2017**, *29*, 1605531.
10. Tikekar, M. D.; Choudhury, S.; Tu, Z. Y.; Archer, L. A. Design principles for electrolytes and interfaces for stable lithium-metal batteries. *Nat. Energy* **2016**, *1*, 1-7.
11. Chen, S. R.; Zheng, J. M.; Mei, D. H.; Han, K. S.; Engelhard, M. H.; Zhao, W. G.; Xu, W.; Liu, J.; Zhang, J. G. High-voltage lithium-metal batteries enabled by localized high-concentration electrolytes. *Adv. Mater.* **2018**, *30*, 1706102.
12. Jiao, S. H.; Ren, X. D.; Cao, R. G.; Engelhard, M. H.; Liu, Y. Z.; Hu, D. H.; Mei, D. H.; Zheng, J. M.; Zhao, W. G.; Li, Q. Y.; Liu, N.; Adams, B. D.; Ma, C.; Liu, J.; Zhang, J. G.; Xu, W. Stable cycling of high-voltage lithium metal batteries in ether electrolytes. *Nat. Energy* **2018**, *3*, 739-746.
13. Qian, J. F.; Adams, B. D.; Zheng, J. M.; Xu, W.; Henderson, W. A.; Wang, J.; Bowden, M.

E.; Xu, S. C.; Hu, J. Z.; Zhang, J. G. Anode-free rechargeable lithium metal batteries. *Adv. Funct. Mater.* **2016**, *26*, 7094-7102.

14. Qian, J. F.; Henderson, W. A.; Xu, W.; Bhattacharya, P.; Engelhard, M.; Borodin, O.; Zhang, J. G. High rate and stable cycling of lithium metal anode. *Nat. Commun.* **2015**, *6*, 6362.
15. Ren, X. D.; Chen, S. R.; Lee, H.; Mei, D. H.; Engelhard, M. H.; Burton, S. D.; Zhao, W. G.; Zheng, J. M.; Li, Q. Y.; Ding, M. S.; Schroeder, M.; Alvarado, J.; Xu, K.; Meng, Y. S.; Liu, J.; Zhang, J. G.; Xu, W. localized high-concentration sulfone electrolytes for high-efficiency lithium-metal batteries. *Chem* **2018**, *4*, 1877-1892.
16. Suo, L. M.; Hu, Y. S.; Li, H.; Armand, M.; Chen, L. Q. A new class of solvent-in-salt electrolyte for high-energy rechargeable metallic lithium batteries. *Nat. Commun.* **2013**, *4*, 1481.
17. Liu, S. F.; Xia, X. H.; Zhong, Y.; Deng, S. J.; Yao, Z. J.; Zhang, L. Y.; Cheng, X. B.; Wang, X. L.; Zhang, Q.; Tu, J. P. 3D TiC/C core/shell nanowire skeleton for dendrite-free and long-life lithium metal anode. *Adv. Energy Mater.* **2018**, *8*, 1702322.
18. Yan, K.; Lu, Z. D.; Lee, H. W.; Xiong, F.; Hsu, P. C.; Li, Y. Z.; Zhao, J.; Chu, S.; Cui, Y. Selective deposition and stable encapsulation of lithium through heterogeneous seeded growth. *Nat. Energy* **2016**, *1*, 16010.
19. Yang, C. P.; Yin, Y. X.; Zhang, S. F.; Li, N. W.; Guo, Y. G. Accommodating lithium into 3D current collectors with a submicron skeleton towards long-life lithium metal anodes. *Nat. Commun.* **2015**, *6*, 8058.
20. Zhang, W. D.; Zhuang, H. L. L.; Fan, L.; Gao, L. N.; Lu, Y. Y. A "cation-anion regulation" synergistic anode host for dendrite-free lithium metal batteries. *Sci. Adv.* **2018**, *4*, eaar4410.
21. Zou, P. C.; Wang, Y.; Chiang, S. W.; Wang, X. Y.; Kang, F. Y.; Yang, C. Directing lateral growth of lithium dendrites in micro-compartmented anode arrays for safe lithium metal batteries. *Nat. Commun.* **2018**, *9*, 464.
22. Li, W. Y.; Yao, H. B.; Yan, K.; Zheng, G. Y.; Liang, Z.; Chiang, Y. M.; Cui, Y. The synergetic effect of lithium polysulfide and lithium nitrate to prevent lithium dendrite growth. *Nat. Commun.* **2015**, *6*, 7436.
23. Li, X.; Zheng, J. M.; Ren, X. D.; Engelhard, M. H.; Zhao, W. G.; Li, Q. Y.; Zhang, J. G.; Xu, W. Dendrite-free and performance-enhanced lithium metal batteries through optimizing solvent compositions and adding combinational additives. *Adv. Energy Mater.* **2018**, *8*, 1703022.
24. Zhang, X. Q.; Cheng, X. B.; Chen, X.; Yan, C.; Zhang, Q. Fluoroethylene carbonate additives to render uniform Li deposits in lithium metal batteries. *Adv. Funct. Mater.* **2017**, *27*, 1605989.
25. Zhao, W. G.; Zou, L. F.; Zheng, J. M.; Jia, H. P.; Song, J. H.; Engelhard, M. H.; Wang, C. M.;

Xu, W.; Yang, Y.; Zhang, J. G. Simultaneous stabilization of LiNi0.76Mn0.14Co0.10O2 cathode and lithium metal anode by lithium bis(oxalato)borate as additive. *Chemsuschem* **2018**, *11*, 2211-2220.

26. Zheng, J. M.; Engelhard, M. H.; Mei, D. H.; Jiao, S. H.; Polzin, B. J.; Zhang, J. G.; Xu, W. Electrolyte additive enabled fast charging and stable cycling lithium metal batteries. *Nat. Energy* **2017**, *2*, 17012.
27. Cheng, X. B.; Zhao, M. Q.; Chen, C.; Pentecost, A.; Maleski, K.; Mathis, T.; Zhang, X. Q.; Zhang, Q.; Jiang, J. J.; Gogotsi, Y. Nanodiamonds suppress the growth of lithium dendrites. *Nat. Commun.* **2017**, *8*, 336.
28. Choi, Y.; Choi, Y.; Kwon, O. H.; Kim, B. S. Carbon dots: bottom-up syntheses, properties, and light-harvesting applications. *Chem. Asian J.* **2018**, *13*, 586-598.
29. Choi, Y.; Kang, B.; Lee, J.; Kim, S.; Kim, G. T.; Kang, H.; Lee, B. R.; Kim, H.; Shim, S. H.; Lee, G.; Kwon, O. H.; Kim, B. S. Integrative approach toward uncovering the origin of photoluminescence in dual heteroatom-doped carbon nanodots. *Chem. Mater.* **2016**, *28*, 6840-6847.
30. Zhang, R.; Chen, X. R.; Chen, X.; Cheng, X. B.; Zhang, X. Q.; Yan, C.; Zhang, Q. Lithiophilic sites in doped graphene guide uniform lithium nucleation for dendrite-free lithium metal anodes. *Angew. Chem. Int. Ed.* **2017**, *56*, 7764-7768.
31. Li, Y. Z.; Li, Y. B.; Pei, A. L.; Yan, K.; Sun, Y. M.; Wu, C. L.; Joubert, L. M.; Chin, R.; Koh, A. L.; Yu, Y.; Perrino, J.; Butz, B.; Chu, S.; Cui, Y. Atomic structure of sensitive battery materials and interfaces revealed by cryo-electron microscopy. *Science* **2017**, *358*, 506-510.
32. Li, Y.; Huang, W.; Li, Y.; Pei, A.; Boyle, D. T.; Cui, Y. Correlating structure and function of battery interphases at atomic resolution using cryoelectron microscopy. *Joule* **2018**, *2*, 2167-2177.
33. Jiao, S.; Zheng, J.; Li, Q.; Li, X.; Engelhard, M. H.; Cao, R.; Zhang, J.-G.; Xu, W. Behavior of lithium metal anodes under various capacity utilization and high current density in lithium metal batteries. *Joule* **2018**, *2*, 110-124.
34. Tian, Z.; Zhang, X.; Li, D.; Zhou, D.; Jing, P.; Shen, D.; Qu, S.; Zboril, R.; Rogach, A. L. Full-color inorganic carbon dot phosphors for white-light-emitting diodes. *Adv. Opt. Mater.* **2017**, *5*, 1700416.
35. Frisch, M. J.; Trucks, G. W.; Schlegel, H. B.; Scuseria, G. E.; Robb, M. A.; Cheeseman, J. R.; Scalmani, G.; Barone, V.; Petersson, G. A.; Nakatsuji, H. et al. **2009**, Gaussian 09, Revision D.01, Gaussian, Inc. Wallingford CT.
36. Perdew, J. P.; Burke, K.; Ernzerhof, M. Generalized gradient approximation made simple. *Phys. Rev. Lett.* **1996**, *78*, 3865-3868.

Chapter V. Enhanced mechanical properties of GPE matrix suppresses the Li dendrite growth

5.1 Introduction

Lithium metal batteries (LMBs) are suitable choice to satisfy increasing demands for energy storage systems with high energy density owing to several advantages such as high specific capacity (3,860 mA h g^{-1}) and the extremely low electrochemical potential (-3.04 V vs. standard hydrogen electrode). Therefore, LMBs have been paid much attention as an energy supplier for emerging applications; electric vehicles and energy storage system for the smart grid. However, the thermodynamically unstable surface interface of battery components causes dendritic growth of Lithium (Li) metal during the battery operation. This unintentional Li deposition leads internal short circuit resulting in dead lithium formation, electrolyte depletion, and safety hazard[1-3].

Several strategies of Li dendrite management including an artificial solid-electrolyte interface (SEI) layers[4-9], the advanced structure of framework for even growth of Li[10-15], high concentration electrolyte[16-21] or electrolyte additives for smooth Li plating morphology[22-26], and solid electrolyte with high mechanical strength have been developed[27-29]. Especially, the introduction of solid electrolytes in LMB system is effective owing to Li dendrite suppression through high mechanical strength and minimal Li side reaction. Solid electrolytes are mainly divided into two classifications; solid polymer electrolytes and inorganic solid electrolytes. This solid polymer electrolyte has several advantages such as good adhesion, flexibility, and mass-producibility. However, its insufficient material properties (reference 2~5 order lower ionic conductivity than that of liquid electrolyte, poor mechanical strength than ceramic electrolyte) hinder the wide usage. On the other hands, ceramic solid electrolytes provide relatively high ionic conductivity and excellent modulus which is enough to suppress Li dendrite. Whereas, its inadequate adhesion, low electrochemical window, and difficult fabrication process hinder a practical usage. Therefore, the practical application of solid electrolytes is limited owing to those several intrinsic drawbacks.

In this sense, gel polymer electrolytes (GPEs) are appropriate to resolve the aforementioned issues through its original nature of high ionic conductivity and strong adhesion with the electrode[30-34]. However, the relatively low mechanical strength of GPEs is still insufficient to prevent Li dendrite perfectly. Thus, the introduction of inorganic particle filler such as SiO_2, TiO_2, and Al_2O_3 would improve both mechanical and electrochemical properties. Among these ceramic

filers, SiO_2 particles are an appropriate choice owing to several effects; enable mass production, practicable modification with functional groups and decline interfacial resistance between polymer matrix and electrodes. Although SiO_2 particles have huge merits, there are only a few reports of application with GPEs until now. It is because simple blending or dispersion with SiO_2 particles in GPEs generate particle agglomeration and local inhomogeneity of filers degrading ionic conductivity.

Herein, a vinyl functionalized silica nanoparticles (VSNP) filled-composite polymer electrolyte has been developed through the in-situ crosslinking process[35-38] (Fig. 5-1). In this design, the crosslinked structure of inorganic particles and polymer matrix exhibits high elastic modulus while retaining high ionic conductivity. By incorporating VSNP with trimethylolpropane ethoxylate triacrylate (ETPTA), the mechanical properties of the composite electrolyte are steeply improved which is suitable for Li dendrite suppression. Especially, ETPTA delivers high ionic conductivity and flexibility for good adhesion with lithium metal electrode in this composite electrolyte[39-41]. With the above advantages, 1wt% VSNP crosslinked ETPTA polymer film has a high modulus of ~1 GPa that is nearly 35% higher than that of bare ETPTA film. Also, VSNP crosslinked ETPTA gel polymer electrolyte (ETG-VSNP) has a high ionic conductivity of 3.51 mS cm^{-1} at 25 °C was achieved. The synergetic interplay between high modulus and ionic conductivity of ETG-VSNP effectively suppress Li dendrites and allow a prolonged cycle life without short circuit in electrochemical tests. Because ETG-VSNP system is operated with the simple blending of GPE components and in-situ electrolyte gelation, it has high potential to apply instantly in an industrial setup. The new design offers a promising methodology solving the ionic conductivity versus modulus dilemma and suggests a great solution for commercialization of LMB.

5.2 Experimental

Synthesis of a vinyl functionalized silica particle (VSNP)

Vinyltriethoxysilane (0.95g, alfa asear) and sodium dodecylbenzene sulfonate (0.013 g, sigma aldrich) were added into 30g of DI water under vigorous stirring until an emulsion formed. $NH_3 \cdot 3H_2O$(0.5 mL) was added dropwise to the emulsion (pH = 11.5), and the reaction mixture was kept at room temperature for 3 hours. Isolating the VSNP from the mixed solution through the centrifuge method (9000 rpm for 5 min, 13000 rpm for 10 min, and 16000 rpm for 10 min). 50 to 500 nm sized silica nanoparticles were obtained depending on the centrifuge speed. For the synthesis of non-functionalized silica nanoparticles, the vinyltriethoxysilane precursor was substituted into tetraethyl orthosilicate.

Material Characterization

The microstructural evolution was investigated via scanning electron microscopy, (S-4800, Hitachi), FT-IR analysis (670-IR, Varian), and tensile tester (LAB DA-01, Petrol).

Gel polymer electrolyte Preparation

Trimethylolpropane ethoxylate triacrylate (ETPTA, Mw = 428, Sigma-Aldrich) was mixed with the liquid electrolyte of 1.3 M $LiPF_6$ ethylene carbonate/diethyl carbonate (EC/DEC, 3/7 vol.%) with 10 wt% fluorinated ethylene carbonate additives in a weight ratio of 3/97 under argon atmosphere. Benzoyl peroxide (BPO, 3.0 wt% relative to the ETPTA content) was added as a radical initiator to allow thermal reaction. The mixed GPE solution was sonicated 30min owing to the securement of solution dispersibility. Inorganic filler (1.0 wt% relative to the GPE solution) was mixed with GPE solution through continuous magnetic stirring.

Electrochemical Characterization

Electrochemical tests were performed using a 2032 coin-type Li/Cu half-cell, Li/Li symmetric-cell, and Li/cathode full-cell. The Li/Cu half-cell was composed of a Cu current collector, polymer separator (Celgard 2400), and a lithium electrode (20 μm, 300 μm thickness, Honjo). In the case of the symmetric cell, the Cu current collector was substituted by 300 μm lithium. For the full

cell, 20 and 300 μm-thick lithium electrode was combined with the $LiCoO_2$ (LCO, L&F Inc.) electrode. The LCO cathode consisted of 90 wt.% of active material, 5 wt.% binder (polyvinylidene fluoride (PVDF, KUREHA KF 1100), and 5 wt.% super-P (TIMCAL), which was prepared by the slurry coating method with a loading level of ~7 mg cm^{-2}. The operating conditions were 1.0 V stripping cut-off voltage with a specific capacity of 1 mA h cm^{-2} at 0.1–1 C-rate for the Li/Cu half-cell, 0.5–1 mA h cm^{-2} at 1–5 C-rate for the Li/Li symmetric-cell, and 3.0–4.45 V voltage window with 0.1–1 C-rate for the Li/LCO full-cell. The electrochemical properties were measured using a cycle tester (WBCS3000 battery systems, Wonatech).

5.3 Results and discussion

Vinyl functional groups are successfully constructed on the surface of silica nanoparticles through the Stöber process. A precursor of vinyltriethoxysilane, a dispersing agent of sodium dodecylbenzene sulfonate, and ammonia water solution were mixed and vigorously stirred together to produce the VSNP (see experimental section for detail). Additionally, we synthesized non-functionalized silica nanoparticles from Stöber reaction using tetraethyl orthosilicate and ammonia solution. After the centrifugation and purification process, the average size of 50nm to 500nm silica particles was obtained (Fig. 5-2a). For the preparation of GPE, ETPTA monomer was dissolved in the carbonate liquid electrolyte, wherein benzoyl peroxide was added as a radical initiator to allow thermal reaction. After that, 1wt% of inorganic particles were filled in the GPE for securing the mechanical strength. Finally, in-situ thermal crosslinking process was carried out for the GPE samples, and final products of ETG-VSNP, ETG-SNP, and ETG were obtained. According to the result of Fourier transform infrared (FT-IR) spectroscopy analysis, as-composed VSNP exhibited peaks of vinyl functional group (1615 cm^{-1}) and Si-alkyl end group (1420 cm^{-1}) while the absence of those peaks was observed in the case of bare silica (Fig. 5-2b). In addition, we confirmed that thermal polymerization was successfully occurred in the GPE by checking the disappearance of vinyl group peaks (1617 cm^{-1} and 1635 cm^{-1}) in the ETPTA (Fig. 5-2c).

The mechanical properties of crosslinked GPE samples were scrutinized via tensile strength test. As shown in Fig. 5-2d, ETG-VSNP represented the enough Young's modulus value to suppress the growth of Li dendrite physically of 1.05 GPa which were attributed to the crosslinking between the inorganic filler and the whole polymer matrix, while others indicated insufficient modulus of 0.78 GPa (ETG) and 0.23 GPa (ETG-SNP) each with a lack of binding network. Although the rupture point of ETG-VSNP was relatively smaller owing to the brittle property from the inorganic inclusions than other samples, it performed the highest maximum strength of 9.24 MPa (Fig. 5-2d and e). As a result, we expected that ETG-VSNP would prevent the uneven Li deposition effectively by mechanical strength and show a smooth interface and great electrochemical performance.

To further explore, chemical properties of the GPE samples such as ionic conductivity and transference number were investigated. Firstly, the ionic conductivity value was compared with the candidate samples of liquid electrolyte (LE) and GPE variations. LE exhibits the highest value of 9.5 mS cm^{-1} of conductivity, while ETG shows a decreased conductivity of 3.7 mS cm^{-1} owing to the viscous nature of polymer-based electrolyte (Fig. 5-2f). In the case of inorganic particle filled GPEs, ionic conductivity depends on the particle dispersibility. The ETG-VSNP exhibits

the vinyl functional group originated direct bonding and uniform distribution of silica particles, resulting in the ionic conductivity of 3.5 mS cm^{-1}. In contrast, ETG-SNP with poor particle spread has a relatively low ionic conductivity of 2.5 mS cm^{-1}. Accordingly, silica end groups effectively prevent the particle aggregation and secure the ionic conductivity.

The electrochemical test was performed in various conditions against LE and GPE samples. The results of Li/Li symmetric-cell test with the areal capacity of 1 mAh cm^{-2} and current density of 1 mA cm^{-2} indicate that distinguishable cyclability of ETG-VSNP retains more than 150 cycles with average voltage difference value of 0.223 V (Fig. 5-3a). On the other hands, the overpotential of other symmetric-cells exceeds 500 mV much earlier; LE for 89 cycles, ETG for 120 cycles, and ETG-SNP for 87 cycles, respectively. This trend is also continued to high rate symmetric-cell tests with the areal capacity of 0.4 mAh cm^{-2} and current density of 2 mA cm^{-2} (Fig. 5-3b). The cycle durability of ETG-VSNP leads more than 500 cycles of battery operation with minimum average voltage difference value of 0.265 V. For the LE, GPE, and GPE-SNP samples, we can observe voltage fluctuation and widen in early cycles. This phenomenon explains that the mechanical strength of ETG-VSNP successfully prevents Li dendrite growth, leading to reduced cell resistance and enhanced cyclability

To confirm the Li dendrite suppression by mechanical strength, the morphology of cycled Li metal was investigated by scanning electron microscopy (SEM) for all samples. As expected, LE, ETG, and ETG-SNP samples represent the problems of degradation layer, electrolyte depletion, and Li dendrite growth due to the insufficient strength which causes poor cyclability and internal short circuit (Fig. 5-4a and b). Especially, in the case of ETG-SNP, agglomerated silica cluster is observed owing to the lack of particle dispersibility which damages Li metal surface (Fig. 5-4c). On the contrary, the ETG-VSNP allows not only the formation of a stable SEI with minimal Li degradation and electrolyte depletion, but also conservation of smooth Li surface with Li dendrite suppression (Fig. 5-4d).

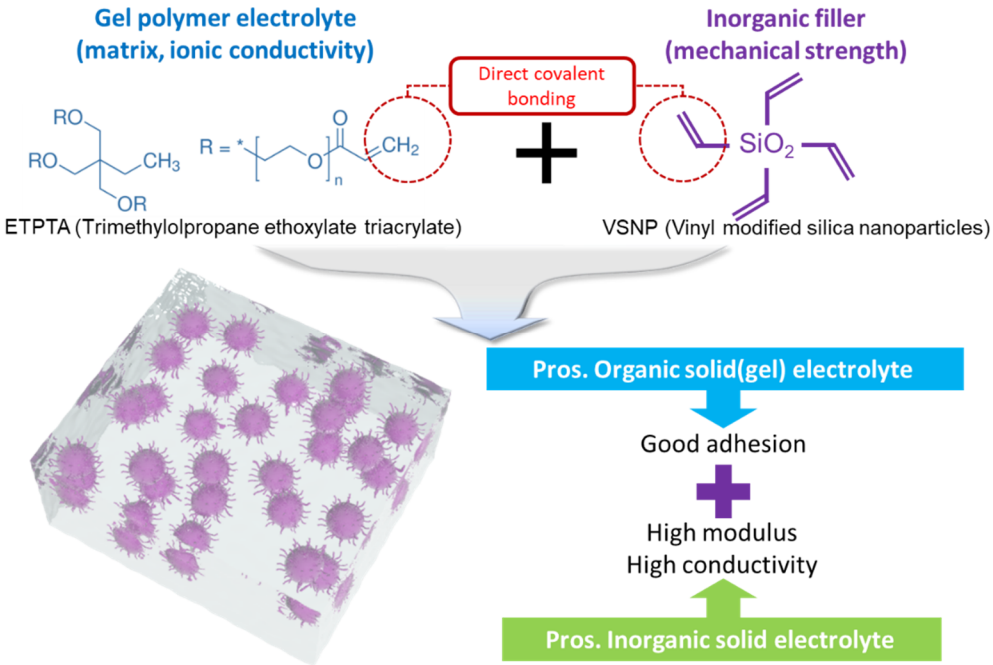

Figure 5-1. Schematic illustration of a synthetic approach for the high mechanical strength of polymer-inorganic filler matrix based gel polymer electrolyte.

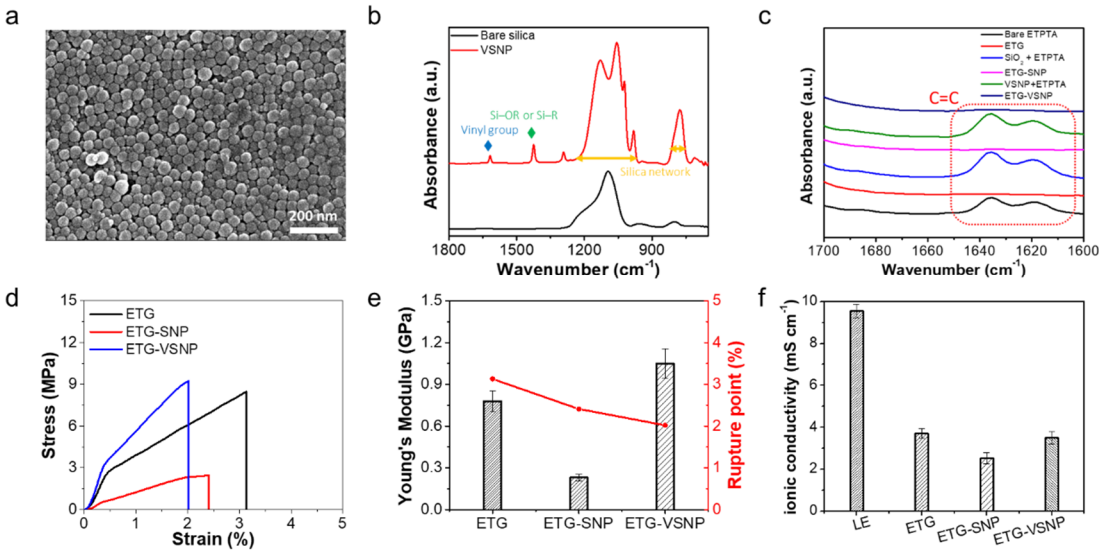

Figure 5-2. Physical and chemical properties of vinyl functionalized silica nanoparticle (VSNP) and various gel polymer electrolyte (GPE). (a) an SEM image of VSNP. FT-IR spectra of (b) bare silica and VSNP. (c) various GPEs before and after gelation. (d) Strain-stress curve of GPEs. (e) Young's Modulus and rupture point of GPEs. (f) ionic conductivity of liquid electrolyte (LE) and various GPEs.

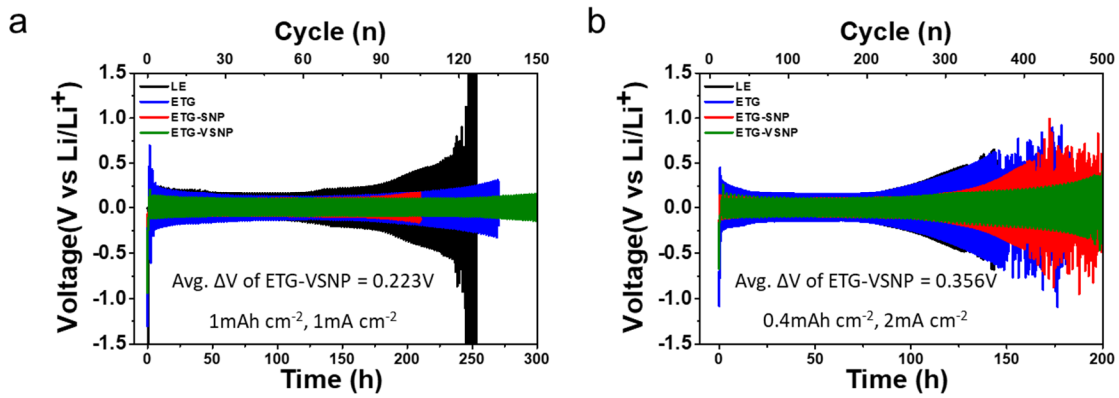

Figure 5-3. The profiles of voltage versus time for lithium stripping/plating experiments of symmetric lithium cells. Voltage profiles for LE and various GPEs with the cycling conditions of (a) an areal capacity of 1mAh cm^{-2} with a current density of 1mA cm^{-2}. (b) an areal capacity of 0.4mAh cm^{-2} with a current density of 2mA cm^{-2}.

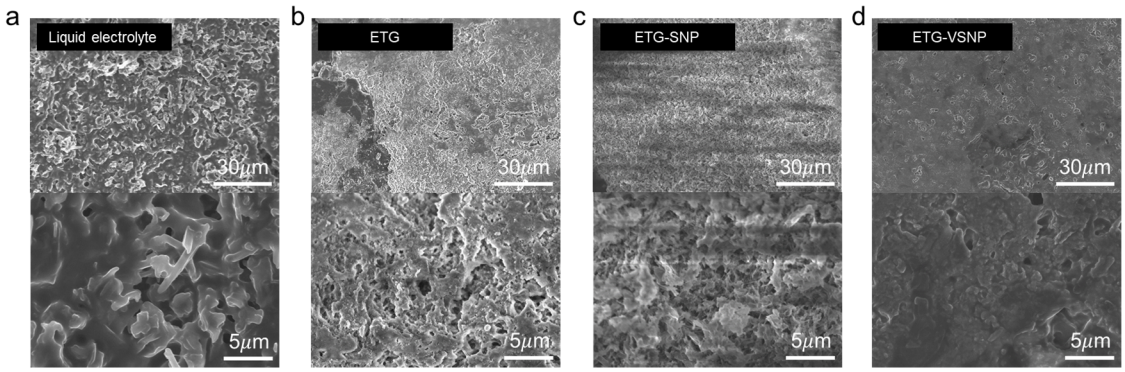

Figure 5-4. Morphology of lithium metal surface after cycles 100 times at 1C-rate with different electrolyte. Components of each electrolyte are (a) liquid electrolyte (b) ETG (c) ETG-SNP (d) ETG-VSNP.

5.4 Conclusions

In summary, we introduce a mechanically strengthened GPE which produces via in-situ thermal polymerization for LMBs. This GPE contains vinyl functionalized silica filler that shows great dispersibility against commercial carbonate electrolyte, leading to uniform distribution along with the GPE matrix and enhanced mechanical strength. Accordingly, ETG-VSNP represents the distinguishable potential for the prevention of unsteady Li deposition and exhibit excellent electrochemical performances, which are attributed to the mechanical strength of well distributed inorganic filler. To establish the relationship between mechanical strength and Li dendrite suppression, electrochemical tests, and analysis for the cycled coin-cell is conducted. The Li/Li symmetric-cell tests of ETG-VSNP under the condition of 1mA h cm^{-2} and 1mA cm^{-2} continues more than 150 cycles, while the potential difference of the LE, ETG, and ETG-SNP start to increase before approaching 80cycles. Similar aspects are observed in the under the high-rate cycling condition of 0.4mA h cm^{-2} and 2mA cm^{-2}. The ETG-VSNP exhibits more than 500 cycles operation with an average voltage difference value of 0.265V, while others show voltage fluctuation before reaching 300 cycles. Furthermore, the SEM results of cycled Li metal for each sample represent a stark difference in the viewpoint of Li dendrite growth, Li surface smoothness, and the degree of degradation layer on the Li metal. The mechanically strengthened GPE in this study has excellent applicability owing to the simple in-situ synthetic step, having a great potential to accept in industry. Therefore, the high mechanical strength of polymer-inorganic filler matrix based GPE will guide a uniform Li plating for LMB.

5.5 References

1. Armand, M.; Tarascon, J. M. Building better batteries. *Nature* **2008**, *451*, 652-657.
2. Xu, w.; Wang, J.; Ding, F.; Chen, X.; Nasybulin, E.; Zhang, Y.; Zhang, J. G. Lithium metal anodes for rechargeable batteries. *Energy Environ. Sci.* **2014**, *7*, 513-537.
3. Cheng, X. B.; Zhang, R.; Zhao, C. Z.; Zhang, Q. Toward safe lithium metal anode in rechargeable batteries: a review. *Chem. Rev.* **2017**, *117*, 10403-10473.
4. Liu, Y.; Lin, D.; Yuen, P. Y.; Liu, K.; Xie, J.; Dauskardt, R. H.; Cui, Y. An artificial solid electrolyte interphase with high li-ion conductivity, mechanical Strength, and flexibility for stable lithium metal anodes *Adv. Mater.* **2017**, *29,* 1605531.
5. Li, N. W.; Yin, Y. X.; Yang, C. P.; Guo, Y. G. An artificial solid electrolyte interphase layer for stable lithium metal anodes. *Adv. Mater.* **2016**, *28*, 1853-1858.
6. Tikekar, M.D.; Choudhury, S.; Tu, Z.; Archer, L. A. Design principles for electrolytes and interfaces for stable lithium-metal batteries. *Nat. Energy* **2016**, *1*, 16114.
7. Fan, L.; Zhuang, H. L.; Gao, L.; Lu, Y.; Archer, L. A. Regulating Li deposition at artificial solid electrolyte interphases. *J. Mater. Chem. A* **2017**, *5*, 3483-3492.
8. Shen, X.; Li, Y.; Qian, T.; Liu, J.; Zhou, J.; Yan, C.; Goodenough, J. B. Lithium anode stable in air for low-cost fabrication of a dendrite-free lithium battery. *Nat. Commun.* **2019**, *10*, 900.
9. Kim, M. S.; Ryu, J.-H.; Deepika; Lim, Y. R.; Nah, I. W.; Lee, K.-R.; Archer, L. A.; Il Cho, W. Langmuir–Blodgett artificial solid-electrolyte interphases for practical lithium metal batteries. *Nat. Energy* **2018**, *3*, 889-898.
10. Wang, H.; Lin, D.; Xie, J.; Liu, Y.; Chen, H.; Li, Y.; Xu, J.; Zhou, G.; Zhang, Z.; Pei, A.; Zhu, Y.; Liu, K.; Wang, K.; Cui, Y. An interconnected channel-like framework as host for lithium metal composite anodes. *Adv. Energy Mater.* **2019**, *9*, 1802720.
11. Zhang, R.; Li, N. W.; Cheng, X. B.; Yin, Y. X.; Zhang, Q.; Guo, Y. G. Advanced micro/nanostructures for lithium metal anodes. *Adv. Sci.* **2017**, *4*, 1600445.
12. Zhang, Y.; Luo, W.; Wang, C.; Li, Y.; Chen, C.; Song, J.; Dai, J.; Hitz, E. M.; Xu, S.; Yang, C.; Wang, Y.; Hu, L. High-capacity, low-tortuosity, and channel-guided lithium metal anode. *Proc. Natl. Acad. Sci. USA* **2017**, *114*, 3584-3589.
13. Li, Q.; Zhu, S;, Lu, Y. 3D porous cu current collector/li-metal composite anode for stable lithium-metal batteries. *Adv. Funct. Mater.* **2017**, *27*, 1606422.
14. Lin, D.; Zhao, J.; Sun, J.; Yao, H.; Liu, Y.; Yan, K.; Cui, Y. Three-dimensional stable lithium metal anode with nanoscale lithium islands embedded in ionically conductive solid matrix. *Proc. Natl. Acad. Sci. USA* **2017**, *114*, 4613-4618.

15. Chi, S. S.; Liu, Y.; Song, W. L.; Fan, L. Z.; Zhang, Q. Prestoring lithium into Stable 3d nickel foam host as dendrite-free lithium metal anode. *Adv. Funct. Mater.* **2017**, *27*, 1700348.
16. Chen, S. R.; Zheng, J. M.; Mei, D. H.; Han, K. S.; Engelhard, M. H.; Zhao, W. G.; Xu, W.; Liu, J.; Zhang, J. G. High-voltage lithium-metal batteries enabled by localized high-concentration electrolytes. *Adv. Mater.* **2018**, *30*, 1706102.
17. Jiao, S. H.; Ren, X. D.; Cao, R. G.; Engelhard, M. H.; Liu, Y. Z.; Hu, D. H.; Mei, D. H.; Zheng, J. M.; Zhao, W. G.; Li, Q. Y.; Liu, N.; Adams, B. D.; Ma, C.; Liu, J.; Zhang, J. G.; Xu, W. Stable cycling of high-voltage lithium metal batteries in ether electrolytes. *Nat. Energy* **2018**, *3*, 739-746.
18. Qian, J. F.; Adams, B. D.; Zheng, J. M.; Xu, W.; Henderson, W. A.; Wang, J.; Bowden, M. E.; Xu, S. C.; Hu, J. Z.; Zhang, J. G. Anode-free rechargeable lithium metal batteries. *Adv. Funct. Mater.* **2016**, *26*, 7094-7102.
19. Qian, J. F.; Henderson, W. A.; Xu, W.; Bhattacharya, P.; Engelhard, M.; Borodin, O.; Zhang, J. G. High rate and stable cycling of lithium metal anode. *Nat. Commun.* **2015**, *6*, 6362.
20. Ren, X. D.; Chen, S. R.; Lee, H.; Mei, D. H.; Engelhard, M. H.; Burton, S. D.; Zhao, W. G.; Zheng, J. M.; Li, Q. Y.; Ding, M. S.; Schroeder, M.; Alvarado, J.; Xu, K.; Meng, Y. S.; Liu, J.; Zhang, J. G.; Xu, W. localized high-concentration sulfone electrolytes for high-efficiency lithium-metal batteries. *Chem* **2018**, *4*, 1877-1892.
21. Suo, L. M.; Hu, Y. S.; Li, H.; Armand, M.; Chen, L. Q. A new class of solvent-in-salt electrolyte for high-energy rechargeable metallic lithium batteries. *Nat. Commun.* **2013**, *4*, 1481.
22. Li, W. Y.; Yao, H. B.; Yan, K.; Zheng, G. Y.; Liang, Z.; Chiang, Y. M.; Cui, Y. The synergetic effect of lithium polysulfide and lithium nitrate to prevent lithium dendrite growth. *Nat. Commun.* **2015**, *6*, 7436.
23. Li, X.; Zheng, J. M.; Ren, X. D.; Engelhard, M. H.; Zhao, W. G.; Li, Q. Y.; Zhang, J. G.; Xu, W. Dendrite-free and performance-enhanced lithium metal batteries through optimizing solvent compositions and adding combinational additives. *Adv. Energy Mater.* **2018**, *8*, 1703022.
24. Zhang, X. Q.; Cheng, X. B.; Chen, X.; Yan, C.; Zhang, Q. Fluoroethylene carbonate additives to render uniform Li deposits in lithium metal batteries. *Adv. Funct. Mater.* **2017**, *27*, 1605989.
25. Zhao, W. G.; Zou, L. F.; Zheng, J. M.; Jia, H. P.; Song, J. H.; Engelhard, M. H.; Wang, C. M.; Xu, W.; Yang, Y.; Zhang, J. G. Simultaneous stabilization of LiNi0.76Mn0.14Co0.10O2 cathode and lithium metal anode by lithium bis(oxalato)borate as additive. *Chemsuschem* **2018**, *11*, 2211-2220.
26. Zheng, J. M.; Engelhard, M. H.; Mei, D. H.; Jiao, S. H.; Polzin, B. J.; Zhang, J. G.; Xu, W.

Electrolyte additive enabled fast charging and stable cycling lithium metal batteries. *Nat. Energy* **2017**, *2*, 17012.

27. Croce, F.; Appetecchi, G. B.; Persi, L.; Scrosati, B. Nanocomposite polymer electrolytes for lithium batteries. *Nature* **1998**, *394*, 456-458.
28. Manthiram, A.; Yu, X.; Wang, S. Lithium battery chemistries enabled by solid-state electrolytes. *Nat. Rev. Mater.* **2017**, *2*, 16103.
29. Zhao, C. Z.; Zhang, X. Q.; Cheng, X. B.; Zhang, R.; Xu, R.; Chen, P. Y.; Peng, H. J.; Huang, J. Q.; Zhang, Q. An anion-immobilized composite electrolyte for dendrite-free lithium metal anodes. *Proc. Natl. Acad. Sci. USA* **2017**, *114*, 11069-11074.
30. Lu, Q.; He, Y. B.; Yu, Q.; Li, B.; Kaneti, Y. V.; Yao, Y.; Kang, F.; Yang, Q. H. Dendrite-free, high-rate, long-life lithium metal batteries with a 3d cross-linked network polymer electrolyte. *Adv. Mater.* **2017**, *29*, 1604460.
31. Shim, J.; Kim, H. J.; Kim, B. G.; Kim, Y. S.; Kim, D. G.; Lee, J. C. 2D boron nitride nanoflakes as a multifunctional additive in gel polymer electrolytes for safe, long cycle life and high rate lithium metal batteries. *Energy Environ. Sci.* **2017**, *10*, 1911.
32. Zuo, T. T.; Shi, Y.; Wu, X. W.; Wang, P. F.; Wang, S. H.; Yin, Y. X.; Wang, W. P.; Ma, Q.; Zeng, X. X.; Ye, H.; Wen, R.; Guo, Y. G. Constructing a stable lithium metal-gel electrolyte interface for quasi-solid-state lithium batteries. *ACS Appl. Mater. Interfaces* **2018**, *10*, 30065-30070.
33. Cheng, Y.; Zhang, L.; Xu, S.; Zhang, H.; Ren, B.; Li, T.; Zhang, S. Ionic liquid functionalized electrospun gel polymer electrolyte for use in a high-performance lithium metal battery. *J. Mater. Chem. A* **2018**, *6*, 18479.
34. Wu, H.; Cao, Y.; Su, H.; Wang, C. Tough gel electrolyte using double polymer network design for the safe, stable cycling of lithium metal battery. *Angew. Chem. Int. Ed.* **2018**, *57*, 1361-1365.
35. Liu, F. Q.; Wang, W. P.; Yin, Y. X.; Zhang, S. F.; Shi, J. L.; Wang, L.; Zhang, X. D.; Zheng, Y.; Zhou, J. J.; Li, L.; Guo, Y. G. Upgrading traditional liquid electrolyte via in situ gelation for future lithium metal batteries. *Sci. Adv.* **2018**, *4*, eaat5383.
36. Lee, Y. W.; Shin, W. K.; Kim, D. W. Cycling performance of lithium-ion polymer batteries assembled using in-situ chemical cross-linking without a free radical initiator. *Solid State Ion.* **2014**, *255*, 6-12.
37. Choi, J. A.; Kang, Y.; Shim, H.; Kim, D. W.; Cha, E.; Kim, D. W. Cycling performance of a lithium-ion polymer cell assembled by in-situ chemical cross-linking with fluorinated phosphorous-based cross-linking agent. *J. Power Sources* **2010**, *195*, 6177-6181.
38. Zhou, D.; Fang, L. Z.; Fan, H.; Shi, Q. Electrochemical performance of trimethylolpropane

trimethylacrylate-based gel polymer electrolyte prepared by in situ thermal polymerization. *Electrochim. Acta* **2013**, *89*, 334-338.

39. Choi, S.; Song, J.; Wang, C.; Park, S.; Wang, G. Multifunctional free-standing gel polymer electrolyte with carbon nanofiber interlayers for high-performance lithium-sulfur batteries. *Chem. Asian J.* **2017**, *12*, 1470-1474.
40. Bok, T.; Cho, S. J.; Choi, S.; Choi, K. H.; Park, H.; Lee, S. Y.; Park, S. An effective coupling of nanostructured Si and gel polymer electrolytes for high-performance lithium-ion battery anodes. *RSC Adv.* **2016**, *6*, 6960-6966.
41. Fan, W.; Li, N. W.; Zhang, X.; Zhao, S.; Cao, R.; Yin, Y.; Xing, Y.; Wang, J.; Guo, Y. G.; Li, C. A dual-salt gel polymer electrolyte with 3d cross-linked polymer network for dendrite-free lithium metal batteries. *Adv. Sci.* **2018**, *5*, 1800559.

Acknowledgement

학문의 길에서 한창 방황하고 있던 저를 거두어 주시고, 4 년 반의 기간 동안 많은 가르침을 주셔서 무사히 학업을 마칠 수 있도록 도와주신 박수진 교수님께 깊이 감사 드립니다. 인생에 중요한 갈림길에서 교수님과 인연을 맺을 수 있었던건 제게 큰 행운이었던 것 같습니다. 연구실을 떠나 사회에 나가서도 교수님의 가르침을 잊지 않고, 부끄럽지 않은 spark 연구실의 일원이 될 수 있도록 항상 노력하겠습니다. 또한 학위를 무사히 마칠 수 있도록 가르침을 주시고 도와주신 심사위원 분들 최남순 교수님, 강석주 교수님, 이현욱 교수님, 장민철 부장님께도 감사 드립니다.

타지에서 온 저를 잘 적응할 수 있도록 먼저 손을 내밀어 주고 즐거운 연구실 생활을 할 수 있도록 도와주신 spark 구성원들에게도 깊이 감사 드립니다. 연구실이 잘 운영될 수 있도록 물심양면으로 지원해주신 정인누나, 맏형으로써 잘 이끌어주시고 많은 조언을 해주신 우진형, 항상 최선을 다하시고 묵묵히 지원해주시는 명수형, 올바른 연구를 할 수 있도록 많은 도움을 준 재건이, 나만 보면 항상 방글방글 웃는 규진이, 돋보적인 비주얼과 피지컬을 지닌 석근이, 빈틈을 보이지만 누구보다 열심히 하는 재현이, 연구실 잘 적응하고 있는 혜빈이, 각 잡혀있는 척하는 컨셉이 잘 어울리는 성진이, 정 많은 리버힐 투덜이 성호, 만인에 인기많은 상엽이, 활력이 과도하게 넘치는 지은이, 뻔뻔함이 매력적인 동엽이, 패셔니스타 민준이, 사회에 먼저 진출해서 spark 의 저력을 보여주고 계신 권도형박사님, 형민형, 신호형, 태수형, 가은이, 소현이, 성희, 우영이, 큰성호 모두 감사합니다.

20 여년의 시간동안 참으로 한결같이 티격태격하면서도 항상 힘이 되어준 정환이, 재균이. 마지막으로, 저의 선택을 전폭적으로 지지해주고 제가 무사히 대학원 생활을 마칠수 있도록 지원해주신 나의 가족들에게 감사하며, 열심히 살아가는 모습을 보여드리겠습니다. 감사합니다.